ABSTRACT

Title of Thesis:	SIMPLIFIED STRUCTURAL DESIGN APPROACH FOR OPEN COMPARTMENTS IN THE CASE OF FIRE
	Parisa Nassiri, Master of Science, 2018
Thesis Directed By:	Dr. Jose L. Torero, Professor, Department of Fire Protection Engineering

A vast majority of modern commercial and office buildings are designed to allow for maximum tenant flexibility. This results in a high demand for open floor plans and for versatility in compartmentation and architecture. The need for a thorough understanding of the behavior of a fire in such spaces is necessary for the improvement of codes and standards as well as for performance-based design.

By considering the thermal properties of typical structural materials the energy equation is studied to establish if a simplified formulation of the thermal boundary condition can be used. The simplified formulation is defined by the characteristic heating time scales and the sensitivity of the structure to develop temperature gradients. Understanding the way in which a structure heats enables engineers to establish an adequate formulation of the fire. A series of full-scale large compartment fires were conducted in order to study the influence on fire behavior on open floor plan spaces in a project called ‘Real Fires for the Safe Design of Tall Buildings’. This work presents

the results from some experiments of the series. The focus is to quantify the fire behavior in what pertains the performance assessment of structural elements. The main objective is to deliver a simplified design approach based on a detailed analysis of the data.

Analysis shows that simplifications can be made for boundary conditions and temperature evolution inside materials in specific conditions.

SIMPLIFIED STRUCTURAL DESIGN APPROACH FOR OPEN COMPARTMENTS IN THE CASE OF FIRE

by

Parisa Nassiri

Thesis submitted to the Faculty of the Graduate School of the
University of Maryland, College Park, in partial fulfillment
of the requirements for the degree of
Master of Science
2018

Advisory Committee:
Professor Jose L. Torero, Ph.D., Chair
Professor Arnaud Trouve, Ph.D.
Associate Professor Michael J. Gollner, Ph.D.

Acknowledgements

First and foremost, I would like to thank my advisor, Dr. Jose Torero for his continuous guidance and support through my research. I am so grateful for all that you taught me.

I would also like to acknowledge Real Fires for the Safe Design of Tall Buildings project team who shared results from their hard work with me.

Additional thanks to my committee members Dr. Arnaud Trouvé and Dr. Michael Gollner. Thank you for sharing your time for reviewing my thesis document, and for offering continuous knowledge during my studies.

I would also like to take the chance to thank Dr. James Milke for his continuous support and encouragements through my studies.

I would like to thank my family for their constant support and encouragement. I would never have made it to this point without you.

Lastly, I would like to thank my husband, Hamed. Thanks for always believing in me and being by my side. Your love and support means the world to me.

Table of Contents

Acknowledgements ii
Table of Contents iii
List of Tables v
List of Figures vi
Nomenclature x
Chapter 1: Introduction 1
1.1 Early design fire 1
1.2 Compartment Fire Framework 3
1.3 *Regime I* fires 4
1.3.1 Energy balance inside the compartment 4
1.3.2 *Regime I* Assumptions 5
1.4 *Regime II* fires 7
1.5 Research Motivations 9
Chapter 2: Structural Thermal Performance 11
2.1 Heat equation and applied conditions 11
2.2 Thermal expansion in a structural element 13
2.3 Curvature in a structural element 15
2.4 Nature of temperature gradient 16
2.4.1 Importance of Biot number 17
2.5 Ranges of temperature variation in the steel web height and thickness 21
2.6 Structure Response 23
2.7 Summary 25
Chapter 3: Edinburgh Tall Building Fire Tests (ETFT) 26
3.1 Compartment description 26
3.1.1 Openings and shutters 27
3.1.2 Gas burners 28
3.2 Fire modes 29
3.3 Ventilation modes 31
3.4 Measured parameters and relevant instrumentations 32
3.4.1 Gas phase temperature 33
3.4.2 Incident radiant heat flux 34
3.4.3 Gas flow velocity 36
3.5 Research Approach 36

3.5.1 Net heat flux calculation 36
3.6 Representative Experiments 41
3.6.1 Experiment 3 42
3.6.2 Experiment 6 43
3.6.3 Experiment 9 44
3.6.4 Experiment 10 46
Chapter 4: Data Analysis 49
4.1 Incident Radiant Heat Flux 49
4.1.1 Experiment 9 49
4.1.2 Experiment 3 62
4.1.3 Experiment 6 64
4.1.4 Experiment 10 66
4.2 Incident Radiant Heat Flux in Near Field 68
4.2.1 Experiment 3 69
4.2.2 Experiment 6 75
4.2.3 Experiment 9 78
4.2.4 Experiment 10 83
4.2.5 Overall mean radiant heat flux in near field 84
4.3 Incident Radiant Heat Flux in Far Field 87
4.3.1 Experiment 3 87
4.3.2 Experiment 9 90
4.4 Convective Heat Flux 91
Chapter 5: Conclusions 97
Bibliography 100

List of Tables

Table 1- Maximum non-dimensional values for I-beam height 21
Table 2- Maximum non-dimensional values obtained for I-beam web thickness 21
Table 3- Different fire spread modes used in the experiments 30
Table 4- Different ventilation modes used in the experiments 32
Table 5- Relevant test instrumentation 33
Table 6- Parameters and their values used for incident radiant heat flux calculation 37
Table 7- Ignition sequences in experiment 3 43
Table 8- Ignition sequences in experiment 9 45
Table 9- Detailed shutter shedule- Experiment 9 46
Table 10- Ignition sequence in experiment 10 48
Table 11- Mean heat flux value for peak duration- Back wall- z = 1.1 m 80
Table 12- Near field radiant heat flux in floor, back wall, and ceiling for different traveling fire experiemnts 84
Table 13- Near field heat flux values and time ratio for different ventilation and fire conditions 98
Table 14- Overview of applicable heat transfer methods for different materials 99

List of Figures

Figure 1- Standard time temperature curve representative as an envelope to results from furnace fire experiments. Extracted from [1] 2
Figure 2- Rate of burning against air flow- Extracted from [9] 8
Figure 3- Boundary conditions for semi-infinite slab - $q0"$ represents the heat imposed to the surface of the compartment from fire, and $T\infty, h$ represent the convective heat transfer 12
Figure 4- T* evolution considering different materials' characteristics including insulation (blue), concrete (green), and steel (red) 14
Figure 5- Temperature gradient in a concrete element in different time steps 16
Figure 6- Schematic of temperature in medium in ambient temperature- T_s is surface temperature, T_b is back temperature and $T\infty$ is ambient temperature 17
Figure 7- Schematic form of temperature gradients in two different mediums- (a) material with high thermal conductivity - (b) material with low thermal conductivity 18
Figure 8- Schematic of temperature variation in materials with real thickness. (a) Realistic steel thickness (b) Realistic insulation thickness 19
Figure 9- Temperature variations in front and back surfaces of steel 20
Figure 10- Temperature variations in front and back surfaces of insulation 20
Figure 11- T* evolution over the height of two different steel profiles 22
Figure 12- T* evolution in web thickness- IPB1000 23
Figure 13- Overview of the compartment (Extracted from [18]) 27
Figure 14- Openings demonstrated as hatched surfaces, all located at x = 5m 27
Figure 15- Gas burners positioning- Extracted from [18] 28
Figure 16- Gas burner layout on compartment floor- Plan view 29
Figure 17- Schematic of a traveling fire- Extracted from [19] 31
Figure 18 – Internal thermocouple locations- elevation view 33
Figure 19- Location of thermocouple trees both inside the compartment and in openings- plan view 34
Figure 20- Real assembled thin skin calorimeter - Extracted from [20] 34
Figure 21- Thin skin calorimeters layout in back wall- Elevation view 35
Figure 22- Thin skin calorimeters layout in floor and ceiling- Plan view 35
Figure 23- Thin skin calorimeters layout in side walls- Elevation view 35

Figure 24- Experiment 3 heat release rate- numbers on the red line present the burners which were operating in labeled time periods 42
Figure 25- Experiment 9 heat release rate- numbers on the red line present the burners which were operating in labeled time periods 45
Figure 26- Plan view of shutters and gas burners layout for experiment 9 – Rectangular boxes marked as yellow represent the shutters which were open from the start of the experiment, green shutters were removed during the test and blue shutters remained closed through the time of experiment..... 46
Figure 27- Experiment 10 heat release rate- numbers on the red line present the burners which were operating in labeled time periods 47
Figure 28- Plan view of shutters and gas burners layout for experiment 10 - Rectangular boxes marked as yellow represent the shutters which were open from the start of the experiment, green shutters were removed during the test and blue shutters remained closed through the time of experiment..... 48
Figure 29- Radiant heat flux 60 seconds after start of the experiment 52
Figure 30- Radiant heat flux 2565 seconds after start of the experiment 53
Figure 31- Node 12B and its distance with the burners..... 54
Figure 32- Radiant heat flux evolution in a TSC located on back wall- Experiment 9 55
Figure 33- Radiant heat flux changes over time in a TSC located on back wall with 2 peak heat flux ranges 57
Figure 34- Shutter malfunction and fire tilt from vertical direction in burner 2..... 58
Figure 35- Shutter malfunction and fire tilt from vertical direction in burner 3..... 59
Figure 36- Heat flux in two different surfaces of the compartment, both graphs obtained for thin skin calorimeters located at y =10.2 m- (a) Thin skin calorimeter on back wall at height of 1.1 m- (b) Thin skin calorimeter located on ceiling at x = 3.9 m 60
Figure 37- Heat flux evolution at different locations of the compartment- Experiment 9..... 61
Figure 38- Heat flux pattern in thin skin calorimeter located at node 12B- Experiment 3..... 62
Figure 39- Radiant heat flux changes over time in a TSC located on back wall with two peak heat flux ranges 64
Figure 40- Heat flux pattern in one of the thin skin calorimeters- Experiment 6..... 65
Figure 41- Radiant heat flux changes over time in a TSC located on back wall..... 67
Figure 42- Radiant heat flux evolution in a TSC located on back wall with two peak heat flux durations- Experiment 10..... 68
Figure 43- Mean values for near field heat fluxes at height of 1.1m – Each line corresponds to location of a burner set on the floor, square boxes with the same color represent the TSCs which capture the maximum heat flux corresponding to the same burner and pink squares show the mean heat fluxes value for thin skin calorimeters with two peaks- Experiment 3 70
Figure 44- Time scaled mean values for the maximum radiant heat flux range- dt_{nf} is the duration when the radiant heat flux was in maximum range and dt_{burner} is the operating duration of corresponding burner set- Experiment 3..... 72

Figure 45- Mean radiant heat flux in near field in all surfaces of the compartment- dt_{nf} represents the near field duration, and dt_{burner} represents the duration when the corresponding burner was operating – Experiment 3 74
Figure 46- Mean values for near field heat fluxes at height of 1.1m – Each line corresponds to location of a burner set on the floor, and square boxes with the same color represent the TSCs which capture the maximum heat flux corresponding to the same burner and pink squares show the mean heat fluxes value for thin skin calorimeters with two peaks - Experiment 6..... 75
Figure 47- Time scaled mean values for the maximum radiant heat flux range- dt_{nf} is the duration when the radiant heat flux was in maximum range and dt_{burner} is the operating duration of corresponding burner set- Experiment 6..... 76
Figure 48- Mean radiant heat flux in near field in all surfaces of the compartment- dt_{nf} represents the near field duration, and dt_{burner} represents the duration when the corresponding burner was operating – Experiment 6 77
Figure 49- Mean values for near field heat fluxes at height of 1.1m – Each line corresponds to location of a burner set on the floor, and square boxes with the same color represent the TSCs which capture the maximum heat flux corresponding to the same burner and pink squares show the mean heat fluxes value for thin skin calorimeters with two peaks - Experiment 9..... 78
Figure 50- Time scaled mean values for the maximum radiant heat flux range- dt_{nf} is the duration when the radiant heat flux was in maximum range and dt_{burner} is the operating duration of corresponding burner set- Experiment 9..... 79
Figure 51- Mean radiant heat flux in near field in all surfaces of the compartment- dt_{nf} represents the duration when the heat flux was in maximum value, and dt_{burner} represents the duration when the corresponding burner was operating..... 81
Figure 52- Mean values for near field heat fluxes – Each blue line corresponds to location of a burner set on the floor, and square boxes with the same color represent the TSCs which capture the maximum heat flux corresponding to the same burner and pink squares show the mean heat fluxes value for thin skin calorimeters with two peaks- Experiment 10 83
Figure 53- Mean near field radiant heat flux for all experiments on each surface- data from experiment 3 is marked as square, experiment 6 is marked as circle and experiment 9 is marked as diamond on each surface..... 86
Figure 54- Incident radiant heat flux in thin skin calorimeter at node 4B located on back wall at height of 1.1m..... 88
Figure 55- Temperature in (a) thin skin calorimeter located at node 4B in back wall, (b) thermocouple adjacent to mentioned thin skin calorimeter 89
Figure 56- Velocity flow in the probes located in opening 14 91
Figure 57- Velocity profile over the height of the compartment. Black vertical line indicates the compartment height and the values indicated in this line are in meters- Red lines indicate the velocity profile in different heights..... 92
Figure 58- Change of convective heat transfer coefficient over height of the compartment 93
Figure 59- Convective heat flux in back wall- node 12B (refer to Figure 21 for location details)..... 94
Figure 60- Temperature averaged in 30 seconds time intervals 95

Figure 61- Temperature averaged in 90 seconds time intervals 95

Nomenclature

A_0	Opening area [m^2]
Bi	Biot-number[-]
c_{p}	Specific heat at constant pressure [J/kgK]
H_0	Opening height [m]
h	Heat transfer coefficient [W/m^2K]
ΔH_c	Heat of combustion per unit mass of Oxygen [J/kg]
k	Thermal conductivity [W/mK]
L	Characteristic length [m]
M	Molar mass [kg/mol]
$\dot{m}$	Mass loss rate [kg/s]
m	Mass [kg]
Nu	Nusselt number [-]
Pr	Prandtl number [-]
P	Pressure [Pa]
$\dot{q}''_{net}$	Net heat flux [W/m^{2}]
$\dot{q}''_{inc}$	Incident radiant heat flux [W/m^2]
$\dot{q}''_{conv}$	Convective heat flux [W/m^2]
Re	Reynolds number [-]
R	Universal gas constant [J/molK]
r	Radius of gyration [m]
S	Surface area [m^2]
T	Temperature [K]
t	Time [s]
T_∞	Ambient temperature [K]
T_0	Fire temperature [K]
T*	Non-dimensional temperature [-]
t*	Non-dimensional time [-]
v_s	Velocity of fire front [m/s]
v	Fluid velocity [m/s]
$Y_{O_{2,\infty}}$	Concentration of ambient Oxygen [kg]
y*	Non-dimensional length [-]

Greek Letters

α	Absorptivity [-]
α	Thermal diffusivity [m^2/s]
α	Coefficient of thermal expansion [$1/K$]
ε	Emissivity [-]
λ	Slenderness ratio [-]
υ	Kinematic viscosity [m^2/s]
ρ	Density [kg/m^3]
σ	Stefan-Boltzmann constant [W/m^2K^4]
υ_s	Oxygen-fuel mass stoichiometric ratio [-]

Abbreviations

TSC	Thin skin calorimeter
HRR	Heat release rate

Subscripts

atm	Atmospheric
c	Convective
disc	Thin skin calorimeter/ solid phase
g	Gas
s	Surface

Chapter 1: Introduction

1.1 Early design fire

The influence of a fire on a structure has been studied now for decades; starting in the late 19th century. The widely used standard time-temperature curve, as presented in Figure 1, was defined by Ingberg [1] and has been specified by various codes and standards including ASTM E119 [2], ISO 834 [3], and BS 476 [4]. This graph was developed based on gas phase temperature measurements in various furnace fire tests. Temperature was measured by thermocouples in the furnace in time and as a result a curve was defined as an envelope for all experimental data. Standard time temperature curve was designed to represent the worst case fire scenario in an enclosure and the required fire resistance was established as the duration of the fire until burnout of the available fuel.

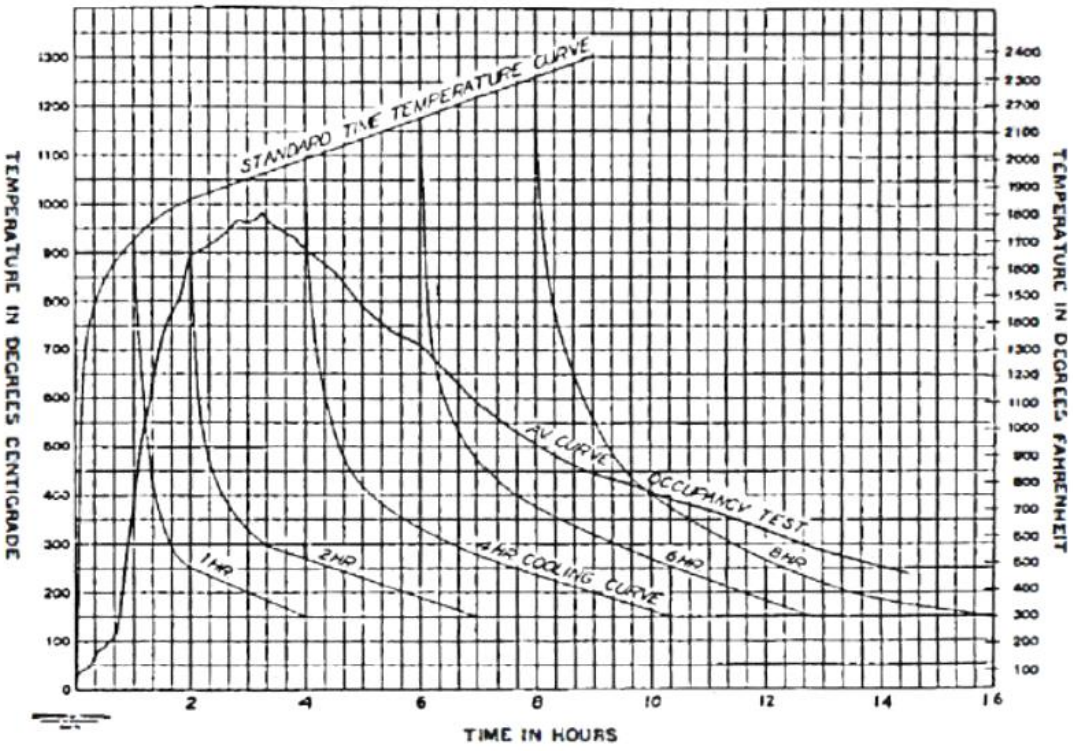

Figure 1- Standard time temperature curve representative as an envelope to results from furnace fire experiments. Extracted from [1]

One of the shortcomings of the standard time temperature curve was referred by Margaret Law as being a single component test and not an appropriate presentation of the structural behavior [5]. Experiments did not study the building as a complete system and characteristics of the building including the geometry, possible fuel loads, and ventilation area were not considered. In addition, the standard time temperature curve does not represent a "real fire" as the temperature in the curve increases indefinitely and does not include important periods of a real fires, including the growth and decay periods.

Studies were continued with decades of experiments of Kawagoe [6], Simms, and Thomas et al. [7] in cubical compartments in under-ventilated conditions which

resulted in creation of the *Compartment Fire Framework* concept. The *Compartment Fire Framework* provides a conservative approach to quantify the effect of elevated temperature in fully developed under-ventilated fire conditions.

1.2 Compartment Fire Framework

Kawagoe [6] conducted series of tests in cubical compartments with various opening sizes and fuel loads while measuring different outputs including, temperature and heat flux. One of the major discoveries of Kawagoe was conducting a linear relationship between the burning rate of the fuel, temperature and the ventilation factor,

$$\dot{m}_b = 0.09 A_0 \sqrt{H_0} \quad (1)$$

Where $\dot{m}_b$ is the burning rate of the oxidizer [kg/s], and $A_0\sqrt{H_0}$ was defined as opening (ventilation) factor, which presents the geometry of opening.

Kawagoe's experiments revealed that time temperature curve does not accurately explain fire behavior in compartments with large openings. Followed by Kawagoe's results, Simms [8] conducted multiple experiments with various fuel and ventilation conditions. His studies divided into reduced scale and full scale experiments which focused on gas phase temperature and decay periods, respectively. As the result, he concluded that with an increase in the air inflow to the compartment, gas phase temperature increases.

Thomas [7] then, divided fire behavior in two categories, referred to *Regime I* and *Regime II*, each function of opening size in the compartment. Thomas concluded that the previously mentioned model defined by Kawagoe does not comply as the opening factor increases [9]. Thomas' studies mainly focused on *Regime I* fires, assuming all

structures follow the regulation for this fire regime behavior. Anything beyond *Regime I* was considered to be unmanageable. Based on the results from the experiments [7], fire load per unit window area and fuel thickness, characterize the duration of *Regime I* fires.

Compartment Fire Framework defines the design fire by means of a constant temperature based on the worst case fire scenario. It was assumed every real fire in the compartment would follow a lower temperature profile, consuming lower amount of fuel, therefore, the structural failure would never be a concern as long as it follows bounds of applicability of framework. Thomas defined the regimes based on the amount of inflow air into a well-defined compartment.

1.3 *Regime I* fires

Regime I fires (also known as "ventilation controlled" fires) are described as fires occurring in compartments with small openings. These compartments allow a limited amount of inflow air to the compartment, which would result in high concentration of smoke, soot, and other combustion products. Burning rate (as shown in Figure 2) would be small and almost proportional to the amount of air flow into the compartment.

1.3.1 Energy balance inside the compartment

In a combustion process inside a compartment, generated heat would either leave the compartment through openings, get stored inside the compartment, or feed the fuel. Each of these changes, affects the temperature of the gas phase inside the compartment (i.e. gas phase temperature inside the compartment can be quantified as a function of time and spatial coordinates ($T_g(x,,y,z,t)$).

Energy conservation equation can be presented as following:

$$\frac{dQ_{CV}}{dt} = \dot{Q}_{in} - \dot{Q}_{out} + \dot{Q} - \dot{Q}_{W} \quad (2)$$

Where $\frac{dQ_{CV}}{dt}$ presents the conservation of energy in a fixed control volume (i.e. the compartment), $\dot{Q}_{in}$ is the rate of heat entering the compartment, $\dot{Q}_{out}$ is the rate of heat lost from the compartment, $\dot{Q}$ is total heat release rate of fire, and $\dot{Q}_{W}$ is the rate of heat losses to the boundaries of the compartment.

Some simplifications can be made to the aforementioned correlation as a result of considerable temperature difference between inflow cold gases and outflow hot gases. Therefore, previous equation can be rewritten as following:

$$1 = \frac{\dot{Q}_{out}}{\dot{Q}} + \frac{\dot{Q}_{W}}{\dot{Q}} \quad (3)$$

1.3.2 *Regime I* Assumptions

Important assumptions made to describe behavior of *Regime I* fires are provided in detail by Torero et al. [10]. Some of these assumptions are as following.

- Smoke inside the compartment is in a quasi-steady temperature, i.e. gas temperature reaches and stays in its maximum value almost instantaneously. Also, solid phase temperature is assumed constant. Reason would be that the smoke fills the compartment in early stages of the fire, which results in high gas temperature inside the compartment, besides, characteristic time for the structural elements to heat up is relatively long compared to gas temperature. This assumption simplifies the conservation of energy equation and will be discussed further in followed section. Exception to previous statements was

made at the openings where the cold inflow air is continuously entering the compartment.

- It was assumed that all of the oxygen entering the compartment is consumed and transformed to energy. Heat release rate would then be defined as $\dot{Q} = \dot{m} Y_{O_2,\infty} \Delta H_{O_2}$, where $\dot{m}$ shows the mass loss rate, $Y_{O_2,\infty}$ is concentration of ambient Oxygen, and heat of combustion per kilogram of oxygen consumed is given by ΔH_{O_2}. This assumption simplifies the problem.
    - It eliminates the need to both define the oxygen concentration in combustion products, and resolve oxygen transport equation inside the compartment.
    - It limits the analysis to fuel-rich conditions.
    - All oxygen in the reaction zone consumes due to existence of fast chemistry.
    - The control volume acts as a perfectly stirred reactor.
    - Completeness of the combustion is independent of the compartment (heat of combustion assumed to be constant).
- Gases inside the compartment have relatively low vertical velocity in the entire compartment. Exceptions was made for the openings where fresh air and smoke flow inside and outside of the compartment, respectively. Rate of mass change of air through openings into the compartment, can be calculated by $\dot{m} = C A_0 \sqrt{H_0}$, where C is a constant value, A_0 and H_0 are representatives of the opening geometry. This correlation demonstrates that the rate of burning is

proportional to the airflow into the compartment (valid only for compartments with small openings).

- Finally, it was assumed the radiative heat loss from the openings are almost negligible.

A linearized heat transfer approximation is used within the compartment considering aforementioned assumptions which results in simple formulation for both burning rate and heat transfer inside the compartment. This framework formulations are only valid in the condition which compartment complies with aforementioned assumptions.

1.4 *Regime II* fires

Regime II fires (also known as "fuel-surface controlled" fires) are defined as fires occurring in compartments with large opening areas, allowing for large amount of inflow of air to the compartment. Based on Thomas' results (shown in Figure 2) burning rate inside the compartment seems to be independent to the air flow. Probable cause would be that since these fires are fuel surface controlled, burning rate inside the compartment is defined by the amount of fuel load, and not the inflow air.

Simplifications made in Regime I fires no longer applies. Major portion of heat evacuates the compartment through openings, amount of stored heat inside the compartment decreases, and gases have lower average temperature throughout the fire duration. In addition, temperature distribution inside the compartment needs to be taken into account.

Figure 2, confirms aforementioned statements. Based on the results from his experiments, in Regime I fires, rate of weight loss is proportional to the air flow. As

the air flow increases the fire transforms to a *Regime II* fire where rate of weight loss is almost independent to the air inflow and $\dot{m}$ reaches an almost steady condition.

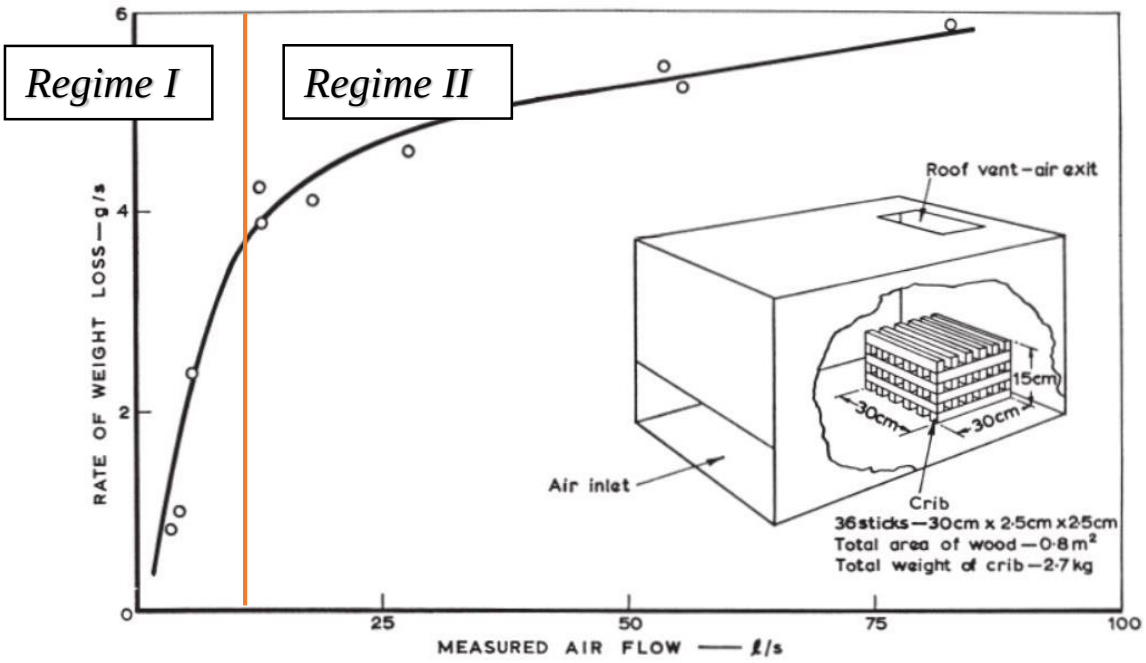

Figure 2- Rate of burning against air flow- Extracted from [9]

Whether or not a fire is considered either regimes, highly depends on the size of the compartment, ventilation sizes, and the opening factor.

First series of *Regime II* fire experiments were conducted by Kirby et al. [11] in Cardington (known as Cardington natural fire tests) and was followed by Dalmarnock fire tests [12] in 2006.

Although previously mentioned test series provided some heat flux [13] and temperature baselines, they clearly had multiple shortcomings including low resolution in measured data. In addition, size of the compartment which was used in Dalmarnock experiments was relatively small.

In order to overcome the issues, series of large scale open floor plan compartment experiments, called Edinburgh Tall Building Fire Tests were conducted as a part of

Real Fires for the Safe Design of Tall Buildings project [14] [10]. Different ventilation and conditions were simulated in these experiments in order to simulate *Regime I* and *Regime II* fires

Detailed description of the compartments and experiments will be provided in details in following chapters.

1.5 Research Motivations

Simplified characterizations used in *Regime I* fires resulted in correlations from numerous experiments in small cubical compartments obtained by solving simple energy balances. These design tools fail to quantify fire behavior in open compartments (i.e. *Regime II* fires) since the simplifying assumptions are not valid as both the compartment and the opening size are increased.

In order to study Regime II fires and their effect on the structure, two stages need to be considered

- Structural thermal performance and the way structure responds to elevated temperature as a function of boundary conditions.
- Fire performance and how thermal energy transfers into structural elements.

A series of full-scale large compartment fires from ETFT project were conducted in order to study the influence on fire behavior of open floor plan spaces and new building designs. This series of tests consists of 10 gas burner fires, with different modes of fire behavior, including traveling and growing fires as well as fully developed fires; also two wood cribs fire tests are conducted as a more realistic approach in order to verify the analysis results.

This work reviews the effect of the effect of *Regime II* fires (more specifically traveling fires) on the structural elements of open compartments based on the results obtained from large-scale tests. The main goal is to propose a simplified approach for structural fire design of open compartments by eliminating the need for detailed and complex heat transfer analyses.

Chapter 2: Structural Thermal Performance

Performance of a structure in the case of fire is dominated by two phenomena known as thermal expansion and curvature. Former is imposed to the structure due to elevated temperature and the latter would be caused as a response to temperature gradients. Failure mode of the structure, in most cases, follows a combination of the two. Compartment fire framework perfectly addressed the temperature evolution inside the compartment although due to complexities it did not address the temperature gradients. In order to define the behavior of structure, both phenomena need to be defined. Energy equation explains the temperature evolution within each material after accurately defining initial and boundary conditions. Knowledge of temperature distribution inside solids, reveals the level of structural integrity within the material.

2.1 Heat equation and applied conditions

According to literature, one-dimensional heat diffusion equation (also referred to as heat equation) inside a homogenous medium, in Cartesian coordinates can be written as following [15]:

$$\rho c_p \frac{\partial T}{\partial t} = k \frac{\partial^2 T}{\partial y^2} \quad (4)$$

Where $\rho c_p \frac{\partial T}{\partial t}$ represents the time rate of change of thermal energy of the medium per unit volume, and $k \frac{\partial^2 T}{\partial y^2}$ corresponds to net conduction heat flux into the control volume for the specified direction. Solution for the aforementioned equation, which highly depends on material characteristics, will result in temperature distribution in time and space. In order to solve the aforementioned equation, couple of boundary conditions and an initial condition need to be defined (since the equation is in second order in spatial coordinate, and first order in time). Semi- infinite slab, which describes as a solid that extends to infinity in all but one direction, was selected as basis geometry to solve equation 4. It was assumed that both a non-zero heat flux, and surface convection are imposed to the considered surface to perfectly simulate the conditions present in the experiments. Figure 3 illustrates the mentioned assumptions.

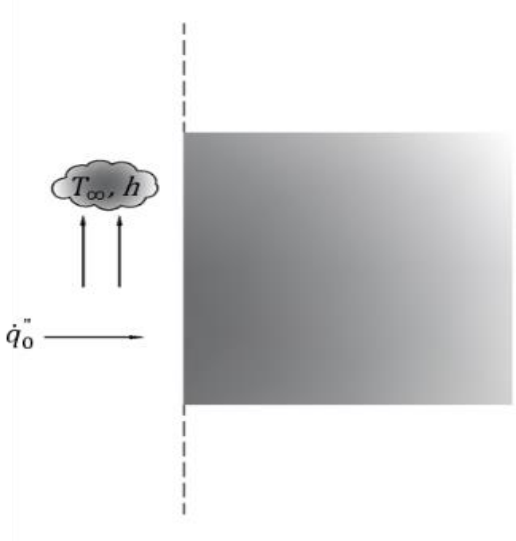

Figure 3- Boundary conditions for semi-infinite slab - $\dot{q}''_0$ represents the heat imposed to the surface of the compartment from fire, and T_∞, h represent the convective heat transfer

Besides, surface temperature of the medium assumed to be same as ambient temperature at the start of the experiment, therefore, initial condition was defined as $T_{(y,0)} = T_\infty$.

2.2 Thermal expansion in a structural element

In a general form, heat equation in a semi-infinite slab in the presence of heat flux and surface convection, considering the mentioned initial condition and surface boundary conditions, yields into an analytical solution presented in literature as following [15]:

$$\frac{T_{(y,t)}-T_\infty}{T_0-T_\infty} = erfc\left(\frac{y}{2\sqrt{\alpha t}}\right) - [\exp(\frac{hy}{k}+\frac{h^2\alpha t}{k^2})][erfc(\frac{y}{2\sqrt{\alpha t}}+\frac{h\sqrt{\alpha t}}{k})] \quad (5)$$

A general solution for temperature evolution within a material will be obtained by converting some parameters of the equation into non-dimensional form. This makes it possible for the equation to be solved for different materials, regardless of their characteristics. Including the properties into consideration, yields numerical results for a specific material.

Non-dimensional parameters, are defined as following:

$$y^* = y/y_c \quad (6)$$

And

$$t^* = t/t_c \quad (7)$$

Where y_c and t_c are characteristic length and time, respectively.

$$y_c = \frac{k}{h} \quad (8)$$

$$t_c = \frac{k^2}{h^2\alpha} \quad (9)$$

By substituting equations 6 and 7 into equation 5 the non-dimensional temperature will be obtained.

$$T^* = erfc\left(\frac{y^*}{2\sqrt{t^*}}\right) - [\exp(y^*+t^*)]\left[erfc\left(\left(\frac{y^*}{2\sqrt{t^*}}\right)+\sqrt{t^*}\right)\right] \quad (10)$$

Equation 10 represents the temperature evolution of material in space and time. This parameters can be used to define the thermal expansion within a structural element.

According to related correlations, T^*, y^*, and t^* are all functions of either h/k or h^2/k^2. Heat transfer coefficient highly depends on the fluid characteristics and would vary for each and every fire, although it can be approximated as a single value for different materials exposed to same fire condition. Other parameter, is thermal conductivity of the material which can be approximated in mean temperature. Figure 4 presents visual evolution of the T^* correlation considering ordinary characteristics and dimensions of insulation, concrete and steel.

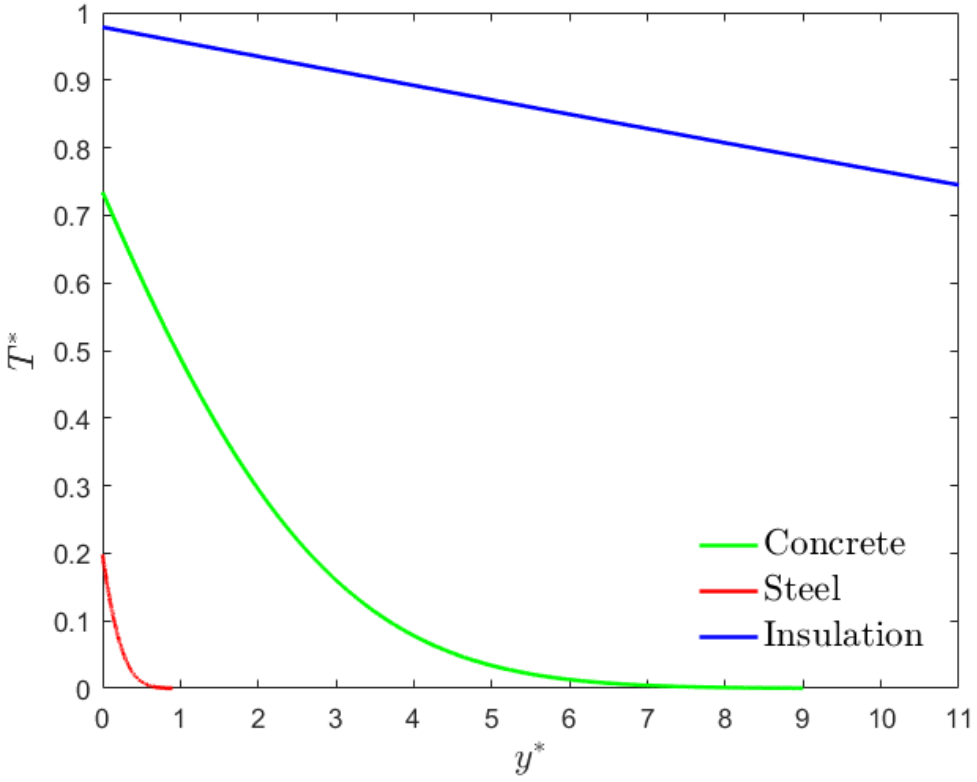

Figure 4- T evolution considering different materials' characteristics including insulation (blue), concrete (green), and steel (red)*

Some assumptions were made to plot these graph which include:

One of the required properties of the materials was thermal conductivity. The values are well defined for some materials such as steel although a high scattered data exists

for other materials in the literature. After all, thermal conductivity of insulation, concrete and steel was set to 0.04, 1, and 50 $[W/mK]$, respectively [16].

Total duration of the fire was assumed to be 60 minutes to represent a typical fire that happens in open compartments.

Each material was set to range of realistic dimensions.

Heat transfer coefficient was assumed to be $45\ [W/m^2K]$ for the purposes of this scaling analysis, nevertheless, as observed in previous chapters, this value will have to be modified depending on the location of the structure with respect to the fire.

2.3 Curvature in a structural element

Deriving the T^* correlation, yields to temperature gradients inside material which is representative of curvature in a medium.

$$\frac{\partial T^*}{\partial y^*} = \exp(-\frac{{y^*}^2}{4t^*}) \tag{11}$$

This correlation is in general form without considering properties of materials. Figure 5 shows the visual form of the temperature gradient equation considering concrete properties as an instance in various time steps.

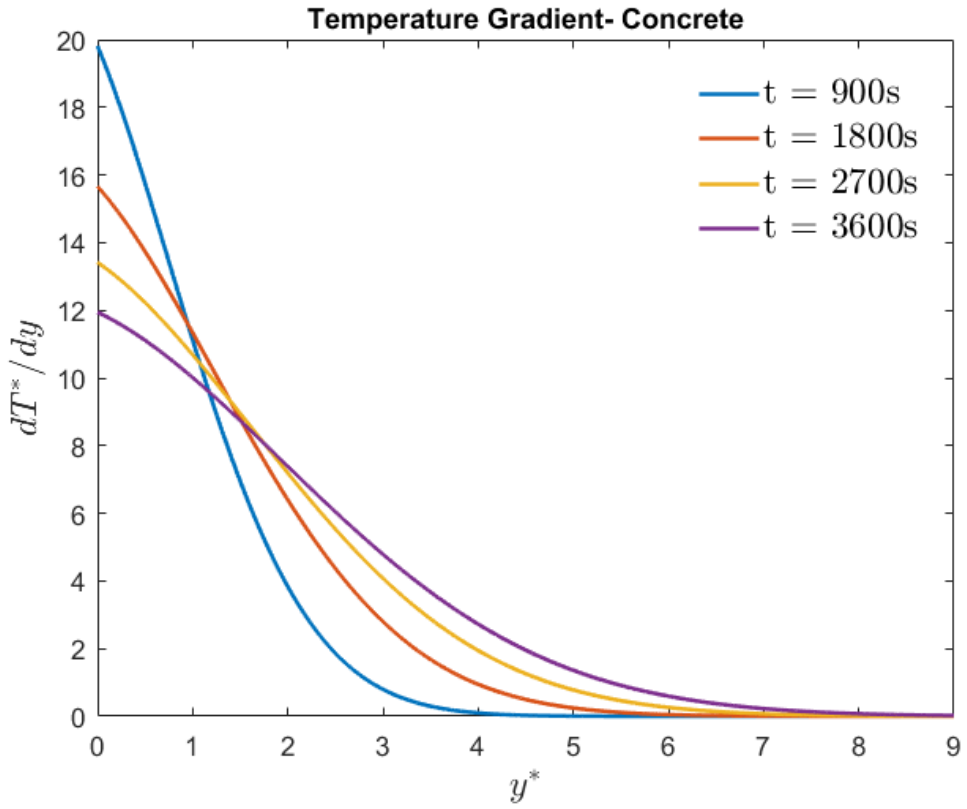

Figure 5- Temperature gradient in a concrete element in different time steps

It would be worth mentioning that time steps used to plot Figure 5 are actual times and not the characteristic time or t^*.

2.4 Nature of temperature gradient

In first time steps of the fire when gases are in ambient condition, temperature distribution through medium has a pattern as presented in Figure 6. At room temperature and in the absence of heat sources, material is in thermal equilibrium with its surrounding therefore temperature in sides of the material can be approximated as almost equal to ambient temperature. As fire grows, gas phase temperature increases almost instantaneously and temperature of the solid phase stars to rise. Rate of temperature increase rate in the solid material is function of its properties.

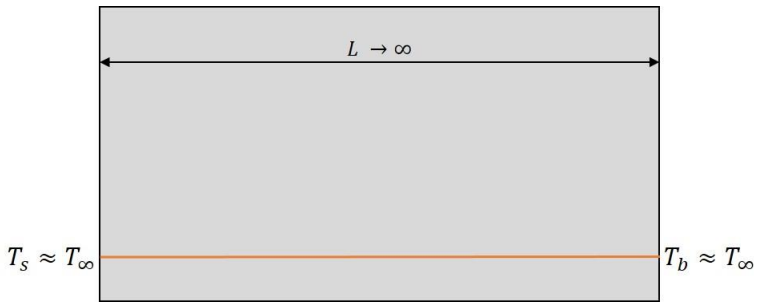

Figure 6- Schematic of temperature in medium in ambient temperature- T_s is surface temperature, T_b is back temperature and $T\infty$ is ambient temperature

2.4.1 Importance of Biot number

According to Torero et al. [16] a single temperature value for a specific material is not an adequate representation of the temperature evolution inside the medium. Biot number is used to define the nature of temperature gradient within material and is defined by

$$Bi = \frac{h_T d}{k} \tag{12}$$

Where h_T is total heat transfer coefficient of material $[W/m^2K]$, d represents the characteristic length $[m]$, and k is thermal conductivity of solid material $[W/mK]$.

Biot number presents the relationship between temperature gradients in the gas phase and solid phase. Parameters that affect the Biot number are mentioned above, in order to study the effect of material properties, fixed thickness (infinite thickness in the extreme condition) for different kinds of materials under a unique fire condition was assumed. This assumptions result in a Biot number solely dependent on thermal conductivity. Simplifications can be made for materials with very large or very small thermal conductivities. Materials with very large thermal conductivities result in low Biot numbers. Temperature gradient is small in the solid phase, thus a single temperature value (i.e. gas phase temperature value) can be assumed within the solid.

In contrast, materials with very small thermal conductivities (i.e. very large Biot numbers), increase the time for heat to transfer to other side of the material. Temperature gradients in solid phase is considerable in a way that the boundary layer conditions can be neglected. Reason would be that temperature difference in the boundary layer between the gas and solid phase are much smaller than the temperature gradient in the material, that the surface and gas phase can be assumed to be at the same temperature. Figure 7 shows schematic form of temperature gradients in two different mediums with high and low thermal conductivities. Other possible case would be when the temperature gradients in both solid phase and gas phase are high. In this case Biot number is close to one, previously mentioned simplifications no longer apply, and energy equations need to be solved.

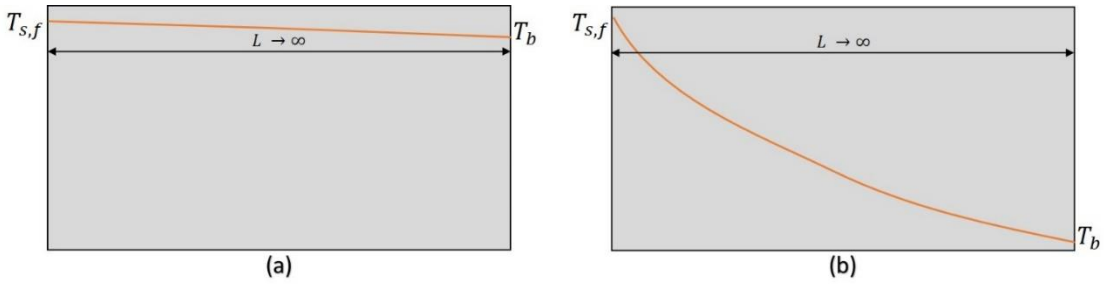

Figure 7- Schematic form of temperature gradients in two different mediums- (a) material with high thermal conductivity - (b) material with low thermal conductivity

A more realistic approach would be considering approximate real dimensions of materials. Figure 8 presents a schematic form of steel with real dimensions shown in green color and insulation in blue. As shown in the figure, not only the temperature variation within the steel material is small, but also the steel itself has small thicknesses which makes it more reasonable to neglect the temperature gradients. In contrary, considerable temperature variation occurs in insulation (as an instance of a material

with low thermal conductivity) which makes it unreasonable to ignore the temperature gradient.

Materials such as concrete, with moderate thermal conductivities, result in Biot numbers closer to one. In addition, average thickness of the concrete slabs, beams or columns, is higher than both steel and insulation. Mentioned uncertainties implies the importance of heat transfer analysis in conditions when assuming a mean temperature value through material lead to unacceptable errors.

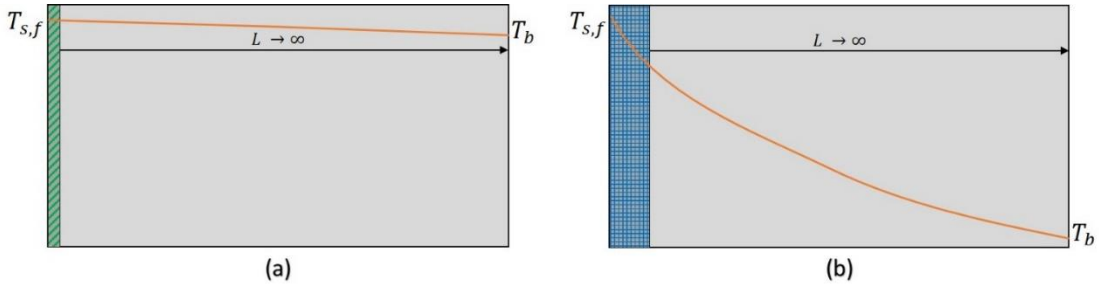

Figure 8- Schematic of temperature variation in materials with real thickness. (a) Realistic steel thickness (b) Realistic insulation thickness

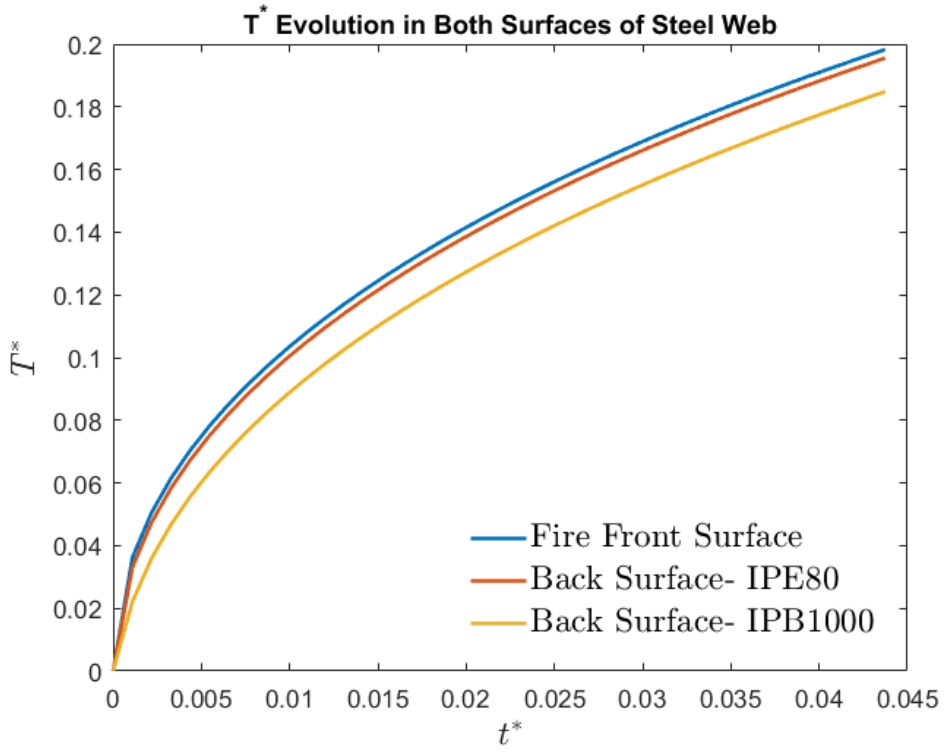

Figure 9 and Figure 10 represent temperature evolution through web thickness of two steel sections as well as an insulation material, respectively. Steel I-beam sections selected were IPE80 as an example of a small section, and IPB1000 as an instance of a large section. Based on this figure, temperature difference between the surfaces of either sections is small, which also proves the previously mentioned argument and simplifications.

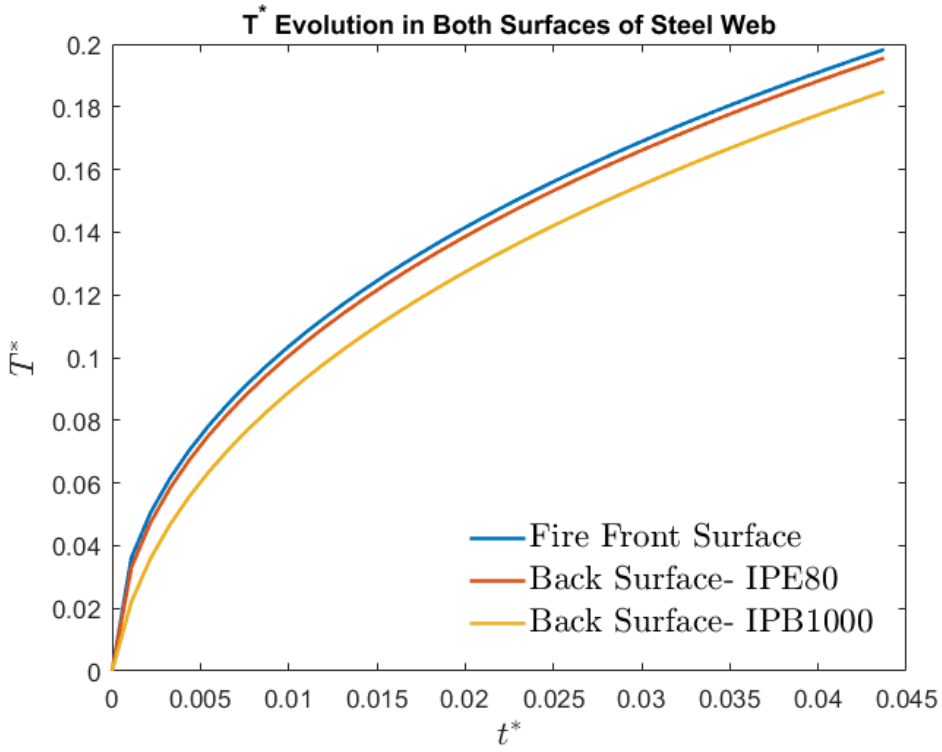

Figure 9- Temperature variations in front and back surfaces of steel

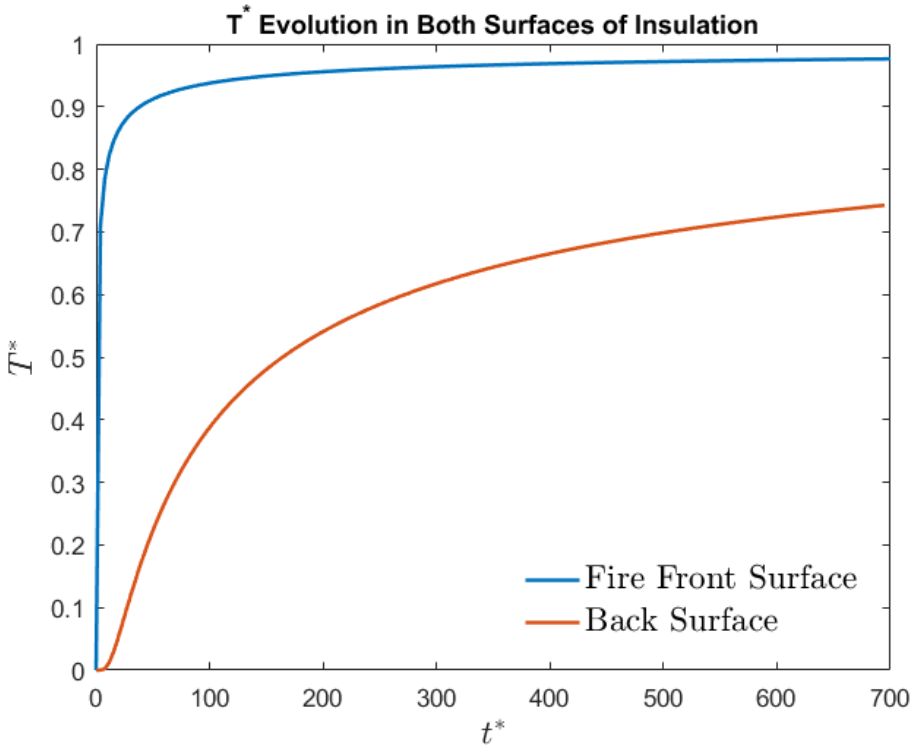

Figure 10- Temperature variations in front and back surfaces of insulation

Extreme values of T^*, y^* and t^* for height of the profile and web thickness were calculated based on aforementioned details and are stated in Table 1 and Table 2. Properties of the selected steel profiles were obtained from Stahl tables. As a reference IPE 80 has height of 80 mm and web thickness of 3.8 mm, and IPB 1000 has height of 1000 mm and web thickness of 19 mm. In addition, as mentioned in the assumptions, fire burnout time was set to 60 minutes.

Table 1- Maximum non-dimensional values for I-beam height

Steel Section	y^*	t^*	T^*	dT^*/dy
IPE 80	0.072	0.04374	0.19828	0.803
IPB 1000	0.9	0.04374	0.19828	0.803

Table 2- Maximum non-dimensional values obtained for I-beam web thickness

Steel Section	y^*	t^*	T^*	dT^*/dy

IPE 80	0.00342	0.04374	0.19828	0.803
IPB 1000	0.0171	0.04374	0.19828	0.803

2.5 Ranges of temperature variation in the steel web height and thickness

Figure 11 shows the temperature evolution in section height i.e. this graph presents T^* plotted in different time steps. According to these figures, assuming a single mean temperature value throughout the steel section height results in major errors. IPE80 is one of the smallest steel profiles with a section height of 80 mm. Assuming an average temperature throughout height of the section, results in almost 14% error. Also, assuming the mean temperature value through the height of IPB1000 results 50% error.

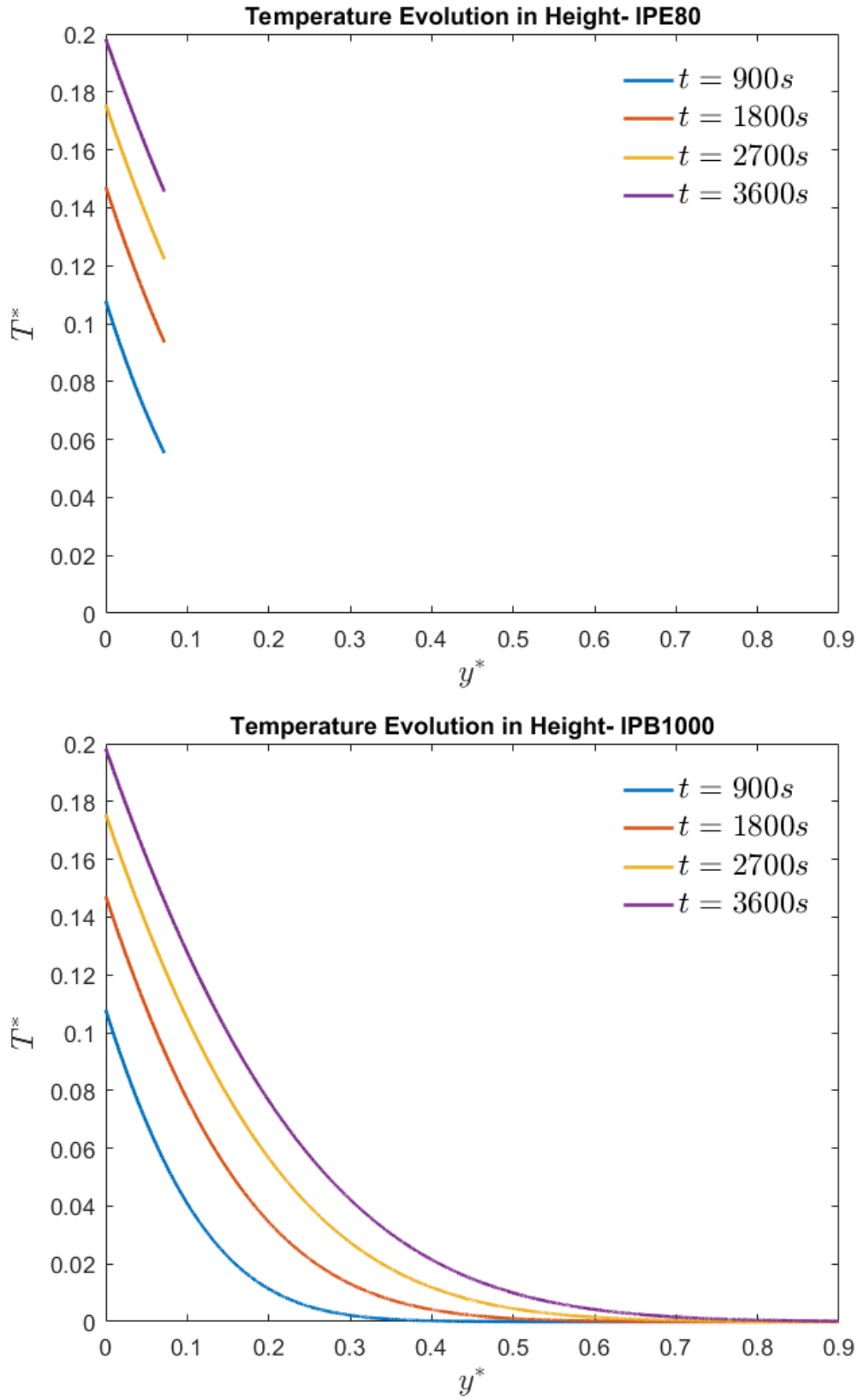

Figure 11- T evolution over the height of two different steel profiles*

Temperature evolution within the web thickness would be smaller in comparison with section height since the considered length is small. Figure 12 shows T^* evolution in IPB1000 with web thickness 19 mm. Error of in IPE80 would be negligible as the temperature variation in very small. In addition, considering the mean temperature value for IPB1000, would result in 4% error. In cases where the error is small, such as steel profile's web thickness, considering the gas phase temperature through material would be an appropriate approximation.

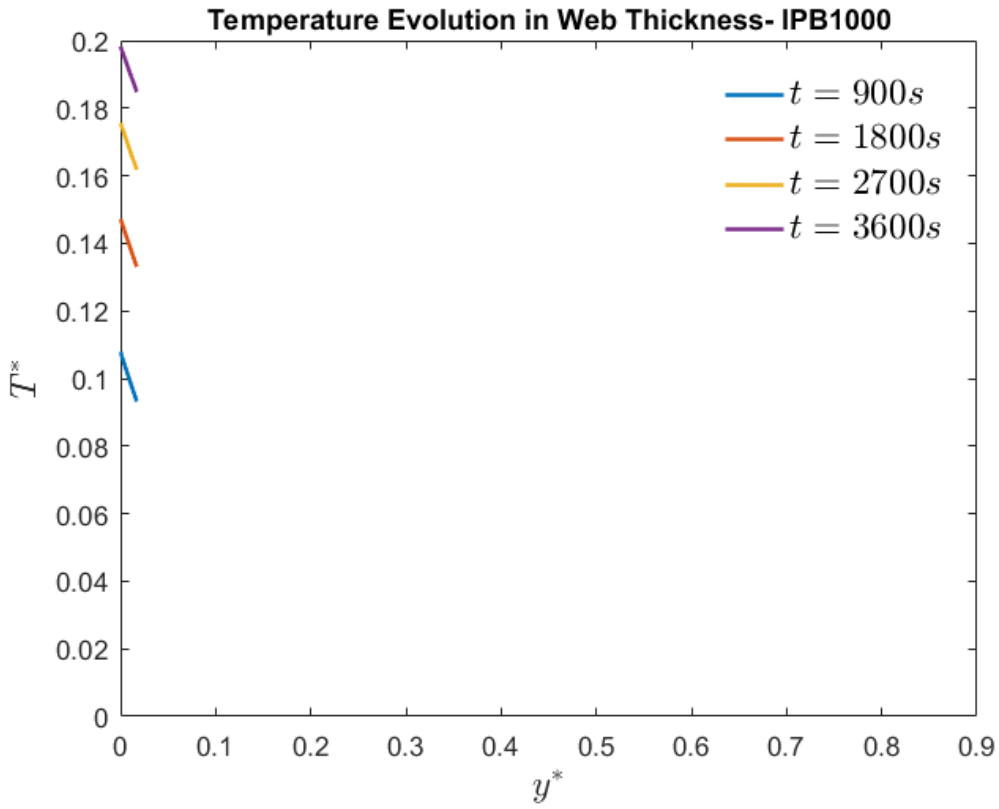

Figure 12- T evolution in web thickness- IPB1000*

2.6 Structure Response

As explained in detail by Usmani et al. [17] response of different materials to elevated temperatures depends not only on the thermal properties of the material but also on the

geometry of the structure. For instance a steel beam will either buckle or yield as temperature increases. Former would happen if the beam is slender. Slenderness ratio of beam depends on the length of the beam and gyration radius. In this case, material buckles before it reaches the yield stress and no longer bears the forces.

$$\lambda = l/r \tag{13}$$

$$r = \sqrt{I/A} \tag{14}$$

Where λ is the slenderness ratio, l is the characteristic length [m], and r is the gyration radius [m]. In addition, I is the second moment of area [m^4], and A is the total cross-sectional area [m^2].

In contrast, an element yields when it is stocky. In this case the slenderness ratio of the beam is more than critical value of slenderness ratio. Axial stress in the beam increases until it reaches the yield value and the beam continues to yield after this point without significant amount of force.

According to Usmani et al. [17] there would be possible to find the critical temperature that results in either buckling or yielding of the steel beam. For slender beams the temperature difference that results in buckling is as following:

$$\Delta T_{cr} = \frac{\pi^2}{\alpha\lambda^2} \tag{15}$$

Also, temperature difference that would result in yielding of the material in stocky beams would be as below:

$$\Delta T_y = \frac{\sigma_y}{E\alpha} \tag{16}$$

Where σ_y is the yield stress [Pa], E is the modulus of elasticity [Pa] and α is coefficient of thermal expansion [$1/K$].

Both aforementioned equations depend on the geometry and section characteristics of the beam.

2.7 Summary

In summary, simplifications can be made for some materials including steel with small dimension although in materials with high complexities and uncertainties, detailed heat transfer analysis would be required. Whether or not a simplification will be applicable for a material depends on following details.

For steel in the case where $y < L_c$, Lumped capacitance will be applicable and in the case which $y > L_c$, one dimensional conduction heat transfer analysis shall be done. For concrete in all cases one dimensional conduction heat transfer analysis shall be done. Insulation can be divided into two high density and low density categories. In the former case, one dimensional conduction heat transfer analysis shall always be done although for low density insulating materials (sprays), for $t < t_c$ it can be assumed that $T_s = T_g$, and for $t > t_c$, one dimensional conduction heat transfer analysis shall be done.

Chapter 3: Edinburgh Tall Building Fire Tests (ETFT)

This chapter provides a detailed description of the compartment used for ETFT series as part of Real Fires for the Safe Design of Tall Buildings project.

Different modes of fire and ventilation, related instrumentations inside the compartment and measured parameters in the experiments will be described in this chapter.

In addition, approach for calculating different parameters from obtained data from instruments will be discussed in this chapter.

3.1 Compartment description

Fire experiments were all conducted in BRE test facility, located in Watford, UK. A detailed description of the experimental enclosure is presented by Hidalgo et al. [18]. The compartment itself, was designed with outer dimensions of 18 m in length, and 5 m in depth, representative of the largest possible floor plan that could be built inside the Burn Hall of BRE test facility. In addition, height of the structure was designed to be 2 m in order to be scaled with other dimensions of the compartment to present a realistic compartment with open floor plan. Figure 13 demonstrates the compartment

design and location of the openings. A 0.5 m overhang placed all across the open side of the compartment which resulted in opening height of 1.5 m.

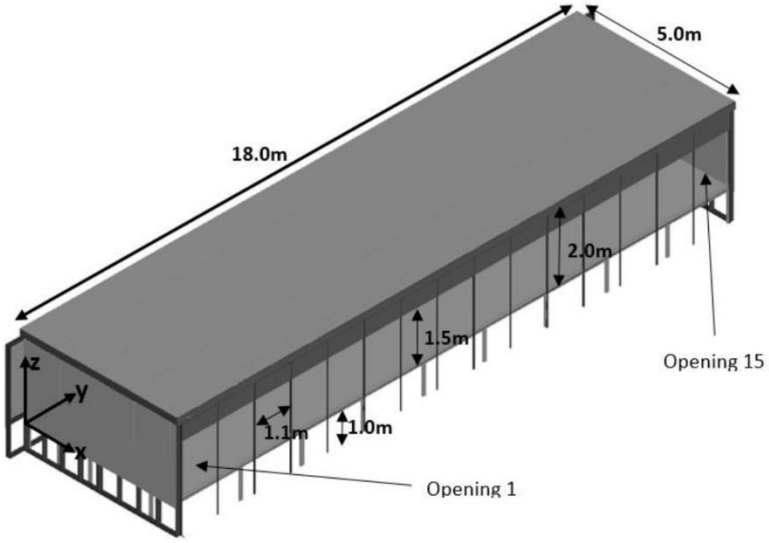

Figure 13- Overview of the compartment (Extracted from [18])

3.1.1 Openings and shutters

Front side of the compartment was divided into 15 openings, each 1.1 m wide. Each couple of openings were separated by 0.1 m thick square columns. Detailed numbering and location of the openings is as shown in Figure 14.

Series of custom built adjustable shutters covered openings. Shutters designed to be as same width as openings, with height of 2 m. Same numbers were assigned to shutters.

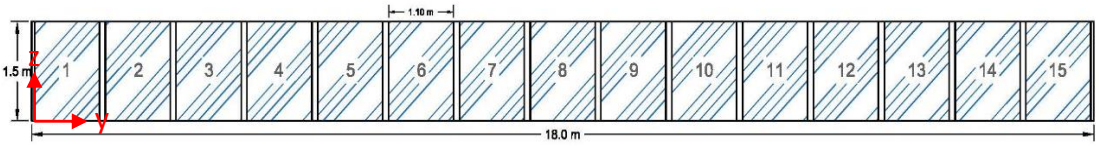

Figure 14- Openings demonstrated as hatched surfaces, all located at x = 5m

Shutters were removed systematically during some experiments to simulate window breakage for various ventilation scenarios.

3.1.2 Gas burners

In first 10 experiments, fire in the compartment was simulated by means of 12 sand gas burners. Propane was supplied to each burner and controlled precisely through two mass flow controllers. Gas burners were used to simulate various fire scenarios including traveling, growing and fully developed fires. Duration of operation of each gas burner was dependent on the designed fire scenario for different experiments.

As shown in Figure 15 each gas burner was encased in a 0.5 m square metal box with height of 0.35 m, filled with gravel to simulate diffusion flames.

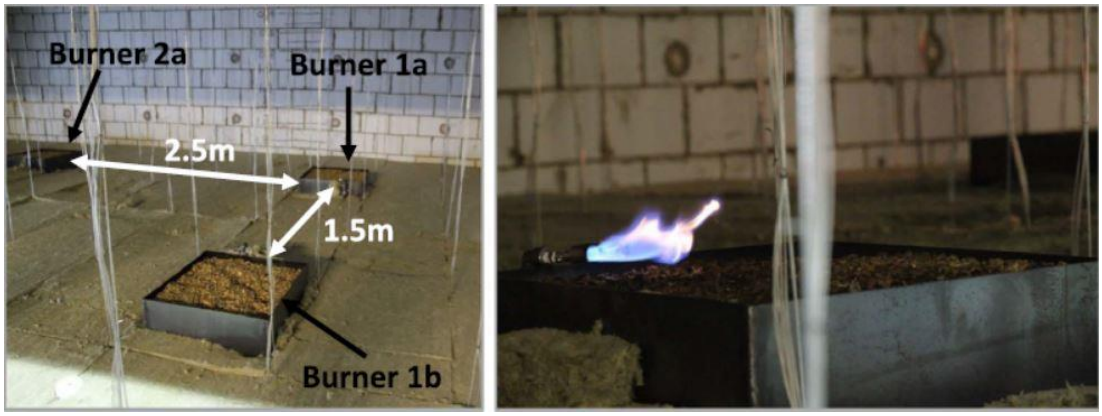

Figure 15- Gas burners positioning- Extracted from [18]

Burners were uniformly distributed in 6 pairs, each with a central distance of 3m from adjacent pair. Figure 16 shows gas burner distribution within the compartment. As shown in this figure, burner pairs were labeled from 1 (closest to right wall) to 6 (closest to left wall).

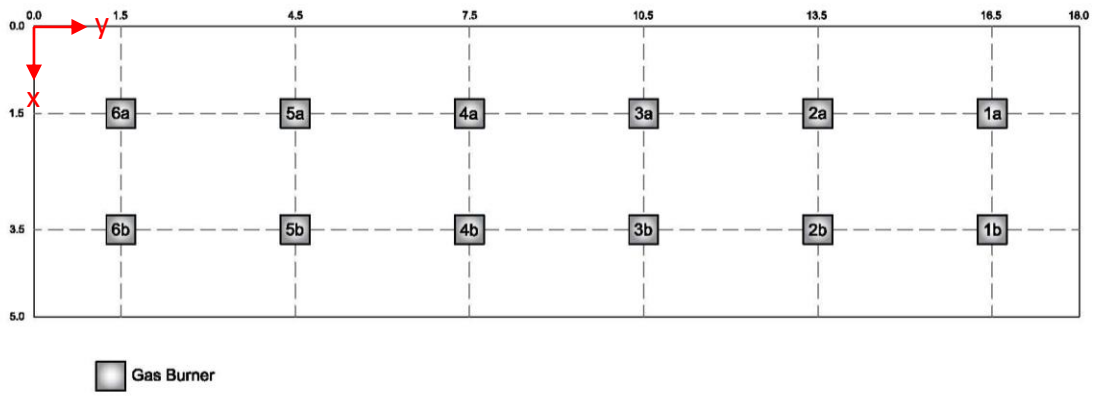

Figure 16- Gas burner layout on compartment floor- Plan view

3.2 Fire modes

3 different modes of fire, along with 3 ventilation modes, were defined to capture all possible fire scenarios inside an open compartment. Fire spread modes adapted in experiment were as following:

- Mode 1 – Spread velocity of the fire front is high enough to cover the entire area of the enclosure instantaneously.
- Mode 2 – Spread velocity of the burnout is less than the fire front therefore burning area increases as the fire develops in time.
- Mode 3 – Spread velocity of the burnout is almost identical to the fire front, therefore the area of floor which is involved in the burning process remains constant during the experiment.

In summary, fire modes conducted in the first 10 experiments (i.e. experiments which gas burners were used as heat source) were as indicated in Table 3.

Table 3- Different fire spread modes used in the experiments

Fire Spread Mode		
Mode 1	fully developed fire	$V_s \rightarrow \infty$
Mode 2	growing/ spreading fire	$V_s \gg V_{BO}$
Mode 3	Moving/ traveling fire	$V_s \cong V_{BO}$

Prior to describing different ventilation modes, it would be worth defining some of the terms used in traveling fires.

A specific kind of open compartment fire, is traveling fire. In almost all open floor plan fires, temperature has a non-homogenous profile. In the case of a traveling fire, the burning itself is not uniform as well. A traveling fire happens when only a portion of floor plan is fully involved in the fire, and flame moves across the compartment.

A large compartment fully involved fire causes high temperature profile for a relatively short duration although a traveling fire inside an open floor plan compartment can burn for hours creating lower overall average gas phase temperature. Elevated temperature during a traveling fire can be divided into two different regions; flame temperatures in near field and elevated temperature caused by the flame in far field as shown in Figure 17. As shown in this figure, the plume and areas close to it, which are areas above and adjacent to the flame, will be subsets of near field section. In contrast, ceiling jet and all other areas not close to the flame are in far field region.

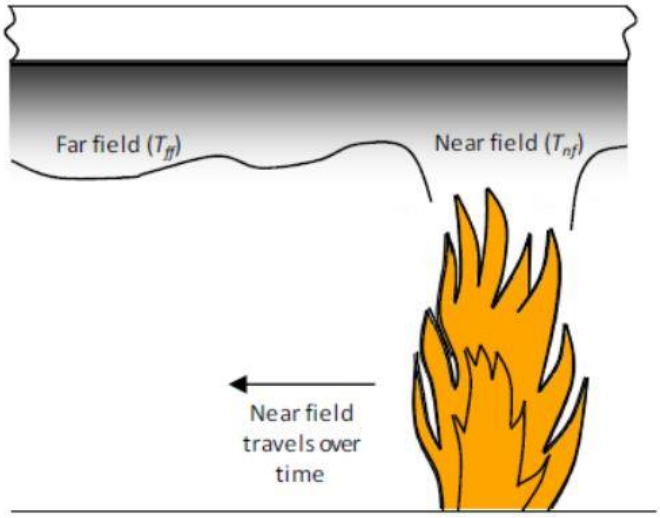

Figure 17- Schematic of a traveling fire- Extracted from [19]

3.3 Ventilation modes

As mentioned previously, removable shutters were used to simulate and control following ventilation modes (for detailed shutter layouts refer to Figure 14):

- Ventilation mode 1 – All 15 opening segments were remained in open condition during the experiment.
- Ventilation mode 2 – Segments 3, 8, and 13 were remained open throughout the test. All other openings were covered with shutters during the experiment.
- Ventilation mode 3 – Experiment started with segments 13, 14, and 15 initially open and shutters were removed one at the time during the test. Number of removed shutters depended on the duration of each experiment. Two different shutter speed patterns were applied to simulate window breakage. This ventilation mode simulated transient condition with following patterns:
    a) Subsequent sections shutters removed with the speed ahead of fire front. In this specific ventilation mode, shutters were removed with speed of 1 per minute.

b) Subsequent sections shutters removed with the speed behind fire front. This ventilation mode was simulated by removing 1 shutter per 5 minutes in the experiment.

Table 4 represents a summary of various ventilation modes conducted in the experiments, also detailed description of the modes can be find in [18].

Table 4- Different ventilation modes used in the experiments

Ventilation Mode		Segment Details
Mode 1	Static over-ventilated	All open
Mode 2	Static under-ventilated	3, 8, and 13 open
Mode 3	Transient	13, 14, and 15 initially open- 1 shutter removed per minute
		13, 14, and 15 initially open- 1 shutter removed per 5 minutes

3.4 Measured parameters and relevant instrumentations

A detailed description of the instrumentation used in the experimental enclosure is described by Hidalgo et al. [18]. The compartment was instrumented as dense as it was practical to obtain accurate results. More than 2000 sensors were used inside the compartment to measure different parameters, including thin skin calorimeters, thermocouples, velocity probes, mass flow controllers, and video cameras. Table 5 represents a brief description of some of the instrumentations which are related to this study.

Table 5- Relevant test instrumentation

Measured Parameter	Sensor Type	Location in Compartment	Number of Sensors
Gas Phase Temperature	Thermocouple	Interior gas phase	1624
		Openings	75
Incident Heat Flux	TSC	Interior Surfaces	165
Gas Flow Velocity	Bi-Directional Velocity Probe	Openings	30

3.4.1 Gas phase temperature

1.5 mm bead type K thermocouples were used to measure spatial and temporal gas phase temperatures within the compartment. Thermocouples were placed on thermocouple trees all over the compartment. Each internal tree consists of 8 thermocouples in different heights (0.3, 0.6. 0.9, 1.2, 1.4, 1.6, 1.8, and 1.95 m). Also, additional thermocouple trees were placed in all openings each consist of thermocouples in heights of 0.18, 0.43, 0.68, 0.93, and 1.18 m. Each internal thermocouple tree was placed with a distance of 0.6 m along the length and 0.7 m in the depth from adjacent tree. Elevation and plan view of internal thermocouples in the compartment are shown in Figure 18, and Figure 19, respectively.

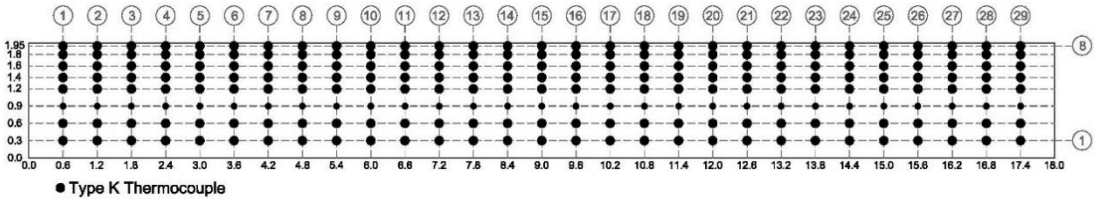

Figure 18 – Internal thermocouple locations- elevation view

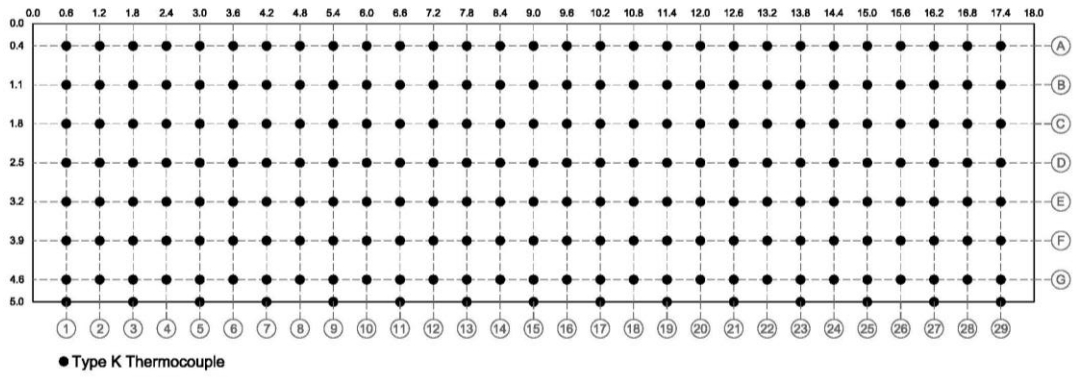

Figure 19- Location of thermocouple trees both inside the compartment and in openings- plan view

3.4.2 Incident radiant heat flux

Thin skin calorimeters were used to measure incident heat flux at the boundaries of the compartment. These instruments were made of 304b stainless steel with dimensions of 10 mm in diameter and 0.5 mm thickness. The thermocouple used in the thin skin calorimeters was a Type KX thermocouple and was welded to the center of unexposed side of the instrument. Each stainless steel plate was placed on an 80 mm in diameter and 50 mm thick Ceraboard® and thermocouple wires passed through the Ceraboard® core. Figure 20 shows an assembled thin skin calorimeter with mentioned characteristics.

Figure 20- Real assembled thin skin calorimeter - Extracted from [20]

Total number of 165 thin skin calorimeters were used on 5 surfaces of the compartment. This includes 3 rows of 15 thin skin calorimeters along the length of the compartment on rear wall, ceiling, and floor (total of 45 TSCs on each surface), and 3 rows of 5 thin skin calorimeters on each side wall (total of 15 on each side surface). Figure 21, Figure 22, and Figure 23 show an overview of locations of thin skin calorimeters on different surfaces of the compartment.

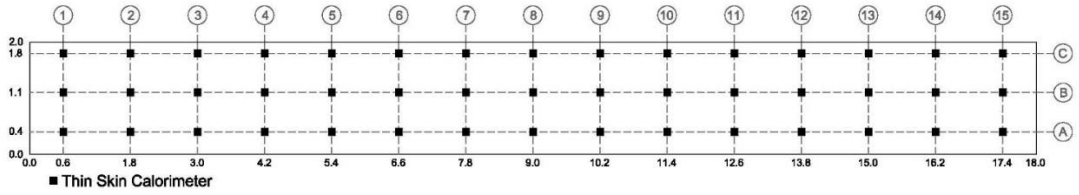

Figure 21- Thin skin calorimeters layout in back wall- Elevation view

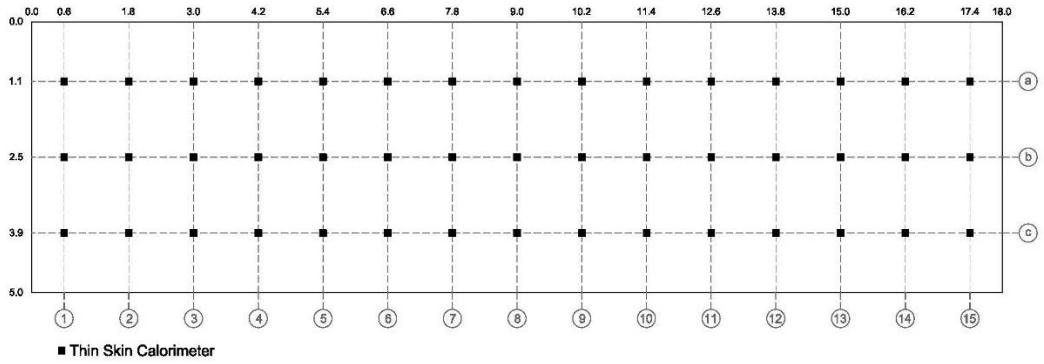

Figure 22- Thin skin calorimeters layout in floor and ceiling- Plan view

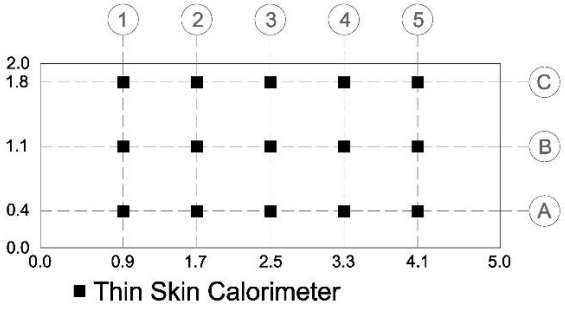

Figure 23- Thin skin calorimeters layout in side walls- Elevation view

3.4.3 Gas flow velocity

A detailed description of velocity probes' location and orientation is presented by Hidalgo et al. [18]. Each of the 15 openings of the compartment was equipped with couple of bi-directional velocity probes in two different heights. Heights of the velocity probes were set to be at 0.22 m and 1.23 m from base of the compartment in order to capture inflow and outflow velocities, respectively.

Velocity probes were designed such that those located at lower height captured cold air flows getting into the compartment. Hot gases and smoke leaving the compartment due to buoyancy from upper parts of the openings were captured by upper velocity probes. Velocity probes were designed and orientated such that, they were only capable of measuring velocity from flows perpendicular to openings.

3.5 Research Approach

This section describes the method used to quantify the heat delivered to the solid phase boundaries. Net heat flux was calculated considering both radiative and convective heat flux imposed to the compartment surface. Quantitative values for parameters in this section are provided in details in following chapter.

3.5.1 Net heat flux calculation

Net heat flux was divided into two radiant and convective categories and each category was studied individually. Net heat flux was calculated by addition, or subtraction of radiative and convective heat fluxes in hot, and cold parts of the compartment, respectively.

3.5.1.1 Incident radiant heat flux

As mentioned previously, thin skin calorimeters were used on all surfaces of the compartment to measure incident radiant heat flux. A detailed description of required calibrations for thin skin calorimeters is described by J.P. Hidalgo et al. [20]. Incident radiant heat flux was calculated according to equation 17 [20].

$$\dot{q}''_{inc} = \frac{1}{\alpha_{disc}(1-C)}\left[\frac{m_{disc}}{S_{disc}} c_P \frac{dT_{disc}}{dt} + \varepsilon_{TSC}\sigma T_{disc}^4 + h_c\left(T_{disc} - T_g\right)\right] \quad (17)$$

Based on this correlation, incident radiant heat flux can be approximated as a function of thin skin calorimeters' temperature measurements, as well as gas phase temperature measured in adjacent thermocouples for each time step.

Table 6 provides a brief definition of the parameters used in equation 4, their units, and assigned values.

Table 6- Parameters and their values used for incident radiant heat flux calculation

Parameter	Definition	Unit	Value
$\dot{q}''_{inc}$	Incident radiant heat flux	$W.m^{-2}$	To be calculated
C	Correction factor for TSC	-	Temperature dependent
α_{disc}	TSC metal disc absorptivity	-	1.0
m_{disc}	TSC metal disc mass	kg	3.06e-4
S_{disc}	TSC metal disc surface area	m^2	7.854e-5
c_P	TSC metal disc specific heat	$J.kg^{-1}.K^{-1}$	Temperature dependent
T_{disc}	TSC temperature	K	Time dependent
ε_{TSC}	TSC metal disc emissivity	-	0.4
dt	Time differential	s	1.0
σ	Stefan-Boltzmann constant	$W.m^{-2}.K^{-4}$	5.67e-8
h_c	Convective heat transfer coefficient	$W.m^{-2}.K$	16

$\boldsymbol{T_g}$	Gas temperature at the vicinity of boundary	K	Time dependent

Temperature dependencies mentioned in previous table are temperature of the thin skin calorimeter disc.

According to Hidalgo et al. [20], C is representative of conduction correction factor for heat flux calculations which is an approach to overcome some uncertainties through calibration procedures. The correction factor for the specific thin skin calorimeters used in these experiment series can be calculated as following:

$$C = -1.8^{-5} \times T_{disc} + 6.37731^{-1} \quad (18)$$

Where T_{disc} is thin skin calorimeter temperature in ˚C.

Also, specific heat capacity of 304b stainless steel, used in thin skin calorimeters, can be calculated from following correlation.

$$c_P = 450 + 0.28\,T_{disc} - 2.91^{-4}\,T_{disc}^2 + 1.34^{-7}\;T_{disc}^3 \quad (19)$$

Where T_{disc}, same as previous correlation, represents thin skin calorimeter temperature in ˚C.

By substituting required parameters in equation 4, incident radiant heat flux can be calculated.

3.5.1.2 Convective heat flux

In order to calculate the net heat flux imposed to the compartment structure, convective heat transfer needed to be taken into account.

Following formula was adopted to calculate convective heat transfer inside the compartment [15].

$$\dot{q}''_{conv} = h_c\,(T_g - T_{disc}) \quad (20)$$

Where $\dot{q}''_{conv}$ represents the heat flux through convection $[W/m^2]$, h_c is the convective heat transfer coefficient $[W/m^2K]$, T_g, and T_s are gas phase, and solid phase temperatures [K], respectively.

Convective heat transfer coefficient was approximated using correlations between Nusselt and Reynolds number from literature [15]. Final heat transfer coefficient value used in convection calculations was the h_c at location of neutral plane.

$$h_c = \frac{Nu.k}{L} \tag{21}$$

Where k is thermal conductivity of gases (30e3 $[W/m.K]$), L represents the characteristic length [m], and Nu is the local Nusselt number corresponding to a flat plate in parallel flow.

$$Nu = 0.332 Re^{\frac{1}{2}} Pr^{\frac{1}{3}} \tag{22}$$

$$Re = \frac{vL}{\upsilon}, \text{and Pr} = \frac{\upsilon}{\alpha} \tag{23}$$

Where Re, and Pr are Reynolds and Prandtl number, respectively, v represents the fluid velocity at neutral plane height $[m/s]$, υ is kinematic viscosity (20.92e6 $[m^2/s]$), and α represents thermal diffusivity (29.9e6 $[m^2/s]$) .

Average gas phase temperature was calculated based on data measured in thermocouples located in the openings. This temperature was adopted as the basis temperature for input parameters. Considering aforementioned values, Prandtl number resulted to be 0.7.

In order to calculate Reynolds number and therefore heat transfer coefficient, velocity of gases needed to be calculated.

Using aforementioned equations with the specific measurements corresponding to each experiment, different values for the convective heat transfer coefficient will be calculated. The specific values will be presented in following chapter.

3.5.1.3 Velocity calculation

Each opening of the compartment was equipped with two velocity probes located at heights of 0.22, and 1.23 m. Velocity calculation was necessary to calculate Reynolds number, followed by Nusselt number and subsequently to obtain heat transfer coefficient.

Raw voltage data from the experiment was treated and converted into velocity using following correlation.

$$v = \gamma\sqrt{\frac{2\Delta P}{\rho_{air}}} \tag{24}$$

Where γ the McCaffrey probe constant (0.94) is, ΔP is the change in pressure [Pa], and ρ_{air} represents density of air $[kg/m^3]$. Ambient gas velocity affected the velocity probe measurements prior to start of the experiment, such that the recorded voltage was not zero when the test started. In order to reduce the effect of predefined values in the probes, mean value of first 50 measured data points (prior to start of the experiment), was calculated and subtracted from the raw data, for each probe individually. Outcome which resulted to be voltage difference from the baseline then converted to pressure difference [21].

$$\Delta P = Voltage\ difference \times (-10) \tag{25}$$

Value of (-10) presents the calibration coefficient for velocity probes used in these experiments.

Other required parameter for velocity calculation is density of air which can be calculated using following equation:

$$\rho_{air} = \frac{M_{air} P_{atm}}{R T_g} \quad (26)$$

Where M_{air} is the molar mass of air (29 [kg/mol]), and P_{atm} is the atmospheric pressure (101325 [Pa]). R represents the universal gas constant (8314.5 [J/$mol.K$]), and T_g is gas phase temperature [K] measured in thermocouple adjacent to each velocity probe.

By substituting air density and pressure difference obtained from equations 12 and 13 into equation 11, velocity was calculated for each probe at each time step. Quantitative velocity values are provided in details in following chapters.

Velocity profile was assumed to be linear over the height of opening. Couple of reasons made this assumption reasonable:

- A general approximate heat transfer coefficient needed to be taken into account.
- Velocity measurement inside the openings of the compartment was coarse, therefore a detailed analysis on the heat transfer coefficient was not reasonable.

3.6 Representative Experiments

Among series of 12 ETFT tests, some were chosen to be basis of analysis for this paper. A detailed description of fire and ventilation conditions used in chosen experiments, in addition to the process of each experiment is provided in this chapter.

Fire and ventilation modes were defined and summarized in Table 3 and Table 4. In addition, burners' locations is presented in Figure 16.

3.6.1 Experiment 3

Experiment 3 was designed to be an over-ventilated traveling fire. This specific scenario was designed with a Mode 3 fire and Mode 1 ventilation condition. Over ventilation condition was achieved as all 15 openings were open during the entire experiment (i.e. no shutter was placed on any of the openings).

Figure 24 represents the heat release rate graph of the fire. Fire started in the right corner of the compartment in burners 1a and 1b. Each pair of burners were turned off after 150 seconds of operation and fire moved to the adjacent pair afterwards. 1 MW fire shown in Figure 24 was simulated by turning a pair of burner off while igniting the adjacent pair almost instantaneously. Each number on top of the red heat release rate line in Figure 24 represents the burners' number which were operating in labeled duration.

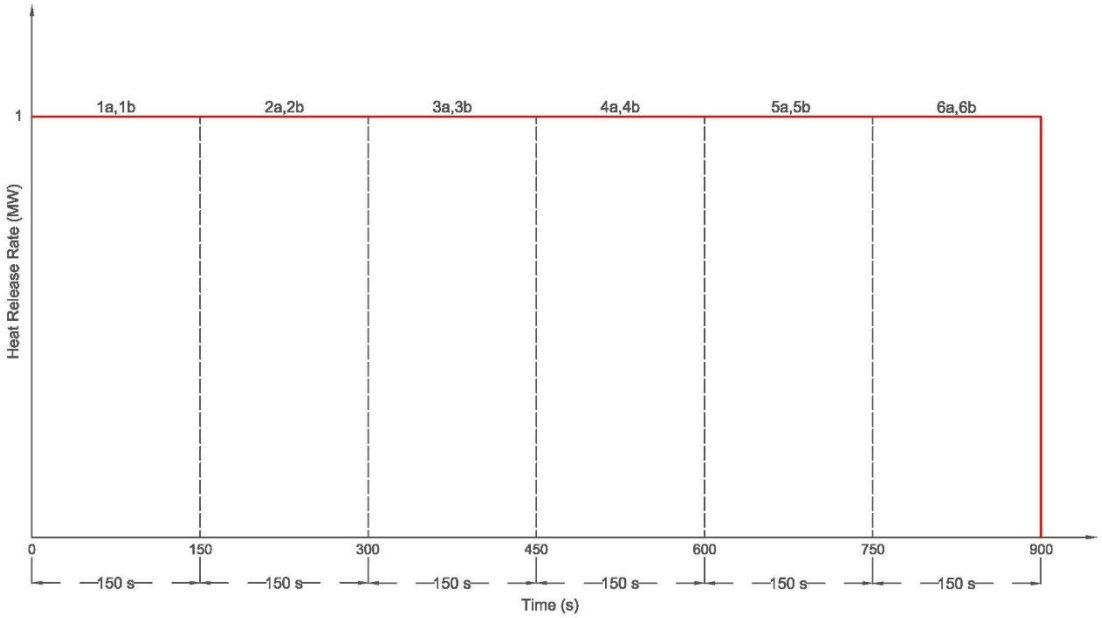

Figure 24- Experiment 3 heat release rate- numbers on the red line present the burners which were operating in labeled time periods

Also, Table 7 shows the ignition sequence of the burners during experiment 3. As a reference, burners 1a and 1b were located at right side of the compartment and burners 6a and 6b were on the left.

Table 7- Ignition sequences in experiment 3

Burner	Ignition Time [s]	Extinction Time [s]
1a	0	150
1b	0	150
2a	150	300
2b	150	300
3a	300	450
3b	300	450
4a	450	600
4b	450	600
5a	600	750
5b	600	750
6a	750	900
6b	750	900

It would be worth mentioning that required experimental data to plot heat release rate graphs was obtained from mass flow controllers' measurements and provided graphs in this paper only demonstrates the smoothened data.

3.6.2 Experiment 6

Experiment 6 designed to be an under-ventilated traveling fire (i.e. Mode 3 fire and Mode 2 ventilation condition). Heat release rate of fire designed to be exact same as Experiment 3 (as shown in Figure 24). Same procedure was used to simulate the fire. Only difference between this test and Experiment 3 is the ventilation condition. A static under-ventilated condition was simulated through entire experiment. Openings, 3, 8, and 13 were open during the test and all other openings were covered by shutters.

3.6.3 Experiment 9

This experiment was designed with a Mode 3 ventilation, and a Mode 3 fire condition. A traveling fire was simulated during this experiment. Fire started in the right corner of compartment in burners 1a and 1b and traveled to the left side of the compartment with heat release rate pattern as shown in Figure 25. Numbers labeled on the red heat release rate line indicate the burners which were operating in corresponding time periods.

Two different heat release rate values of 1 MW and 0.5 MW simulated during this experiment. Each 1 MW heat release rate fire in Figure 25 simulated by operation of a pair of burners together, and 0.5 MW fires happened when a single burner was lit. For instance, first 60 seconds of Figure 25 with 1 MW heat release rate, corresponds to fire in burners 1a and 1b. Burner 1b was then turned off almost 60 seconds after start of experiment and burner 1a operated singularly for the next 690 seconds to maintain 0.5 MW fire inside the compartment. Burner 6b did not ignite during this experiment and burner 6a was used to maintain the minimum heat release rate of the fire (0.5 MW) in the last stage of the test.

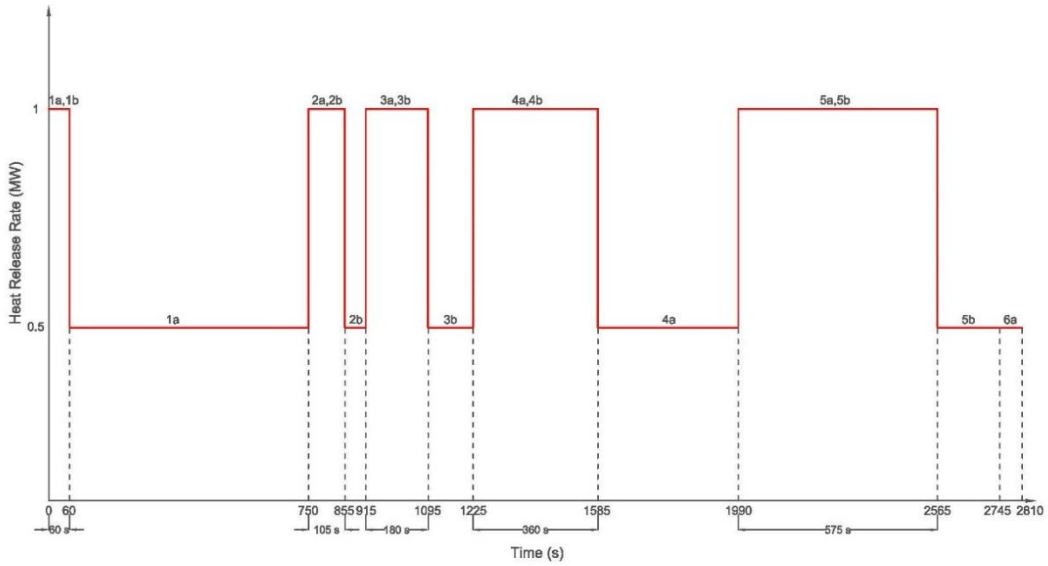

Figure 25- Experiment 9 heat release rate- numbers on the red line present the burners which were operating in labeled time periods

Table 8 shows the ignition sequence of the burners during experiment 9.

Table 8- Ignition sequences in experiment 9

Burner	Ignition Time [s]	Extinction Time [s]
1a	0	750
1b	0	60
2a	750	855
2b	750	915
3a	915	1095
3b	915	1225
4a	1225	1990
4b	1225	1585
5a	1990	2565
5b	1990	2745
6a	2745	2810
6b	-	-

As mentioned previously, shutters were designed to simulate different ventilation scenarios during the tests. A Mode 3 ventilation condition was designed for this specific experiment. As shown in Figure 26, openings 13, 14, and 15 were initially open (i.e. no shutter was placed in these openings). Experiment started in an under-ventilated condition and as the fire traveled from right to left side of compartment, shutters were

removed to simulate breakage of the windows. Shutters were planned to be removed at the speed of 1 shutter per minute, although due to rail system malfunction in opening 12, a slight delay happened in the procedure.

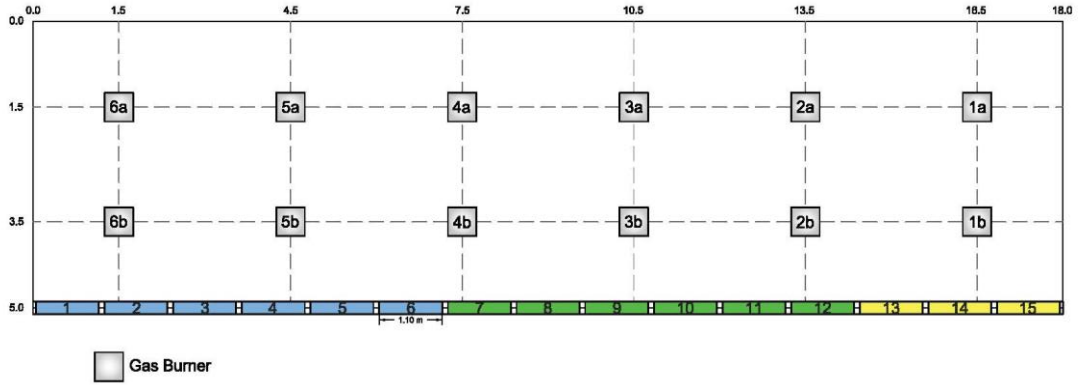

Figure 26- Plan view of shutters and gas burners layout for experiment 9 – Rectangular boxes marked as yellow represent the shutters which were open from the start of the experiment, green shutters were removed during the test and blue shutters remained closed through the time of experiment.

By the end of the experiments, 6 shutters were removed and 7 shutters located in the left openings remained closed. Table 9 shows the detailed shutter schedule. Numbers in brackets demonstrates the time which took mentioned shutters to be completely removed.

Table 9- Detailed shutter shedule- Experiment 9

Event	**Time [s]**
Shutter 12 half opened	830 [+15s]
Shutter 12 fully opened	991 [+10s]
Shutter 11 opened	1111 [+32s]
Shutter 10 opened	1143 [+47s]
Shutter 9 opened	1190 [+22s]
Shutter 8 opened	1483 [+30s]
Shutter 7 opened	2490 [+30s]

3.6.4 Experiment 10

Experiment 10 was designed to be a Mode 3 fire (i.e. traveling fire) and Mode 3 ventilation. Same as previous experiment, fire started in the right corner of the

compartment in burners 1a and 1b and traveled to the left side. Figure 27 shows the heat release rate pattern of this experiment. Numbers on the red heat release rate line represent the burners which were operating in corresponding duration to keep the heat release rate to designed value. Some of the differences between considered experiments is the speed which the fire moves to next burner sets as well as total duration of fire. In this experiment fire was kept in the maximum 1 MW heat release rate for long period of time although it moved to adjacent burners after each 150 seconds time period. In addition, unlike previous test, burners 6a and 6b were both ignited in last stages of the experiment to reach the maximum fire heat release rate.

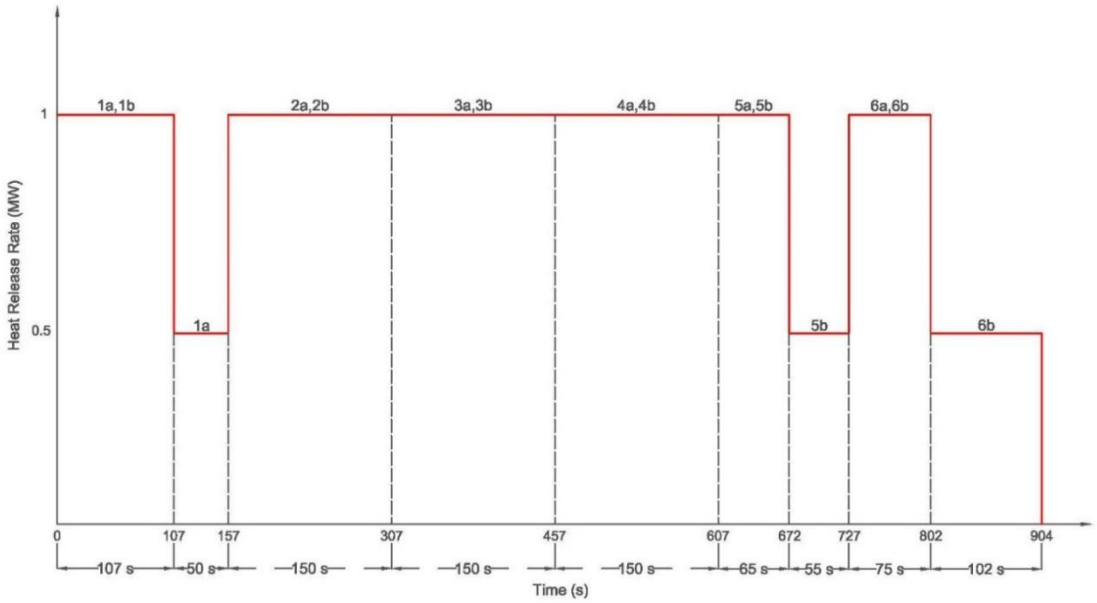

Figure 27- Experiment 10 heat release rate- numbers on the red line present the burners which were operating in labeled time periods

Table 10 shows the ignition sequence of the burners during experiment 10.

Table 10- Ignition sequence in experiment 10

Burner	Ignition Time [s]	Extinction Time [s]
1a	0	157
1b	0	107
2a	157	307
2b	157	307
3a	307	457
3b	307	457
4a	457	607
4b	457	607
5a	607	672
5b	607	727
6a	727	802
6b	727	904

Ventilation condition was set to be Mode 3 (i.e. transient ventilation condition). Experiment started with no shutters in openings 13, 14, and 15 and shutters were removed with the speed of 5 per minute. Since the duration of the experiment was short, only two shutters were removed from the openings. Shutter 12 was removed 300 seconds after the start of the experiment and shutter 13 was removed 600 seconds in the test. Figure 28 shows location of burners in addition to shutters details. Shutters labeled in yellow were open when the test started, green blocks show the shutters which were removed during the experiment, and blue blocks remained closed.

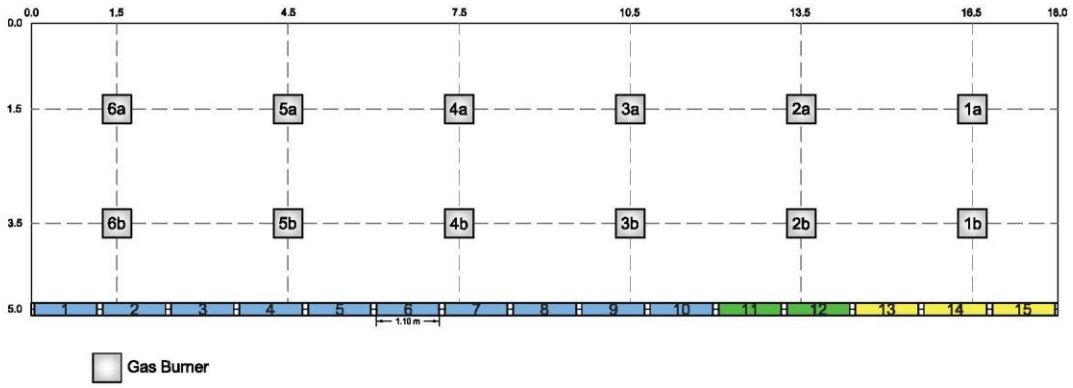

Figure 28- Plan view of shutters and gas burners layout for experiment 10 - Rectangular boxes marked as yellow represent the shutters which were open from the start of the experiment, green shutters were removed during the test and blue shutters remained closed through the time of experiment

Chapter 4: Data Analysis

4.1 Incident Radiant Heat Flux

Raw temperature data obtained from thin skin calorimeters and thermocouples in different experiments were treated and analyzed. Heat flux was calculated as mentioned in previous chapter. Results from previously mentioned experiments are provided with the sequence as they were analyzed (Experiments 9 followed by experiments 3, 6 and 10).

In order to study the heat flux in details, data obtained from thin skin calorimeters located on back wall with height of 1.1 m, and their corresponding thermocouples were chosen to be basis for raw data analysis and heat transfer calculations. All other thin skin calorimeters, on back wall and other surfaces of the compartment, were used for verification and further calculations.

4.1.1 Experiment 9

Incident radiant heat flux was calculated and studied based on obtained data from thin skin calorimeters located on each surface, and their adjacent thermocouples inside the compartment. Spatial distribution of radiative heat flux was plotted for all surfaces

inside the compartment in different time steps. Figure 29 shows the radiative heat flux imposed to compartment surfaces almost 60 seconds after the start of the experiment. Each part of this graph shows one of the surfaces of the compartment and the radiative heat flux which was imposed to it at this time step. Overall dimension of each part in Figure 29 shows the dimension of the considered surface, and the contoured part shows the area which heat flux data was available.

Almost 60 seconds after start of the experiment, gas burners 1a and 1b, located in right side of the compartment, were operating and fire had heat release rate of 1 MW (refer to Figure 16 for burners' detailed location and Figure 25 for fire heat release rate of this experiment). Since the fire at chosen time step was located in the right side of the compartment, high radiative heat flux in the contours of right wall (Figure 29 (e)) as well as areas in other surfaces which were close to the operating burner location can be seen.

In contrary, left wall (Figure 29 (d)) which was located far from the fire location at this time, captured radiative heat fluxes which are almost negligible. In addition, radiative heat fluxes decreased to lower values in areas far from the fire origin therefore as the relative distance of a considered point in compartment with the operating burner increases, a considerable decrease in the incident radiant heat flux value can be observed. In other words, in near field areas, high heat flux values were captured, although in far field, this value considerably decreased.

Same approach adopted to show the radiative heat flux in other time steps and study the near field and far field heat fluxes and the distance of the mentioned locations from the fire origin. Figure 30 represents the same concept almost 2565 seconds after the

start of the experiment when burners 5a and 5b were operating. Same as before, fire had heat release rate of 1 MW although area of the floor involved in fire had been moved to left side of the compartment. As shown in this graph, maximum radiative heat flux location has moved to areas closer to burner 5 and in contrast with Figure 29, left wall has higher heat flux value than the right wall (Figure 30 (d) and (e)).

As expected and according to the results, incident radiant heat flux on compartment surface, in a specific location, reaches its maximum value when the fire is in near field and decreases to a lower value in far field.

Mentioned time steps were chosen to be moments before the decrease in fire heat release rate from 1 MW to 0.5 MW (refer to Figure 25 for detailed heat release rate graph). Reason was to make sure that the burners had operated the most, and temperature and heat transfer in considered location reached the steadiest possible condition in the compartment for a specific period.

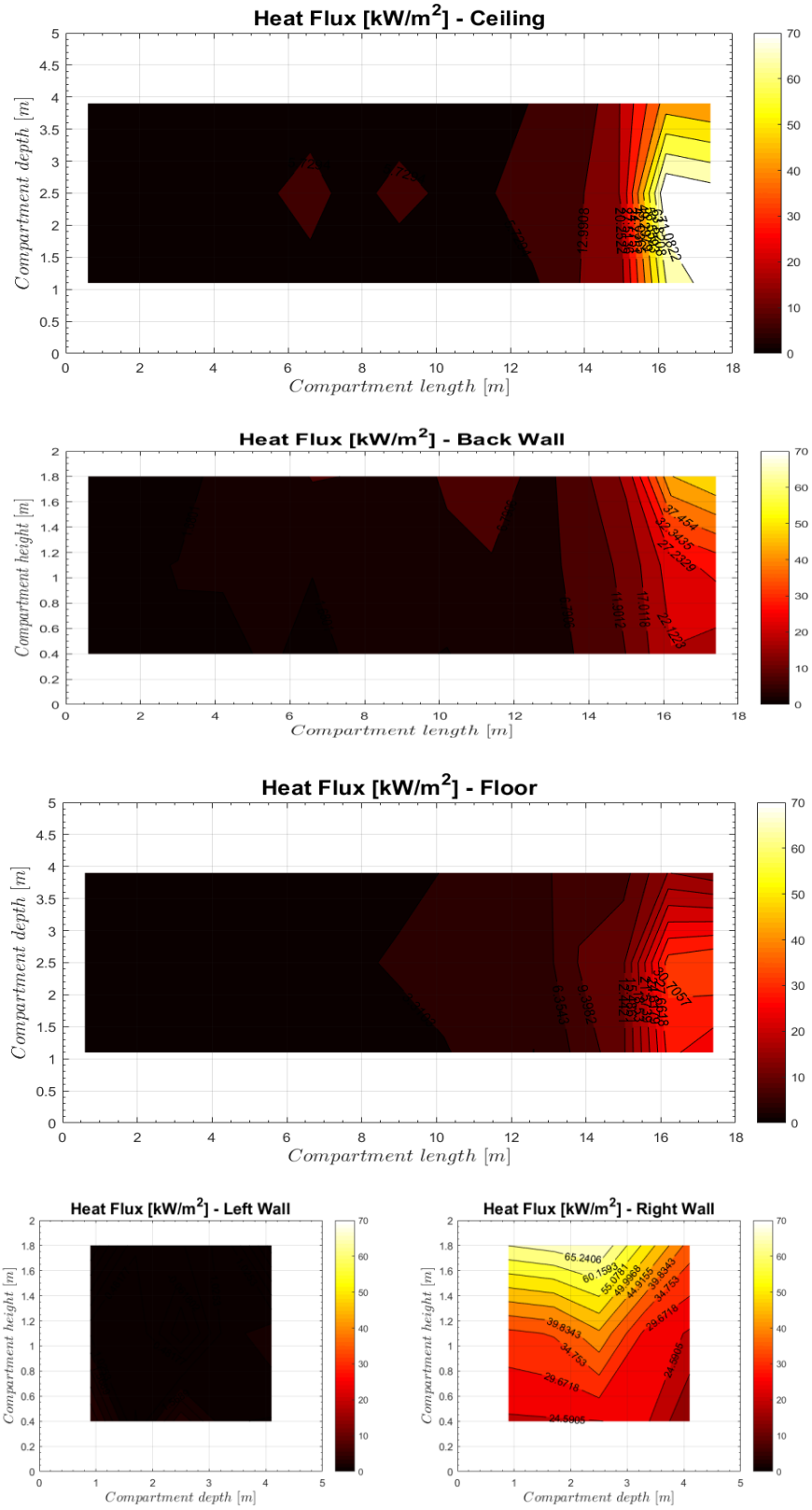

Figure 29- Radiant heat flux 60 seconds after start of the experiment

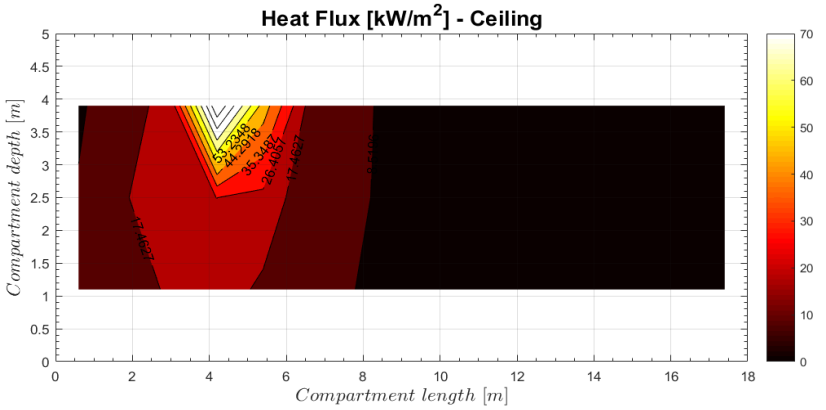

(a)

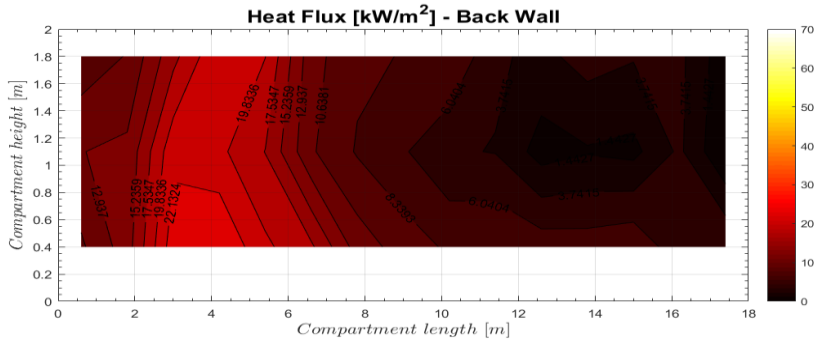

(b)

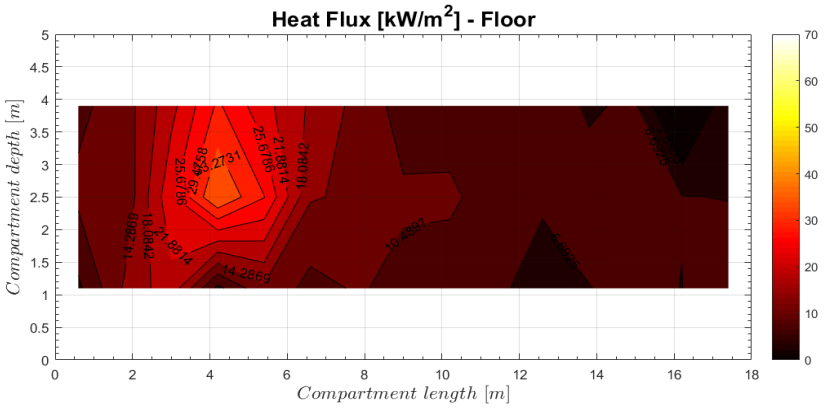

(c)

(d)

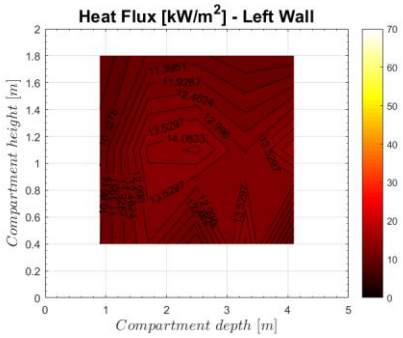

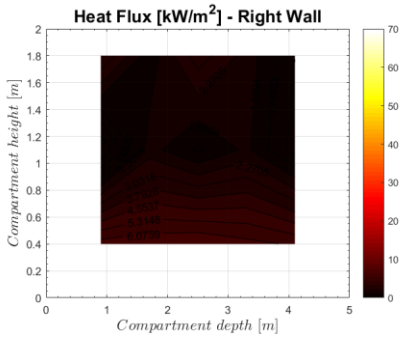

(e)

Figure 30- Radiant heat flux 2565 seconds after start of the experiment

In order to further study the radiative heat flux to figure out how it evolves in time, a specific thin skin calorimeter in the back wall was considered. Thin skin calorimeter located at node 12B in back wall and its adjacent thermocouple were the chosen instruments. Detailed description of location of instruments was provided previously although Figure 31 visualizes relative distance of the considered thin skin calorimeter and the burners.

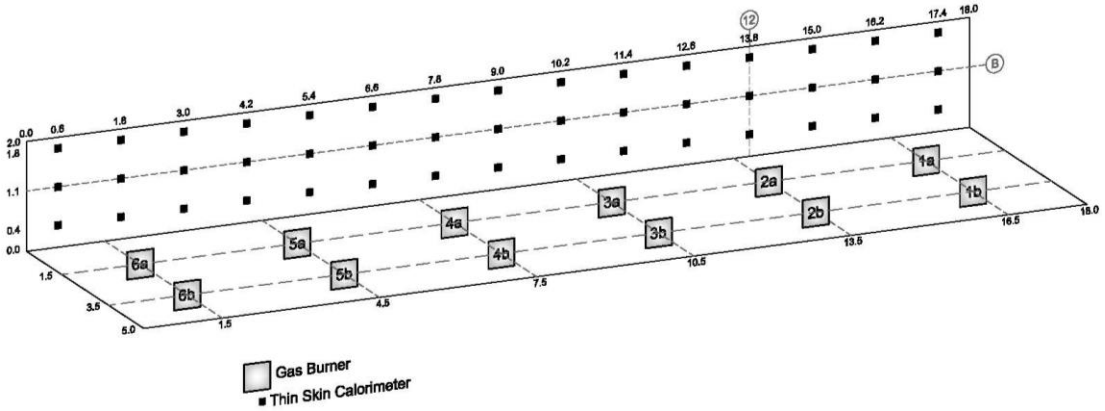

Figure 31- Node 12B and its distance with the burners

Figure 32 represents radiant heat flux evolution in the considered thin skin calorimeter. First small protuberance in Figure 32 corresponds to start of the experiment and duration when burners 1a and 1b were both ignited. This thin skin calorimeter is not close enough to burner 1 to capture a near field heat flux although according to the figure, it got slightly affected by fire. Heat flux then drops to a lower value after almost 60 seconds, which corresponds to the time when burner 1b turned off. Closest burners to this node were 2a and 2b, located at y = 13.5 m in the compartment. As expected, heat flux reached a maximum value almost at the same time when both burners 2a and 2b were ignited, and stayed in this maximum heat flux value (with slight fluctuations) for the duration when mentioned burners were operating. In other words, near field heat

flux duration was caused while burners 2a and 2b were operating. As fire traveled on the floor, distance between burners and considered thin skin calorimeter increased therefore mentioned point moved to far field area of fire. Some fluctuations can be seen in heat flux pattern in far field areas which means heat flux was affected by radiation although did not reach the maximum value.

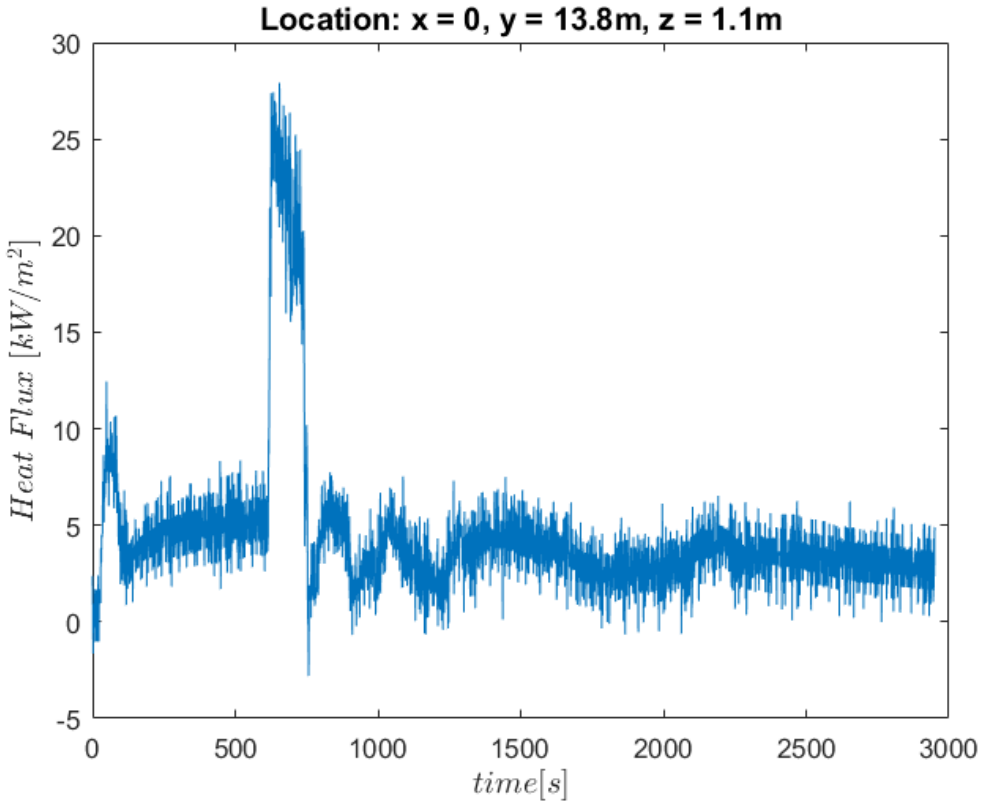

Figure 32- Radiant heat flux evolution in a TSC located on back wall- Experiment 9

According to Figure 25, burners 2a and 2b were operating (together) for almost 105 seconds (from 750 seconds to 855 seconds). As mentioned previously, near field heat flux range for the considered node, was captured with same duration although not in the exact same time when burners were lit.

Probable reasons for the difference between the time when heat flux graph is in maximum and the time when corresponding burners were operating according to heat release rate data would be as following:

- Data logging started earlier than the experiment itself and continued after the experiment was ended. Although in order to make the heat flux results compatible with heat release rate graph of the fire, it was assumed that start of first protuberance in graphs corresponds to start of experiment. In other words relative zero time was assumed for the graphs based on visual considerations, therefore a slight time discrepancy might be possible.
- The heat flux evolution graph (Figure 32) has been plotted based on thin skin calorimeters and thermocouples data which are considered as output data although the heat release rate graph (Figure 25) was plotted according to mass flow controllers' data sets which considered as input. Therefore this delay might be caused by the lag between input and output data.

Previous figure only shows the evolution of radiant heat flux in one of the thin skin calorimeters although all other 164 thin skin calorimeters inside the compartment were studied individually. As a result, same pattern was obtained for most of the thin skin calorimeters. Each peak in heat flux graph was almost simultaneous with operation of the closest set of burners to the considered point, i.e. time and duration of the near field heat flux in graph corresponded to duration of a 1 MW fire in the fire heat release rate data although some graphs did not follow the same pattern.

4.1.1.1 Discrepancies- A graph with two peaks

Figure 32 showed the radiant heat flux evolution over time in one of the thin skin calorimeters although in some locations of the compartment, heat flux graphs did not

follow the normal pattern. Figure 33 is an instance which shows the heat flux evolution in node 10B in back wall, located between 2nd and 3rd pairs of burners (refer to Figure 21 for thin skin calorimeters location in back wall). Two near field heat flux ranges can be seen in this graph. Value of each peak is considerably lower compared to normal near field heat flux values obtained from other thin skin calorimeters.

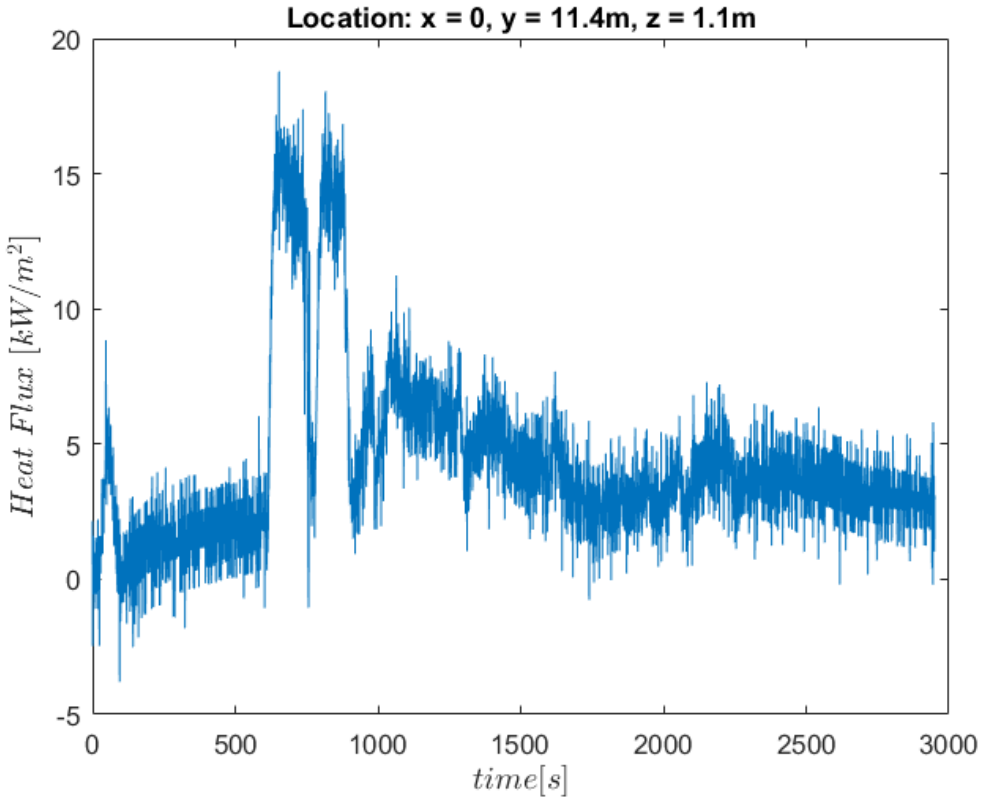

Figure 33- Radiant heat flux changes over time in a TSC located on back wall with 2 peak heat flux ranges

It would be difficult to describe the precise reason for this case although probable problem which caused this pattern would be that, first, the characteristic time scale for the structure is large, meaning the solid phase temperature does not decrease to ambient instantaneously after removing the heat source, therefore high solid phase temperature and as a result high radiant heat flux was captured after extinction of nearby burners. Based on heat release rate data, third burners ignited moments after second pair. In

other words heat release rate graph of the fire shows two peaks which unlike other periods of the fire in this experiment were close to each other therefore gas phase environment and the compartment itself did not have enough time to cool down therefore T_{disc} remained in a high value.

In addition, shutter 12 was planned to be removed in this time period although due to shutter systems malfunction and as shown in Figure 34 and Figure 35 this shutter got angled and stuck half open inside opening 12. Shutter malfunction caused slight tilt in the fire and the fire deflected from its vertical direction which might affect the temperature measurements.

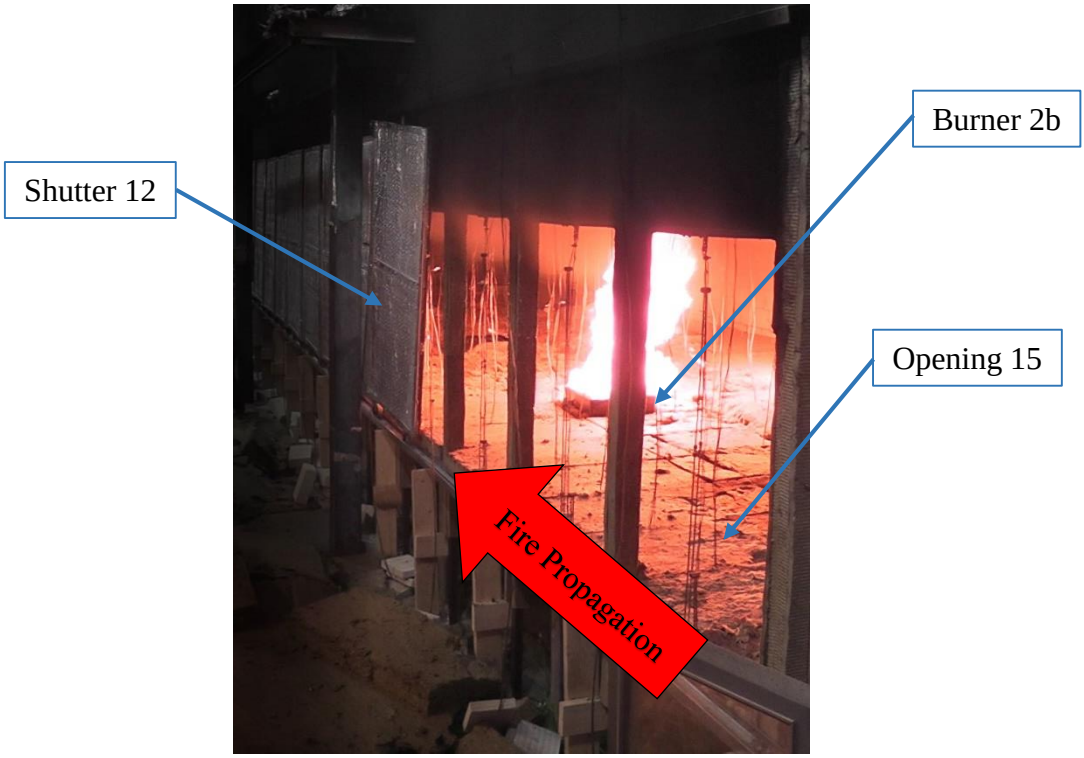

Figure 34- Shutter malfunction and fire tilt from vertical direction in burner 2

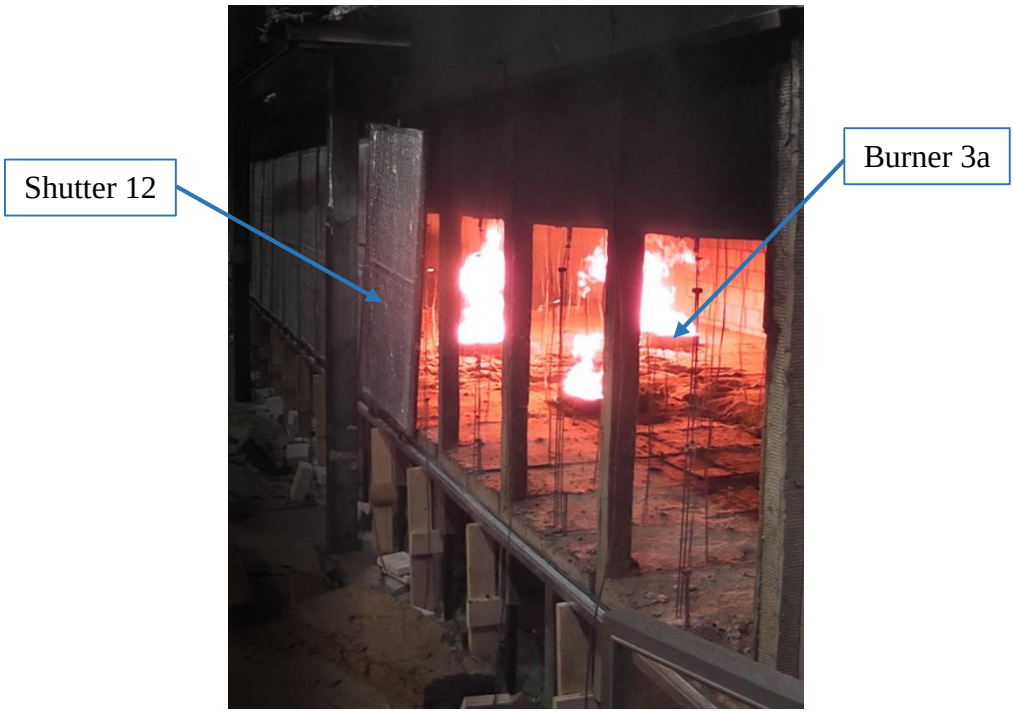

Figure 35- Shutter malfunction and fire tilt from vertical direction in burner 3

4.1.1.2 Discrepancies- Heat flux in the ceiling near openings

Other abnormal pattern obtained for radiative heat fluxes on ceiling in thin skin calorimeters located at x = 3.9 m, near openings. According to heat flux graphs, measured data in these instruments were more scattered compared to other parts of the compartment. Figure 36 shows incident radiant heat flux graphs for two different locations in the compartment both located at y = 10.2 m, one located on back wall and other one on ceiling near opening.

Probable reasons for the mentioned discrepancy would be that this thin skin calorimeter is the closest to the opening (on the ceiling), therefore heat transfer and air circulation is not as predictable as other sections of the compartment. Besides, half meter overhang which was placed on top of each opening, exacerbate the previously mentioned problem even more.

Furthermore, this experiment was done with transient shutter mode. Shutters were removed during the test which caused a change in air entrainment rates as well as temperature measurements in areas closer to openings.

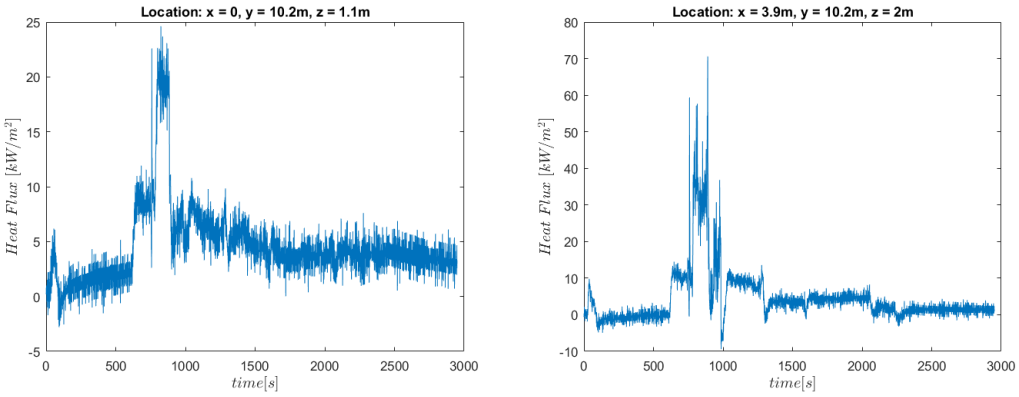

(a) (b)

Figure 36- Heat flux in two different surfaces of the compartment, both graphs obtained for thin skin calorimeters located at y =10.2 m- (a) Thin skin calorimeter on back wall at height of 1.1 m- (b) Thin skin calorimeter located on ceiling at x = 3.9 m

In order to achieve a better illustration of heat flux evolution inside the compartment at different locations, Figure 37 shows the heat flux evolution in some of thin skin calorimeters inside the compartment.

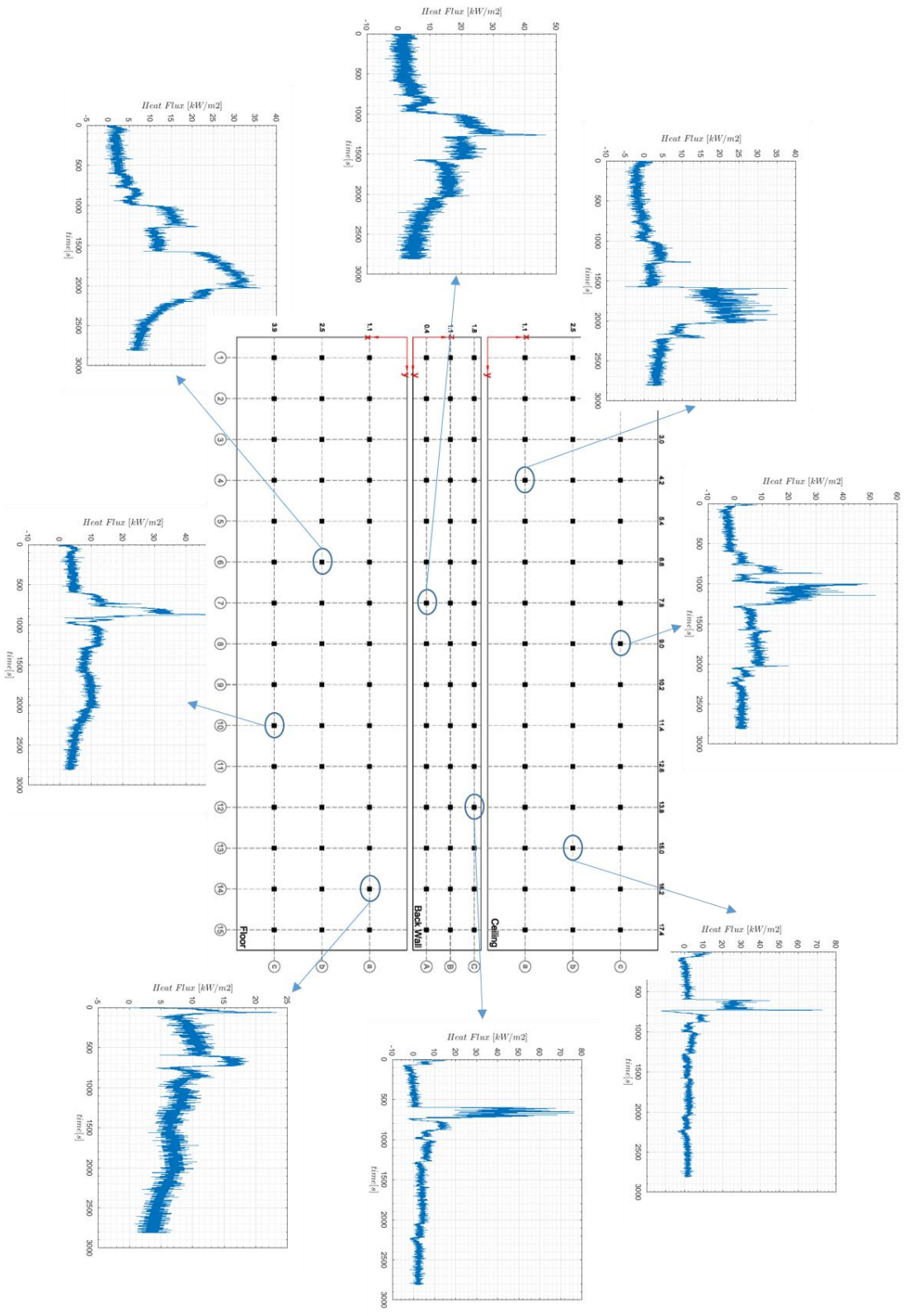

Figure 37- Heat flux evolution at different locations of the compartment- Experiment 9

4.1.2 Experiment 3

Same as previous experiment, heat flux data studied for all 165 thin skin calorimeters inside the compartment. Same incident radiant heat flux pattern was obtained. Near field heat flux was observed in all graphs with exception of some graphs capturing near field heat flux from multiple burners. Figure 38 represents the heat flux evolution in node 12B located on back wall.

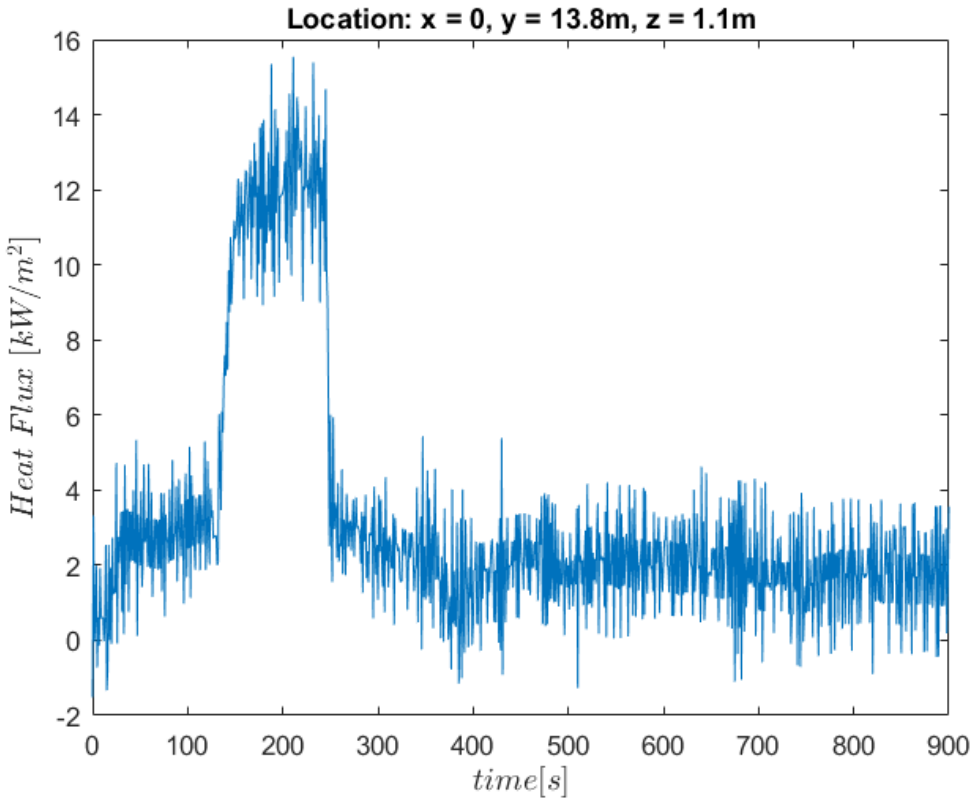

Figure 38- Heat flux pattern in thin skin calorimeter located at node 12B- Experiment 3

One of the differences between the graphs obtained from this experiment and experiment 9, is the near field heat flux values. According to this graph, near field heat flux values seems to be considerably less than previous experiment. Reason would be that experiment 3 was an over-ventilated experiment. All openings were open and the heat transfer with outside environment was at maximum level.

Other difference is the way burners which were located in far field affected a specific thin skin calorimeter data. It was seen in previous experiment that operation of each burner pair even located at the farthest from the considered thin skin calorimeter affected the heat flux evolution by producing small protuberances although in this experiment, heat flux graph seems to be considerably smoother in far field area. One possible reason would be the fully open ventilation condition of this experiment. Air entrainment in previous experiment was affected by shutter operations which was not the case in this test.

Since the dominant heat flux pattern in this experiment is same as experiment 9 and most of thin skin calorimeters captured near field heat flux from only one burner pair, while considering the fact that in this experiment fire had continuous heat release rate of 1MW while moving on the compartment floor, previously mentioned hypothesis regarding the characteristic time of the structure being large would not accurately define the reason for the graphs with two near field durations.

Same as previous experiment, some thin skin calorimeters had two near field heat flux durations, caused by different burner pairs and near field heat flux values which were slightly lower than normal pattern. Figure 39 shows one of these graphs for a thin skin calorimeter located at left side of the compartment on the back wall in node 8B.

This thin skin calorimeter was located on back wall in the middle of burners 5 and 6 on back wall and near field heat flux was captured during operation of both burners 5 (including 5a and 5b) and 6 (including 6a and 6b).

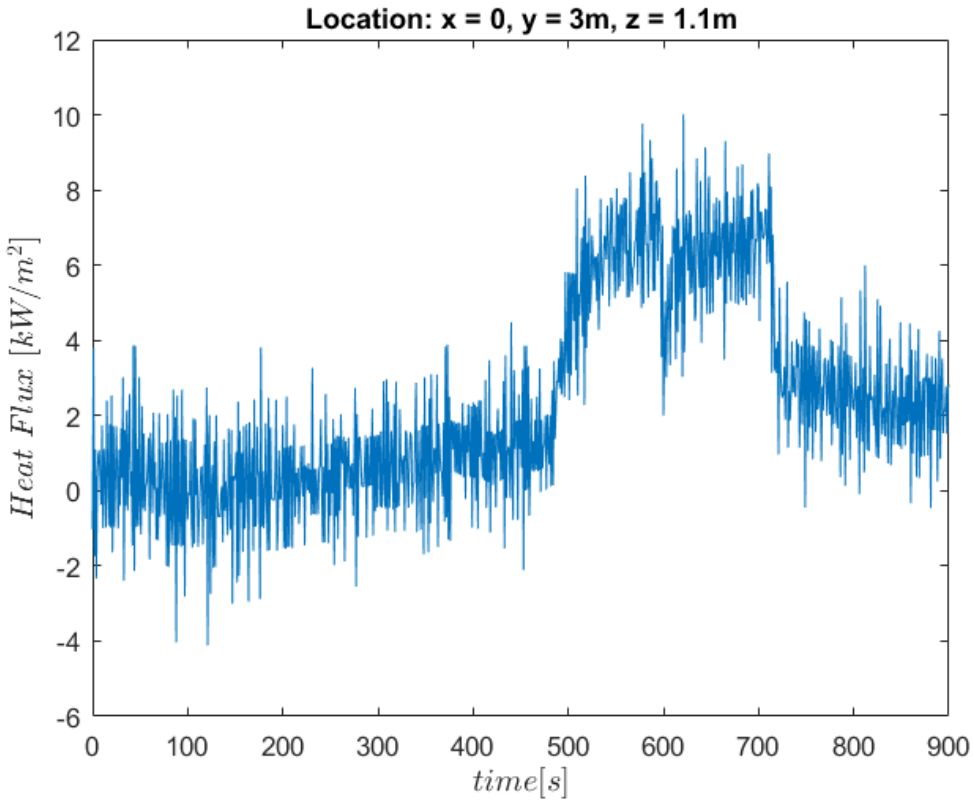

Figure 39- Radiant heat flux changes over time in a TSC located on back wall with two peak heat flux ranges

4.1.3 Experiment 6

As mentioned previously, the only difference between this experiment and experiment 3 is the ventilation mode. This test was done in an under-ventilated condition although the fire never reached a flashover point. Figure 40 shows heat flux evolution in node 12B located on back wall at height of 1.1 m.

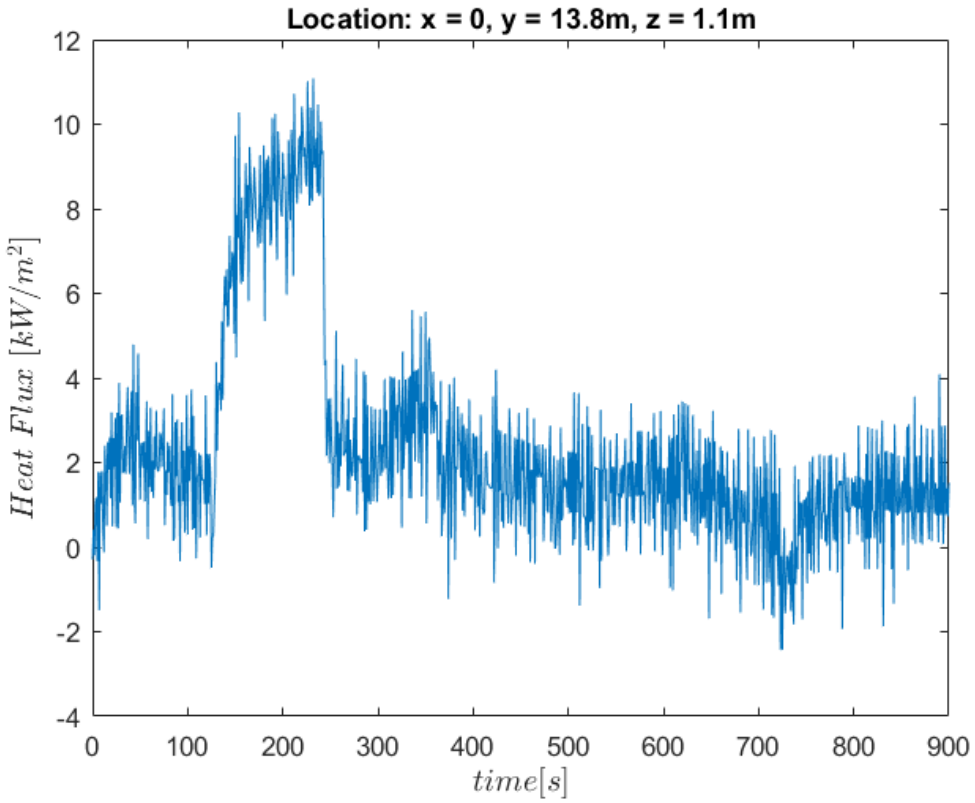

Figure 40- Heat flux pattern in one of the thin skin calorimeters- Experiment 6

Same as other considered experiments, heat flux evolution divides into far and near field categories. Near field duration and time is almost simultaneous with operation of the burners. Near field heat flux value is lower compared to experiment 9 and the reason is the low concentration of hot black smoke inside the compartment. Although the experiment was done in an under-ventilated condition, compartment did not reach flash over point therefore intensity of combustion products was kept low. Graphs with double near field were observed in this experiment as well although not in exact same thin skin calorimeters as previous experiment.

Same as previous experiments, heat flux was maintained in lower values in far field durations.

4.1.4 Experiment 10

Same as previous experiments, incident radiant heat flux evolution was calculated and plotted for all thin skin calorimeters inside the compartment. Figure 41 shows radiant heat flux evolution in node 12B located on back wall. Comparing this graph, along with all other graphs obtained from this experiment's data, shows that same pattern as all other experiments can be observed. Radiant heat flux value is higher in near field areas and decreases to lower values in far field. Same as before, near field duration is almost equal to the duration which the corresponding burners are operating. This graph can be compared with Figure 32 since both have been plotted for data obtained from the same thin skin colorimeter in different experiments. They both have almost same maximum heat flux from fire in near field. Reason would be that both fire and ventilation condition in this experiment is very similar to experiment 9. In addition, fire heat release rate is approximately similar to experiment 9 although it should be mentioned that total duration of this test is considerably shorter.

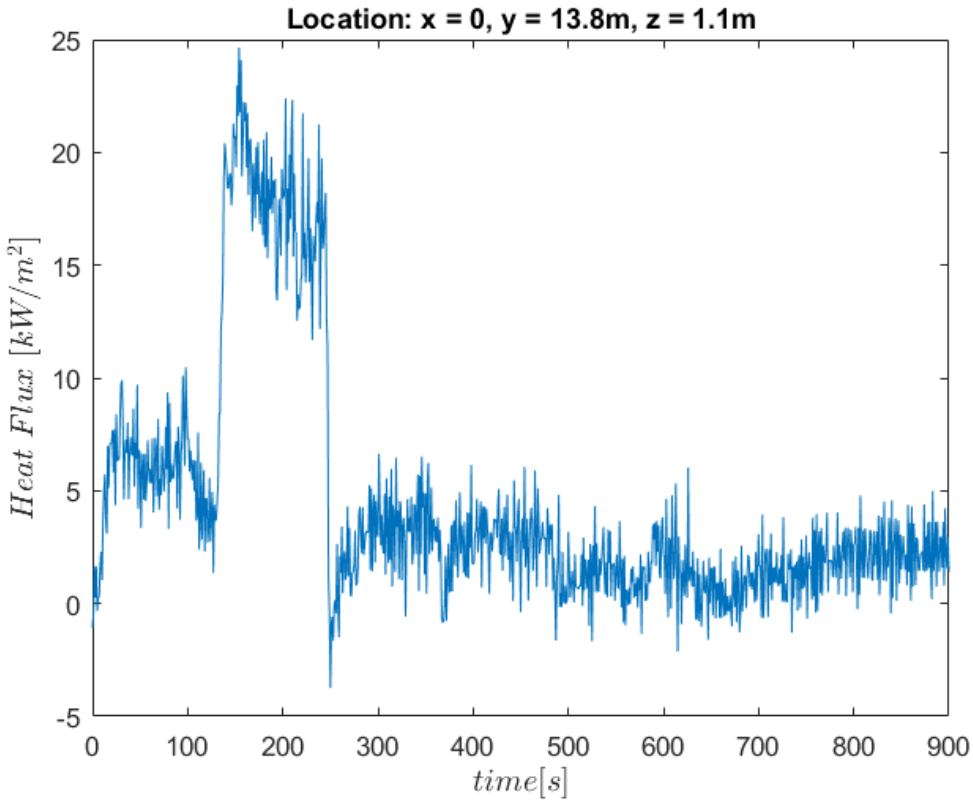

Figure 41- Radiant heat flux changes over time in a TSC located on back wall

In addition to other similarities in heat flux patterns between this experiment and previously considered experiments, some thin skin calorimeters captured near field heat fluxes from multiple burners, therefore double peak was observed. Same as before, near field heat flux values are considerably lower in graphs with two peaks compared to other heat flux graphs.

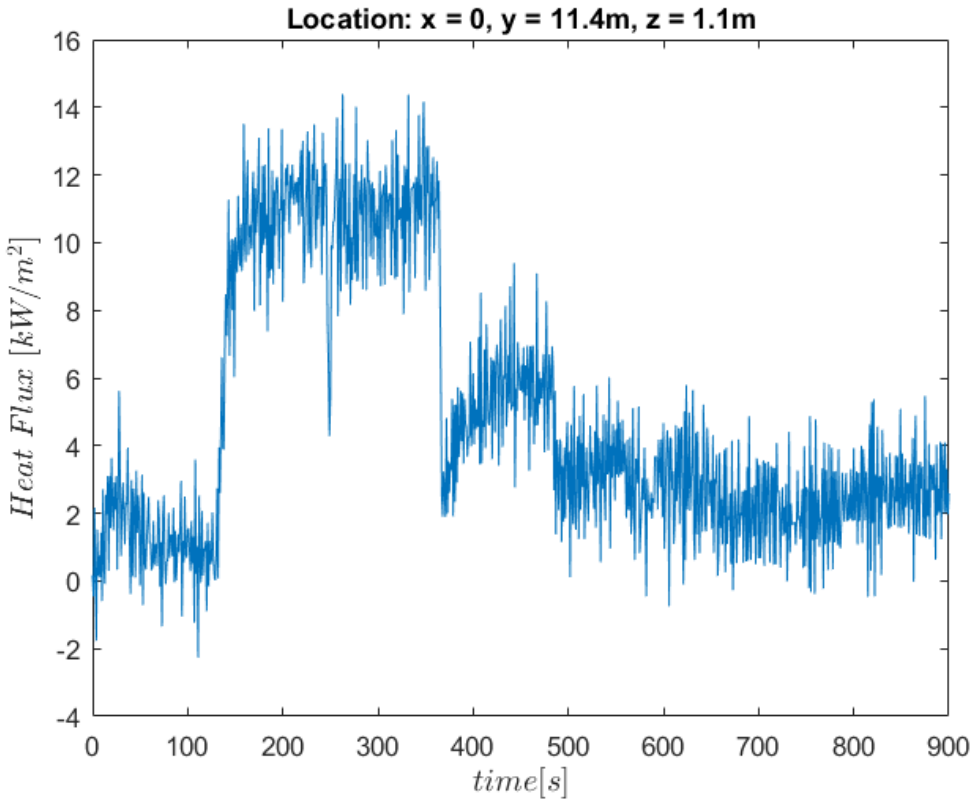

Figure 42- Radiant heat flux evolution in a TSC located on back wall with two peak heat flux durations- Experiment 10

4.2 Incident Radiant Heat Flux in Near Field

In previous chapters it was concluded that heat flux pattern in case of traveling fires can be divided into two different categories of near field and far field. Near field defined as areas close to fire origin and far field defined as areas far from the area involved in the fire. Near field heat flux observed to have a specific pattern in all considered experiments. Heat flux value increased and stayed in a specific maximum value in near field with slight fluctuation. This chapter focuses on near field evolution, its duration and determines if applying a single near field value would be possible for each experiment. All thin skin calorimeters' data in the compartment were studied in details for experiments 3, 6, 9 and 10.

4.2.1 Experiment 3

Near field duration (i.e. duration when heat flux was maximum) was determined for each thin skin calorimeter in back wall located at height of 1.1 m based on the graphs as showed in previous chapter. Near field duration was assumed to be the single (or double) considerable peak(s) in heat flux graphs.

As it was seen in previous chapter, each heat flux evolution graph has a near field period which corresponds to operation of a specific burner. Therefore, each thin skin calorimeter was studied individually to determine time and duration when the heat flux was in maximum value as well as to find the corresponding burner.

Mean heat flux value in near field was calculated for each thin skin calorimeter located at height of 1.1 m in back wall and plotted as shown in Figure 43. Each vertical line in this graph corresponds to location of a pair of burners on the floor (refer to Figure 16 for burners' location details). In other words, black vertical line represents the location of burners 1a and 1b, and with same approach yellow vertical line corresponds to location of burners 6a and 6b.

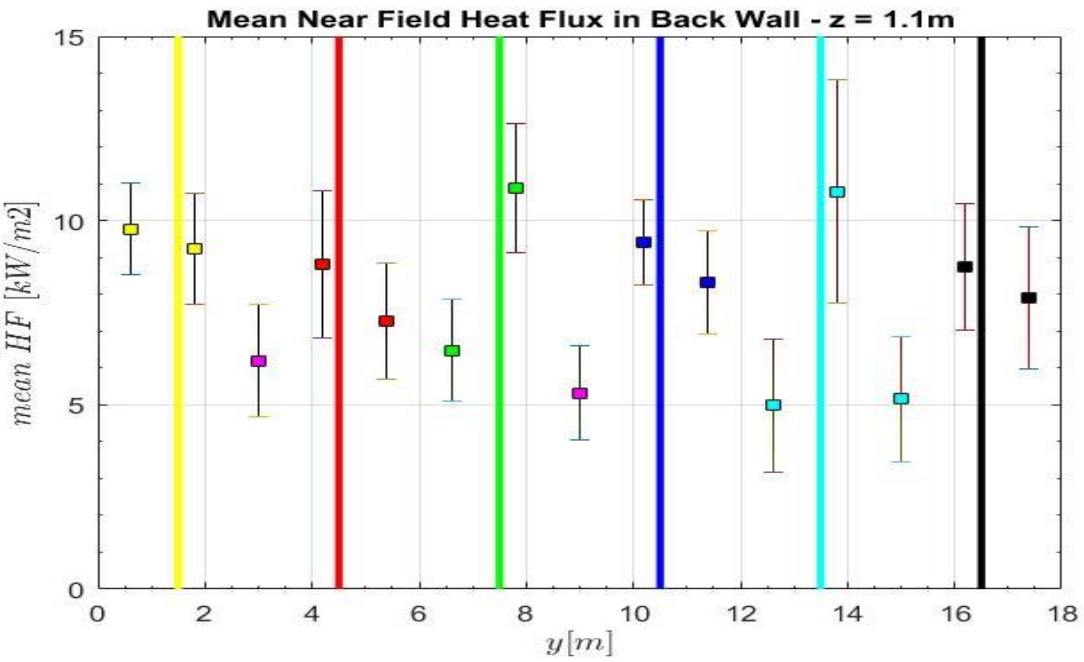

Figure 43- Mean values for near field heat fluxes at height of 1.1m – Each line corresponds to location of a burner set on the floor, square boxes with the same color represent the TSCs which capture the maximum heat flux corresponding to the same burner and pink squares show the mean heat fluxes value for thin skin calorimeters with two peaks- Experiment 3

Thin skin calorimeters which their near field corresponded to the same burner sets were assigned same colors. For instance, thin skin calorimeters located at 16.2, and 17.4 m were both marked with black squares; near field heat flux in these thin skin calorimeters, was captured in the duration when first burner sets were operating. According to Figure 43, couple of squares are marked differently (pink squares). These squares show thin skin calorimeters which captured near field heat flux from burners located at their both sides (i.e. they had two individual peak in their heat flux graph). For instance, radiant heat flux for thin skin calorimeter located at y = 9 m, was in near field during the operation of burners 3a and 3b and afterwards while burners 4a and 4b were ignited.

In addition, standard deviation from the mean heat flux value in near field was calculated for each thin skin calorimeter to establish the variability of the heat flux as the fire moved across a specific thin skin calorimeter location.

According to Figure 43, slight fluctuations from mean near field radiant heat flux value can be observed for each thin skin calorimeter at this specific height, also, the mean values themselves do not considerably vary. Therefore single near field heat flux value can be assumed through length of the compartment at height of 1.1 m.

Although previous figure shows the near field heat flux evolution while fire travels in the space, it lacks time aspect of the burners operation and corresponding near field durations. Duration when fire is in near field of a specific point highly depends on the fire front propagation rate. Parameter dt_{nf} was defined as the duration when heat flux was in near field for a thin skin calorimeter. This time period was determined based on heat flux evolution graphs for each thin skin calorimeter, individually, as the duration when heat flux was in maximum range. Furthermore, duration when each burner pair were operating (dt_{burner}) was determined based on heat release rate graph of fire (refer to Figure 25).

Scaled time for each thin skin calorimeter was then, defined as the ratio of dt_{nf} of the considered thin skin calorimeter to dt_{burner} of the corresponding burner. This ratio shows the relation between the duration when the peak heat flux was measured in a thin skin calorimeter and the duration when corresponding burners were ignited. Figure 44 shows the mean heat flux value in near field for each thin skin calorimeter in the back wall which has a height of 1.1 m, versus the scaled time as defined for each thin skin calorimeter. Colors were kept same as Figure 43.

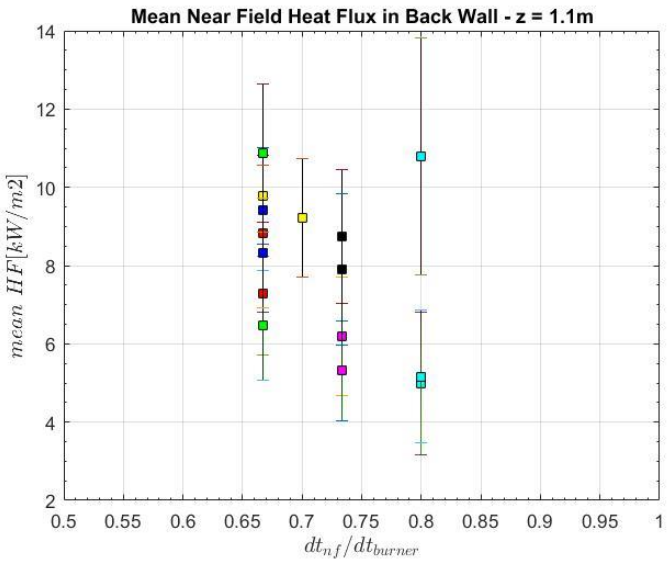

Figure 44- Time scaled mean values for the maximum radiant heat flux range- dt_{nf} is the duration when the radiant heat flux was in maximum range and dt_{burner} is the operating duration of corresponding burner set- Experiment 3

According to Figure 44, variation of the defined time ratio between different thin skin calorimeters is considerably small therefore assuming a single time ratio through the length of the compartment would be reasonable.

Previous calculations indicated that a single near field radiant heat flux value with a specific scaled time can be assumed for thin skin calorimeters at a specific height. In order to achieve a more comprehensive result, same approach was adapted to calculate and analyze the mean radiant heat flux in near field for all other thin skin calorimeters in the compartment.

Thin skin calorimeters on each surface of the compartment were divided into groups based on their location. Back wall, ceiling and floor each divided into 3 groups of 15 thin skin calorimeters (referred to rows “a”, “b”, and “c” in Figure 21 and Figure 22). Side walls each divided into 3 groups of 5 thin skin calorimeters (referred to rows “a”, “b”, and “c” in Figure 23). Same graphs were plotted for all groups to make sure same pattern was obtained in all groups. Mean value of radiant heat flux in near field was

then calculated for each group and plotted as shown in Figure 45. Each graph has 3 different points and each point is representative of a previously mentioned thin skin calorimeter group. Same as before, standard deviation for both time and heat flux was calculated for each group and is shown in the figure.

It can be observed from Figure 45 that for in this specific experiment which was an over-ventilated traveling fire, small near field heat flux values was obtained. In addition, heat flux and time fluctuations can be assumed negligible for each group.

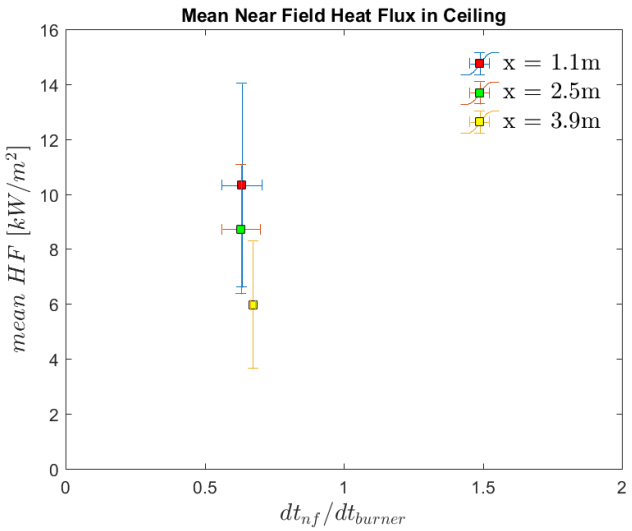

(a)

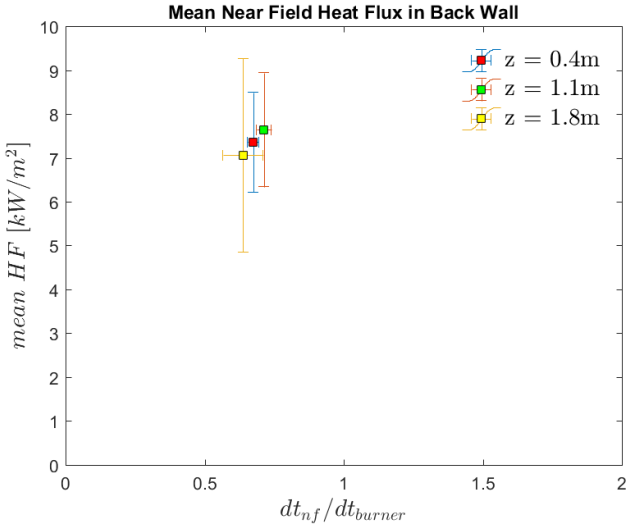

(b)

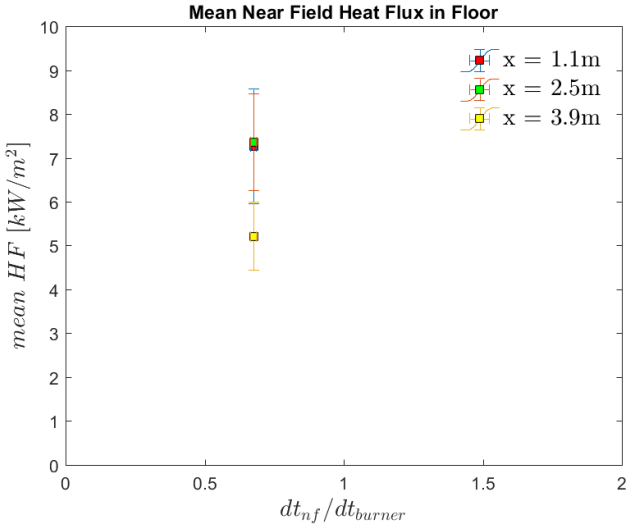

(c)

Figure 45- Mean radiant heat flux in near field in all surfaces of the compartment- dt_{nf} represents the near field duration, and dt_{burner} represents the duration when the corresponding burner was operating – Experiment 3

4.2.2 Experiment 6

Same as previous experiment, mean heat flux value in near field was first calculated for each thin skin calorimeter located at height of 1.1 m in back wall and plotted as shown in Figure 46. A detailed description of elements used in graphs of this section has been provided in "Experiment 3" of this chapter.

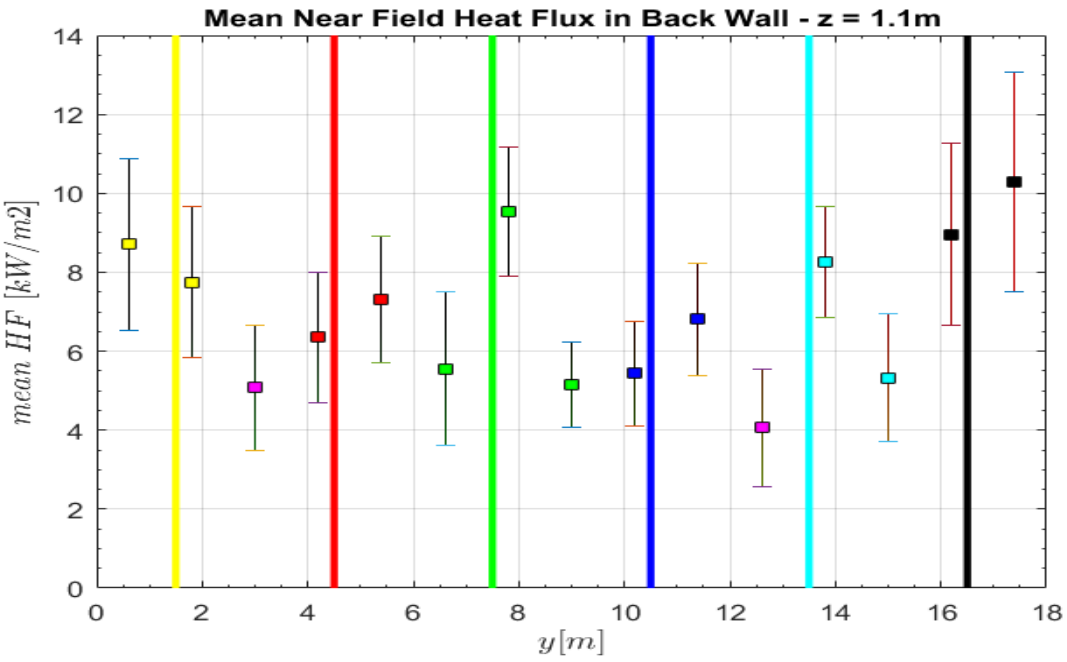

Figure 46- Mean values for near field heat fluxes at height of 1.1m – Each line corresponds to location of a burner set on the floor, and square boxes with the same color represent the TSCs which capture the maximum heat flux corresponding to the same burner and pink squares show the mean heat fluxes value for thin skin calorimeters with two peaks - Experiment 6

Couple of thin skin calorimeters had double near field heat fluxes although they were not exact same thin skin calorimeters as previous experiment.

In addition, same time scale was defined for this experiment and heat fluxes were plotted as shown in Figure 47. According to this graph, variation of the time ratio is considerably small.

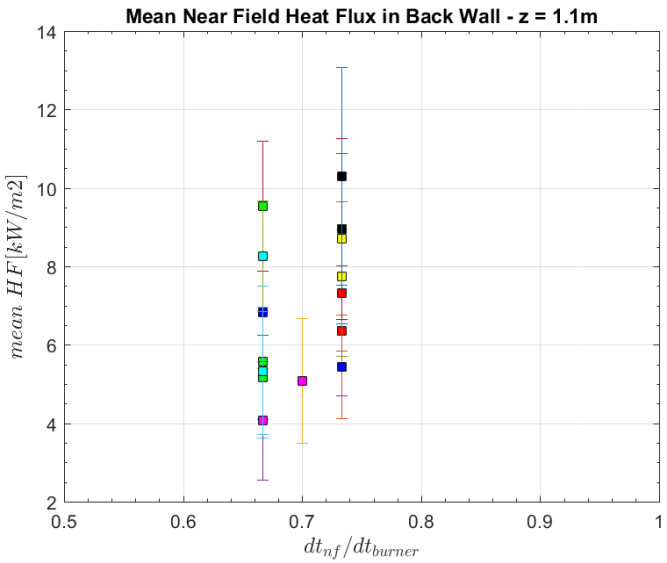

Figure 47- Time scaled mean values for the maximum radiant heat flux range- dt_{nf} is the duration when the radiant heat flux was in maximum range and dt_{burner} is the operating duration of corresponding burner set- Experiment 6

After all, near field radiative heat flux duration for all thin skin calorimeters in ceiling, back wall and floor was determined and the mean value was calculated (based on the same approach as previous experiments). Figure 48 shows the mean value for each group in mentioned surfaces in addition to their averaged time ratio. Heat flux fluctuation in thin skin calorimeters located on the ceiling and upper heights of the back wall seems to be more than other parts. Possible reason would be the circulation of the hot gases close to ceiling. All shutters were remained closed during this experiment which might have caused the high scattered data in these areas.

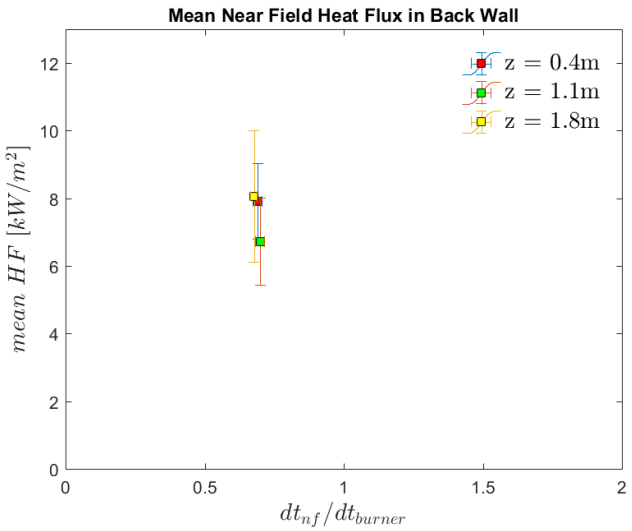

(a)

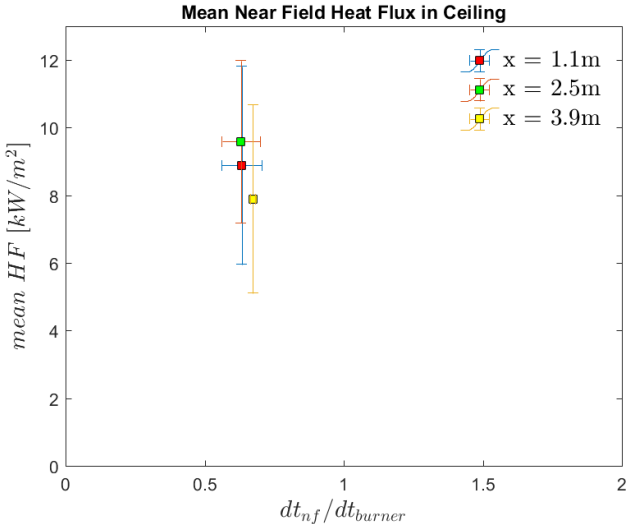

(b)

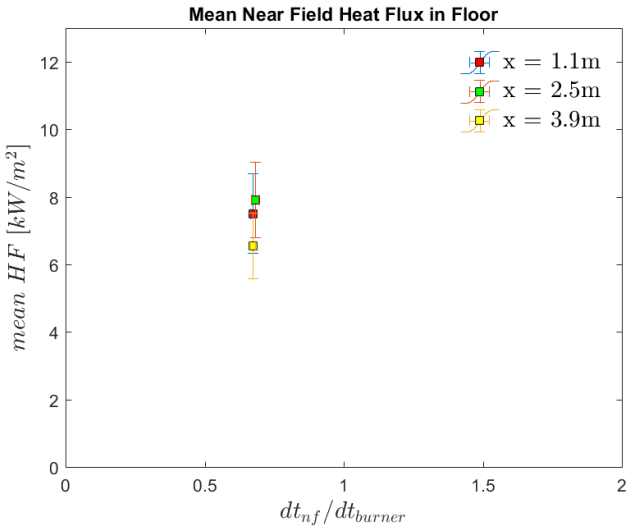

(c)

Figure 48- Mean radiant heat flux in near field in all surfaces of the compartment- dt_{nf} represents the near field duration, and dt_{burner} represents the duration when the corresponding burner was operating – Experiment 6

4.2.3 Experiment 9

Same as previous experiments, mean heat flux value in near field was first calculated for each thin skin calorimeter located at height of 1.1 m in back wall and plotted as shown in Figure 49. A detailed description of elements used in graphs of this section has been provided in "Experiment 3" of this chapter.

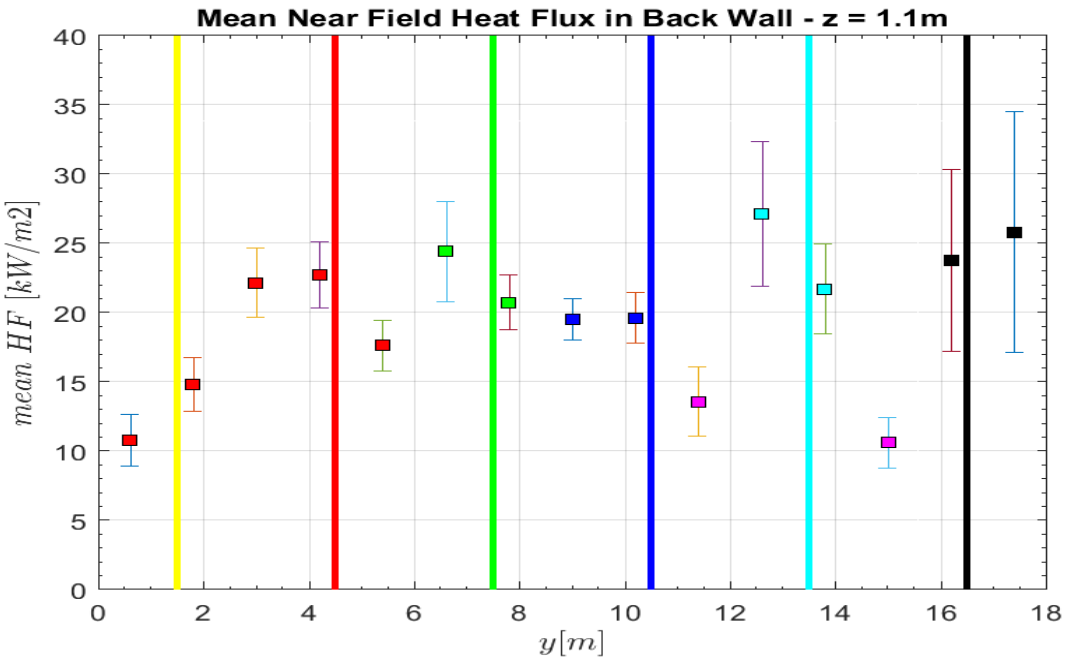

Figure 49- Mean values for near field heat fluxes at height of 1.1m – Each line corresponds to location of a burner set on the floor, and square boxes with the same color represent the TSCs which capture the maximum heat flux corresponding to the same burner and pink squares show the mean heat fluxes value for thin skin calorimeters with two peaks - Experiment 9

Two thin skin calorimeters at this height had a double peak heat flux although not in the same location as previous experiments. All other heat flux data, followed the normal near field pattern. In addition, the overall near field heat flux values in this experiment seems to be higher than previous tests. Probable reason would be the ventilation condition of this experiment. As mentioned previously, this experiment started in an under-ventilated condition, and shutters were removed systematically during the test.

According to Figure 49, at earlier stages of the fire (i.e. black squares), the spatial variability is limited but the proximity of the wall results in large fluctuations, thus a large standard deviation. This potentially might have been caused by the considerable scatter in temperature measurements at this locations. Possible reason for high scattered data in the beginning of the experiment would be that operation duration of burners 1a and 1b which resulted in near field heat flux in these thin skin calorimeters was short (almost 60 seconds) therefore there was not enough time for both gas and solid phase temperatures to stabilize inside the compartment. As fire traveled, and after a slight increase in overall temperature, compartment reached a more steady condition; temperature fluctuations decreased and therefore a lower variation range has been achieved.

Time scaled graph was also plotted at height of 1.1 m for back wall to achieve an overview for this aspect of the experiment.

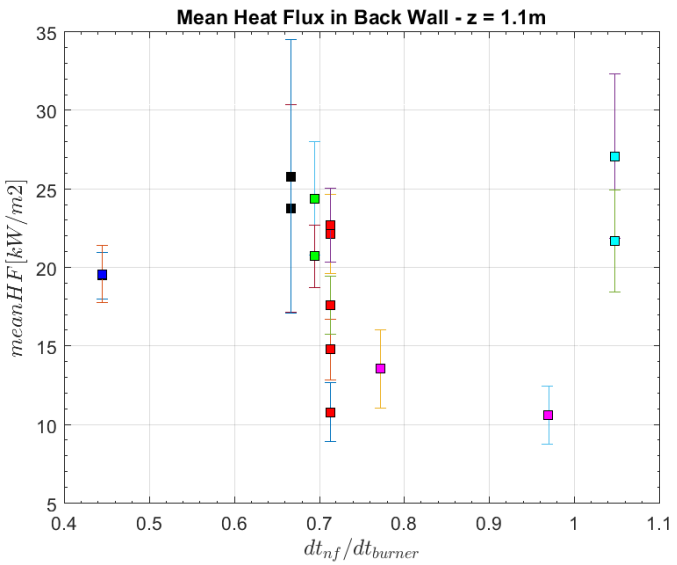

Figure 50- Time scaled mean values for the maximum radiant heat flux range- dt_{nf} is the duration when the radiant heat flux was in maximum range and dt_{burner} is the operating duration of corresponding burner set- Experiment 9

After all, mean value of heat flux in near field for thin skin calorimeters, in addition to corresponding standard deviations (both from time, and heat flux perspective) were calculated and summarized in Table 11.

Table 11- Mean heat flux value for peak duration- Back wall- z = 1.1 m

Mean Heat Flux Value at height of 1.1m in back wall [kW/m^2]	**Error Range**	
	Non-dimensional Time	Heat Flux
18.5	0.2	5.6

Previous table and related calculations elaborates the reason assuming a single heat flux value in the near field throughout the length of the compartment in height of 1.1 m while considering range of variability would be reasonable.

Same as previous experiments, in order to achieve a comprehensive result, mean radiant heat flux in near field for all other thin skin calorimeters in the compartment was calculated.

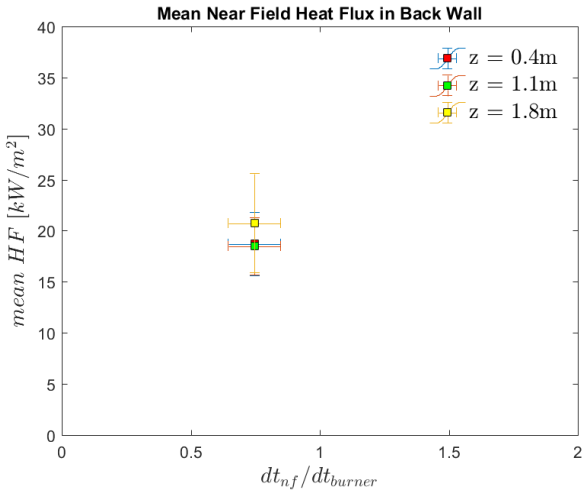

(a)

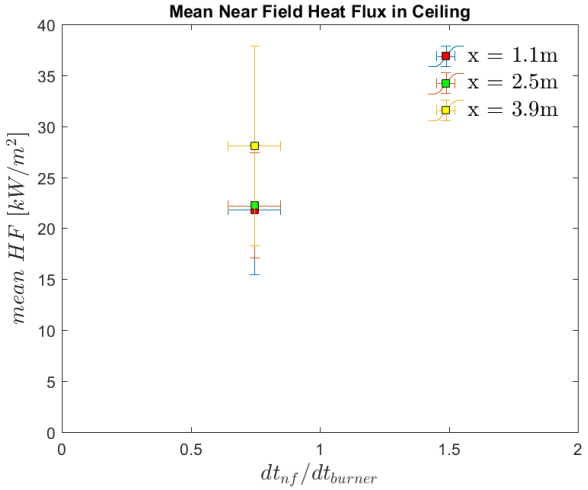

(b)

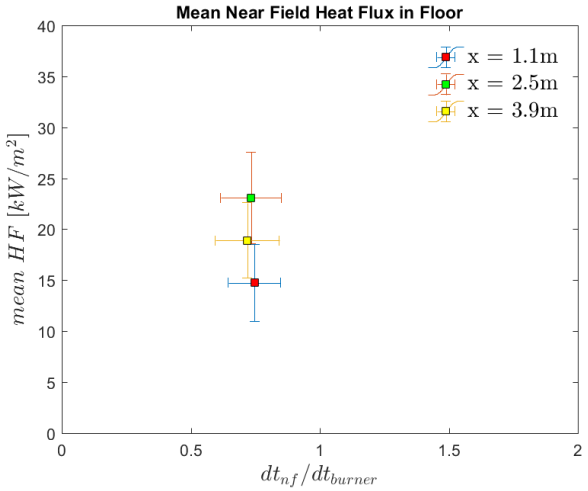

(c)

Figure 51- Mean radiant heat flux in near field in all surfaces of the compartment- dt_{nf} represents the duration when the heat flux was in maximum value, and dt_{burner} represents the duration when the corresponding burner was operating

No significant variation in the scaled time values was observed between different groups and surfaces. Each horizontal standard deviation in the graph is a representation of variation in the scaled time between thin skin calorimeters of a certain group. According to Figure 51 horizontal bars are small in back wall, ceiling and floor, and almost zero in side walls.

Reason was that side wall thin skin calorimeter data sets were observed to have the same dt_{nf}; besides, dt_{nf} for all thin skin calorimeters in right wall happened while burners 1a and 1b were operating. This resulted in the same scaled time ratio for all thin skin calorimeters in a group. Same reason applies to left wall with the exception that dt_{nf} in the left wall was corresponding to burners 5a and 5b.

In addition, heat flux values in the left wall seems to be significantly lower than other surfaces in the compartment. Probable reason would be that last stage of 1 MW fire ended in burner pairs 5 with a distance of 4.5 m from the left wall (refer to Figure 16 for detailed burners' location), besides burner 6a only operated to keep the lower 0.5 MW heat release rate of the fire in the last stages of the experiment; therefore, left wall, compared to other surfaces, never reached high temperatures.

4.2.4 Experiment 10

Same as previous experiments, mean heat flux value in near field was first calculated for each thin skin calorimeter located at height of 1.1 m in back wall and plotted as shown in Figure 49. A detailed description of elements used in graphs of this section has been provided in "Experiment 3" of this chapter.

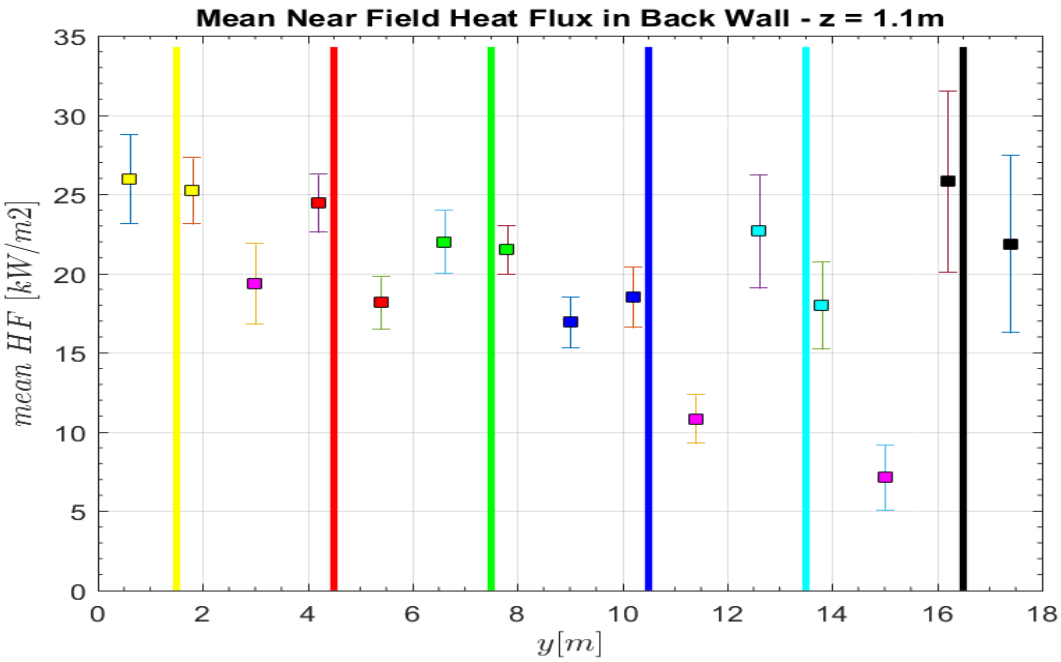

Figure 52- Mean values for near field heat fluxes – Each blue line corresponds to location of a burner set on the floor, and square boxes with the same color represent the TSCs which capture the maximum heat flux corresponding to the same burner and pink squares show the mean heat fluxes value for thin skin calorimeters with two peaks- Experiment 10

Both conditions and outcomes from this experiment were close to experiment 9 therefore it will not be discussed further for other thin skin calorimeters.

4.2.5 Overall mean radiant heat flux in near field

As a final step in studying mean near field heat flux values, data from previously considered experiments were plotted in a single graph for each surface. Figure 53 shows the mean radiant heat flux in near field for each surface. In this figure, data from experiment 3 is marked as square, experiment 6 is marked as circle and experiment 9 is marked as diamond on each surface. Each point in Figure 53 shows the mean heat flux value and corresponding error bars at a certain non-dimensional height/depth. In order to obtain the non-dimensional locations, height and depth of each thin skin calorimeter group was divided by the overall dimension of the considered surface. Non-dimensional lengths makes it easier to apply the near field heat flux values compartments with other dimensions.

In addition, an overall mean value was calculated for the entire compartment in different experiments. This average value was calculated based on the near field data from 135 thin skin calorimeters located on back wall, ceiling and floor surfaces of the compartment (does not include data from thin skin calorimeters located on side walls). Table 12 shows the mentioned value for different experiments.

Table 12- Near field radiant heat flux in floor, back wall, and ceiling for different traveling fire experiemnts

					Variations
Experiment	Ventilation Mode	Fire Mode	Near Field Heat Flux	Non-dimensional Time	Heat Flux
Experiment 3	Over-ventilated	Traveling	7.4	0.7	1.4
Experiment 6	Under-ventilated	Traveling	7.9	0.6	0.9
Experiment 9	Transient	Traveling	20.7	0.7	3.7

Experiment 10 was not considered in this calculation since both fire and ventilation condition and as a result, near field heat flux values were close to those from experiment 9. This can also be concluded from comparing Figure 49 and Figure 52.

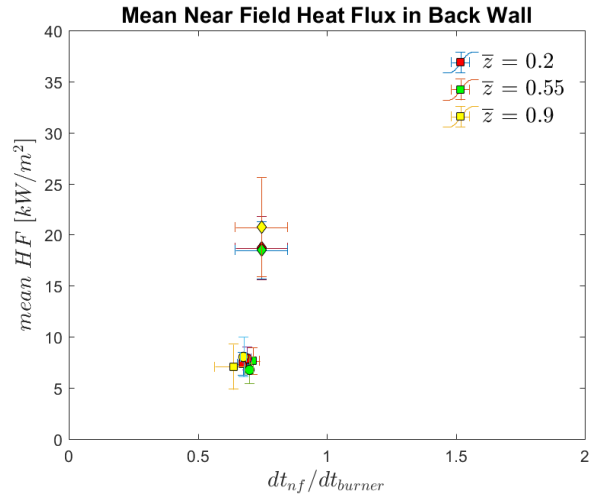

(a)

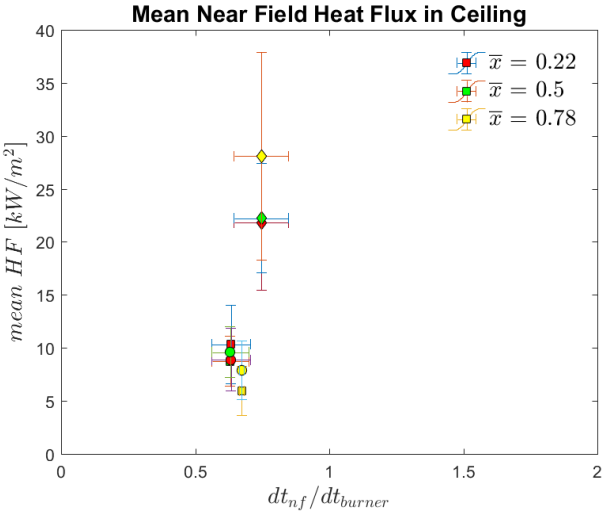

(b)

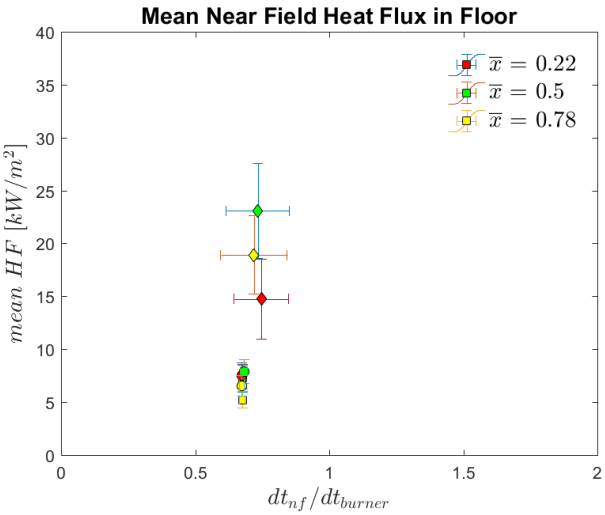

(c)

Figure 53- Mean near field radiant heat flux for all experiments on each surface- data from experiment 3 is marked as square, experiment 6 is marked as circle and experiment 9 is marked as diamond on each surface

4.3 Incident Radiant Heat Flux in Far Field

As mentioned in previous chapters, far field incident radiant heat flux, has considerably lower value compared to near field heat fluxes. This chapter studies the incident radiant heat flux in far field and provides the average heat flux value for different fire and ventilation conditions.

Experiment 3 and 9 were the considered tests for far field heat flux analyses. Experiments 6 and 10 provided results which were close to experiments 3 and 9, respectively therefore far field heat flux was not studied for these tests.

Far field heat flux durations were found for each thin skin calorimeter and each burner, based on obtained data. This duration was defined as the time when a burner is ignited inside the compartment although the burner is not close enough to the considered thin skin calorimeter to produce the maximum possible heat flux.

4.3.1 Experiment 3

Fire was maintained at the constant heat release rate of 1 MW throughout the experiment while traveling from right side of the compartment to the left by means of burners. As a result, incident radiant heat flux in a specific thin skin calorimeter maintained a specific (i.e. far field) value during the experiment except for the durations which the operating burner was close enough to the considered point to make a near field heat flux pattern.

Figure 54 shows the heat flux pattern in a thin skin calorimeter in back wall at node 4B, located at left side of the compartment between burners 5 and 6. Near field duration

in this thin skin calorimeter was captured when burners 5a and 5b were operating. All other durations can be assumed as far field.

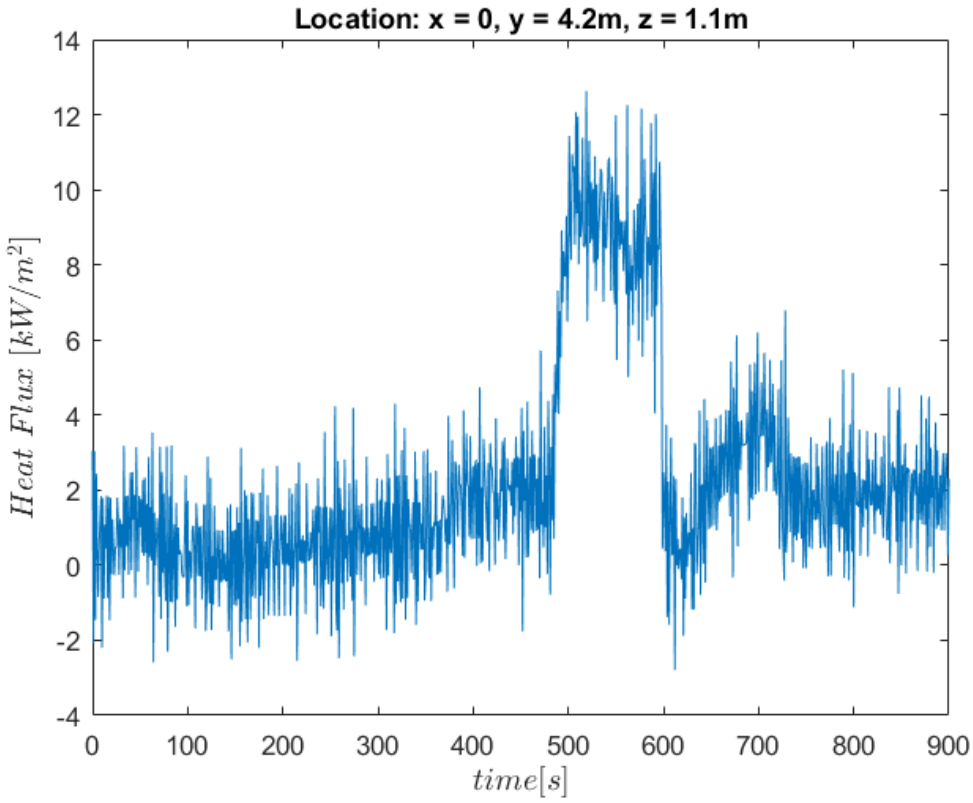

Figure 54- Incident radiant heat flux in thin skin calorimeter at node 4B located on back wall at height of 1.1m

According to this figure, far field heat flux was captured to be negative in some time steps. This pattern was observed in almost all other heat flux graphs. Since gas and solid phase temperatures are key components affecting heat flux, these temperatures were studied individually. Figure 55(a) shows solid phase temperature obtained from thin skin calorimeter in the same location (node 4B on back wall) and Figure 55(b) presents gas phase temperature in thermocouple adjacent to mentioned thin skin calorimeter.

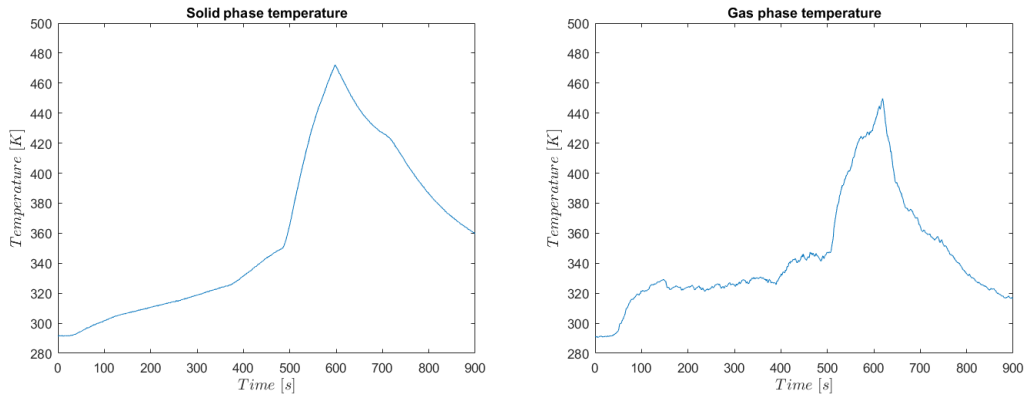

(a) (b)

Figure 55- Temperature in (a) thin skin calorimeter located at node 4B in back wall, (b) thermocouple adjacent to mentioned thin skin calorimeter

As mentioned previously in equation 4, solid phase temperature as well as the difference between solid and gas phase temperatures are main parameters for calculating the radiative heat flux. According to Figure 55, in far field areas, not only the solid phase temperature is small, but also the temperature difference oscillates which results in the pattern which was observed in Figure 54.

Far field duration for each thin skin calorimeter was established individually based on their heat flux pattern. Mean far field heat flux value was calculated considering the mentioned duration. Average value was calculated with same approach as near field calculations. Thin skin calorimeters were divided into different groups, each include 15 thin skin calorimeters. Each surface (Ceiling, back wall and floor) was divided into 3 groups which resulted in 3 mean far field heat flux values. Average heat fluxes in addition to their error bars were studied in detail to make sure similar pattern was obtained for all surfaces.

As a result, average far field radiant heat flux resulted to be -0.4, 1.2, and 2.4 kW/m^2 in ceiling, back wall and floor, respectively. Since the negative heat flux value is not reasonable and as mentioned the possible reason is the fluctuation in the measured

parameters, average heat flux of zero was assumed for ceiling. These results show that assuming a single far field heat flux value through entire compartment, on mentioned surfaces, for this experiment would be reasonable. Therefore, far field heat flux value of 1.2 kW/m^2 can be assumed for fire and ventilation condition mentioned in this experiment.

4.3.2 Experiment 9

Same as previous experiment, 1 MW fire started in right side of the compartment and moved to the left although heat release rate of the fire was reduced to 0.5 MW in specific durations. Far field period for a thin skin calorimeter was defined based on the duration when the burners located at the far field were operating.

Same approach was chose to find the duration of far field heat flux in this experiment. Far field duration for each thin skin calorimeter was defined as the sum of operation duration of burners located at far field. In other words, duration when the radiant heat flux was not in maximum value.

Far field heat fluxes were studied for each thin skin calorimeter, individually, and mean value was calculated for far field duration and assumed to be average of total far field incident radiant heat fluxes.

Finally, average far field heat flux value resulted to be 3.2, 5.1, and 6.8 kW/m^2 for ceiling, back wall and floor, respectively and overall mean value for the compartment in this specific fire and ventilation condition can be assumed as 5 kW/m^2.

4.4 Convective Heat Flux

Convective heat flux inside the compartment was calculated using data from thin skin calorimeters, their adjacent thermocouples, and velocity probes in each opening. Experiment 9 was chosen to be the basis for convective heat flux calculations. Voltage from the velocity probes were treated and converted into velocity as described in chapter 3.

Figure 56 presents an instance of velocity evolution in opening 14 located at right side of the compartment.

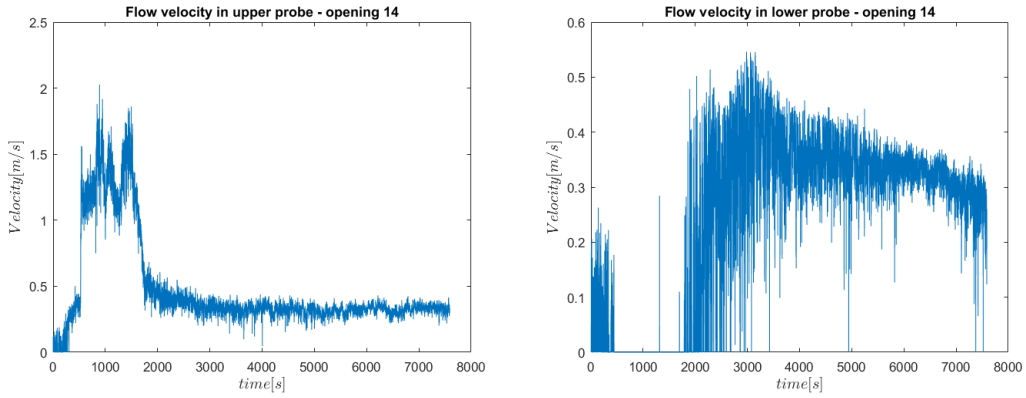

Figure 56- Velocity flow in the probes located in opening 14

Same graphs were plotted for both upper and lower probes in all 15 opening to find the maximum inflow and outflow velocity through openings. Based on the calculations, maximum outflow and inflow velocity for this experiment approximated as 1.5 m/s, and 0.35 m/s, respectively.

As mentioned previously, linear velocity profile was assumed in height of the compartment. Figure 57 shows this linear profile according to calculated velocities for upper and lower probes.

Neutral plane height defined to be the height in the compartment where the velocity reaches zero value. Heights of the probes were designed in a way to make sure that the upper probe captured hot outflow gas velocity, and lower probe captured ambient inflow air to the compartment, therefore, the neutral plane locates between the probes.

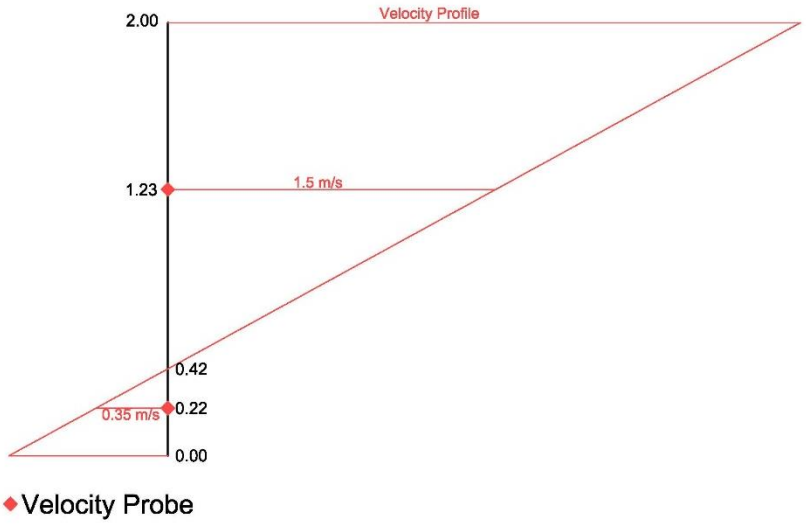

Figure 57- Velocity profile over the height of the compartment. Black vertical line indicates the compartment height and the values indicated in this line are in meters- Red lines indicate the velocity profile in different heights

Assuming mentioned velocities, neutral plane resulted to be at the height of 0.42 m from the floor. Heat transfer coefficient value at neutral plane height was adapted as the basis for convective heat flux calculations.

Furthermore, as a conservative approach maximum velocity in upper probe was applied to calculate Reynolds and therefore Nusselt number to achieve convective heat transfer coefficient. Figure 58 represents evolution of heat transfer coefficient as a function of characteristic length scale. This value decreases with increase in length. It is impossible to define a proper characteristic length scale for this compartment, thus a conservative average value for the length scale will be used. Considering Figure 58 along with neutral plane height result (based on Figure 57), the characteristic length scale was

defined as the neutral plane height. By using this value a typical convective heat transfer coefficient could be approximated as $4\ [\mathrm{W}/m^2.K]$. It is clear that in some areas the heat transfer coefficient will be larger, but in others it will be lower, so this average value was deemed to be representative of the ensemble.

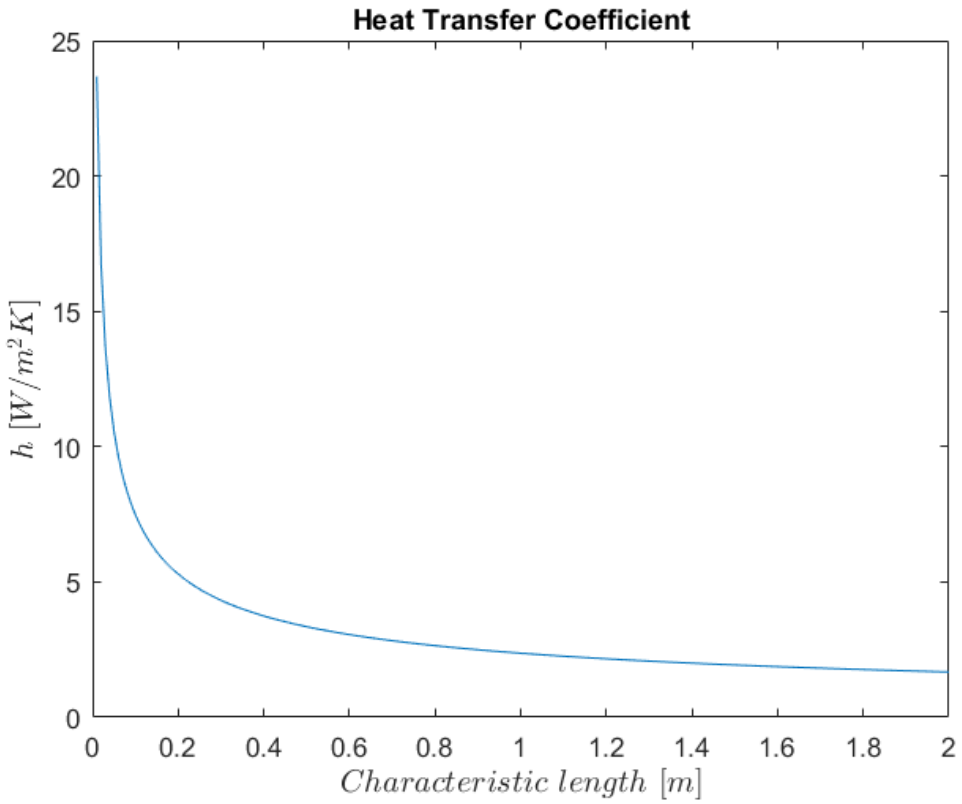

Figure 58- Change of convective heat transfer coefficient over height of the compartment

After calculating convective heat transfer coefficient every required parameters for calculating convection was obtained. Temperature differences between the solid and gas phase were calculated for each thin skin calorimeter and adjacent thermocouple at each time step. Figure 59 shows the convective heat transfer evolution through time in node 12B located on back wall (refer to Figure 21 for location details). Convective heat flux fluctuates during the entire experiment time and is not limited to near field. For

instance, Figure 59 is one of the nodes close to burners 2a and 2b although the fluctuations are almost at the same magnitude while other burners are operating.

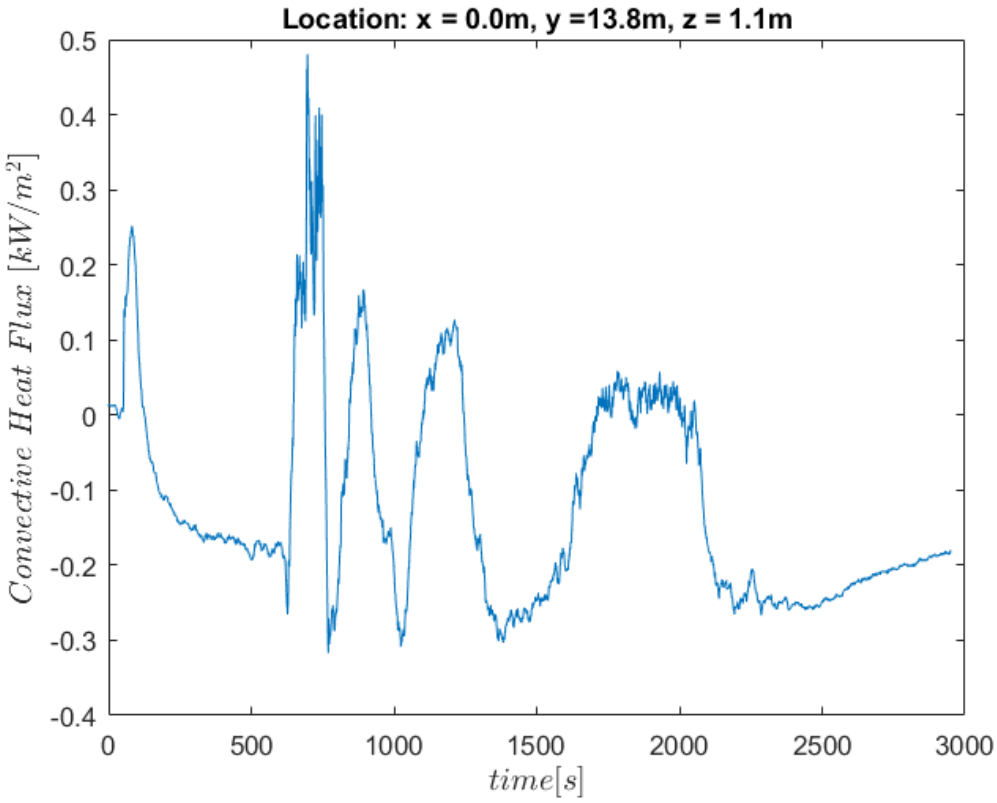

Figure 59- Convective heat flux in back wall- node 12B (refer to Figure 21 for location details)

Possible reason for fluctuations in convection would be that gas phase temperature variations are dramatic as a slight change occurs in heat release rate of the fire. In order to analyze the convection fluctuations in detail, both gas phase and solid phase temperature were studied separately. Figure 60 and Figure 61 represent the evolution of these temperatures for the thin skin calorimeter located in node 12B and its adjacent thermocouple. Temperatures were averaged in 30, and 90 seconds time intervals to achieve a clear overview of the changes with less data noise.

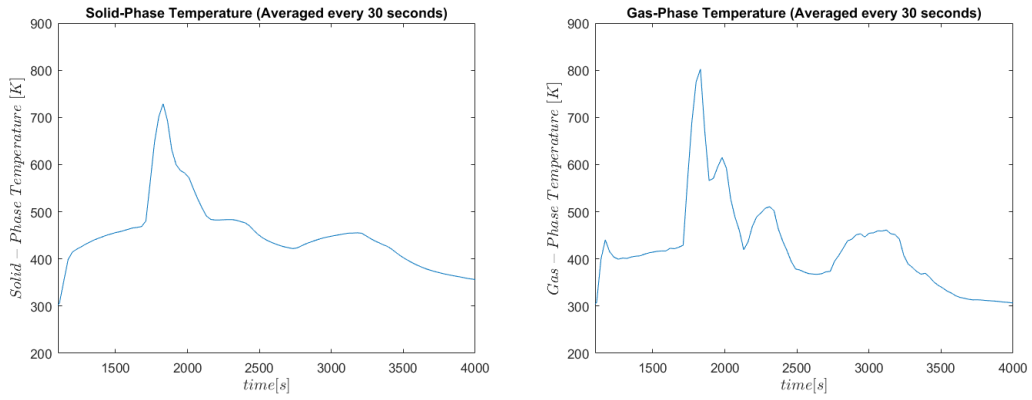

Figure 60- Temperature averaged in 30 seconds time intervals

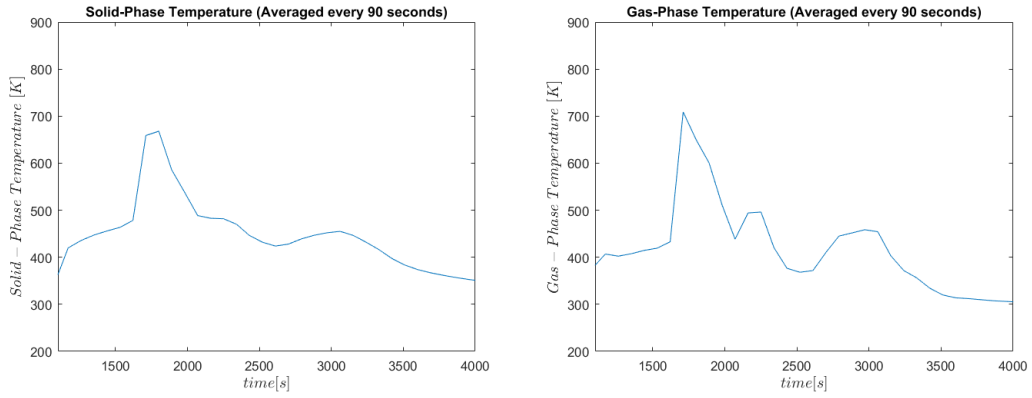

Figure 61- Temperature averaged in 90 seconds time intervals

According to previous graphs, solid phase temperature reaches a peak when the fire is in near field. In all other stages of the fire, temperature has a lower value. In contrast, gas phase temperature has fluctuations in all stages of the experiment. Therefore, by comparing the solid and gas phase temperature graphs, it can be concluded that the convective heat flux pattern is mostly driven by gas phase temperature variations.

As expected, based on Figure 59 values of convective heat fluxes (i.e. convective losses) are clearly negligible compared to radiative heat flux, therefore total heat flux imposed to the surfaces of the compartment can be approximated solely by considering the radiation heat transfer.

It would be worth mentioning that the heat transfer coefficient which was calculated and used for convection heat transfer purposes was different than the one used in incident radiant heat flux calculations in previous chapters although as the convection heat transfer resulted to be considerably small, value was kept for incident radiant heat flux calculations.

In addition, since the convective heat flux values are very small, compared to incident radiant heat fluxes, it was concluded that the net heat flux in considered types of fire can solely be calculated through radiation.

Chapter 5: Conclusions

Heat transfer inside an open compartment, highly depends on the fire condition in addition to the way which cold air and hot gasses circulate. Different modes of ventilation condition can affect the heat transfer inside the compartment.

Based on the results, in the near field, convective heat transfer in open compartments is considerably smaller than incident radiant heat fluxes imposed to surfaces of the compartment by the fire. Therefore, net heat flux can be calculated solely through radiation. This is also potentially the case for the far field, nevertheless, it needs to be verified as a function of the distance from the fire.

In addition, heat flux analyses on different surfaces of a specific compartment fire shows that a single heat flux value can be assumed for a specific fire and ventilation condition since heat flux variation in different surfaces and time steps were negligible. In the case of traveling fires, where the heat flux has different behavior in near field and far field, specific heat flux values can be assigned to each mentioned period.

Table 13 shows the near field heat flux values for various fire and ventilation conditions. The non-dimensional time is scaled by the residence time of the fire at each given location.

Table 13- Near field heat flux values and time ratio for different ventilation and fire conditions

Ventilation Mode	Fire Mode	Near Field Heat Flux	Non-dimensional Time
Over-ventilated	Traveling	7.4	0.7
Under-ventilated	Traveling	7.9	0.6
Transient	Traveling	20.7	0.7

Also, based on structural analyses for different materials, in cases where the Biot number is small (generally less than 0.1), some simplifications are acceptable and lumped capacitance method is valid. Errors which are associated with using the lumped capacitance method are negligible, and therefore in these cases the temperature of the solid can be assumed to be spatially uniform. Resolving the time evolution of the fire is less important and a time integral of the heat flux will accurately deliver the evolution of the temperature as a function of time for the structure.

For materials with high thermal conductivities, such as steel, in real fire conditions lumped capacitance can be applied under conditions where the considered dimension is smaller than the corresponding characteristic length. As the dimensions of material increases, temperature difference between surfaces becomes greater which results in considerable error, and lumped capacitance method will no longer be applicable. In these cases an integrated approach to the delivery of energy to the structure will not be adequate because it will fail to reproduce the temperature gradients. The time evolution of the fire is therefore important.

In contrast, materials such as concrete with so many uncertainties regarding their thermal properties, require heat transfer analysis for all dimensions and fire conditions. Heat transfer within materials with very low thermal conductivities such as insulation will not be as fast as aforementioned mediums, therefore one dimensional convection

heat transfer analysis shall be done. Table 14 shows the summary of discussion considering different materials. For conctere, the time evolution of the fire is of importance.

Table 14- Overview of applicable heat transfer methods for different materials

Material	Condition	Description
Steel	for $y < L_c$	Lumped capacitance will be applicable
	for $y > L_c$	One dimensional conduction heat transfer analysis shall be done
Concrete	In all cases	One dimensional conduction heat transfer analysis shall be done
Insulation Low Density (Sprays)	for $t < t_c$	$T_s = T_g$
	for $t > t_c$	One dimensional conduction heat transfer analysis shall be done
Insulation Standard Density (Boards)	In all cases	One dimensional conduction heat transfer analysis shall be done

Bibliography

[1] S. H. Ingberg, "Tests of the Severity of Building Fires," 1928.

[2] "ASTM E119- Standard Test Methods for Fire Tests of Building Construction and Materials".

[3] "ISO 834-11: Fire resistance tests -- Elements of building construction".

[4] "BS 476- Fire tests on building materials and structures".

[5] M. Law, "A Relationship Between Fire Grading and Building Design and Contents," *Fire Research Note, No 877,* 1971.

[6] K. Kawagoe, "Fire Behavior in Rooms," *Building Research Institute, No 27,* 1958.

[7] P. H. Thomas, A. J. Heselden and M. Law, "Fully developed compartment fires-two kinds of behaviour," *Fire Research Technical Paper No.18,* 1967.

[8] H. Simms, D. Hird and H. G. H. Wraight, "The Temperature and Duration of Fires," *Fire Research Note, No 412,* 1960.

[9] P. H. Thomas, "Studies of Fires in Buildings Using Models - Part I, Experiments in Ignition and Fires in Rooms," 1960.

[10] J. L. Torero, A. H. Majdalani, C. Abecassis-Empis and A. Cowlard, "Revisiting the Compartment Fire," *Fire Safety Science 11: 28-45.*

[11] B. R. Kirby, D. E. Wainman, L. N. Tomlinson, T. R. Kay and B. N. Peacock, "Natural Fires in Large Scale Compartments," *International Journal on Engineering Performance-Based Fire Codes,* 1999.

[12] C. Abecassis-Empis, P. Reszka, T. Steinhaus, A. Cowlard, H. Biteau, S. Welch, G. Rein and J. L. Torero, "Characterisation of Dalmarnock Fire Test One," *Experimental Thermal and Fluid Science,* pp. 1334-1343, 2008.

[13] G. Rein and C. Abecassis-Empis, "The Dalmarnock Fire Tests: Experiments and Modelling," 2007.

[14] A. Cowlard, A. Bittern, C. Abecassis-Empis and J. L. Torero, "Some Considerations for the Fire Safe Design of Tall Buildings," *International Journal of High-Rise Buildings.*

[15] F. P. Incropera, D. P. Dewitt, T. L. Bergman and A. S. Lavine, Principles of heat and mass transfer, Wiley.

[16] J. e. a. Torero, "Defining the thermal boundary condition for protective structures in fire," *Engineering Structures,* 2016.

[17] Usmani, "Fundamental principles of structural behaviour under thermal effects," *Fire Safety Journal,* 2001.

[18] J. P. e. a. Hidalgo, "An experimental study of full-scale open floor plan enclosure fires," *Fire Safety Journal,* pp. 22-40, 2017.

[19] J. Stern-Gottfried, "Travelling fires for structural design," 2011.

[20] J. P. Hidalgo, "A Thin Skin Calorimeter (TSC) for quantifying irradiation during large-scale fire testing," *International Journal of Thermal Sciences,* 2017.

[21] B. Linnan, "Distribution of Energy in Large Compartment Fires," 2016.